2007-04-23

# DNA-Templated Nanomaterials

Hector Alejandro Becerril-Garcia
*Brigham Young University - Provo*

# DNA-TEMPLATED NANOMATERIALS

by

Héctor Alejandro Becerril García

A dissertation submitted to the faculty of

Brigham Young University

in partial fulfillment of the requirements for the degree of

Doctor of Philosophy

Department of Chemistry and Biochemistry

Brigham Young University

August 2007

BRIGHAM YOUNG UNIVERSITY

GRADUATE COMMITTEE APPROVAL

of a dissertation submitted by

Héctor Alejandro Becerril García

This dissertation has been read by each member of the following graduate committee and by majority vote has been found to be satisfactory.

| | |
|---|---|
| Date | Adam T. Woolley, Chair |
| Date | Matthew C. Asplund |
| Date | David V. Dearden |
| Date | Paul B. Farnsworth |
| Date | Matthew R. Linford |

BRIGHAM YOUNG UNIVERSITY

As chair of the candidate's graduate committee, I have read the dissertation of Héctor Alejandro Becerril García in its final form and have found that (1) its format, citations, and bibliographical style are consistent and acceptable and fulfill university and department style requirements; (2) its illustrative materials including figures, and charts are in place; and (3) the final manuscript is satisfactory to the graduate committee and is ready for submission to the university library.

_____
Date

_____
Adam T. Woolley
Chair, Graduate Committee

Accepted for the Department

_____
David V. Dearden
Graduate Coordinator

Accepted for the College

_____
Tom Sederberg
Associate Dean, College of Physical and Mathematical Science

# ABSTRACT

DNA-TEMPLATED NANOMATERIALS

Héctor Alejandro Becerril García

Department of Chemistry and Biochemistry

Doctor of Philosophy

Nanomaterials display interesting physical and chemical properties depending on their shape, size and composition. Self-assembly is an intriguing route to producing nanomaterials with controllable compositions and morphologies. DNA has been used to guide the self-assembly of materials, resulting in: (1) metal nanowires; (2) metal or semiconductor nanorods; (3) carbon nanotubes; and (4) semiconductor, metal or biological nanoparticles. My work expands the range of DNA-templated nanomaterials and develops novel ways of using DNA to pattern nanostructures on surfaces. I have performed the first synthesis of silver nanorods on single-stranded DNA, an attractive material for localizing DNA-coupled nanostructures through hybridization. I have demonstrated an ionic surface masking protocol to reduce ~70% of non-specific metal deposition (a pervasive problem) during electroless plating of DNA with silver or copper. I have designed and constructed discrete three-branched DNA junctions as scaffolding for self-assembling three-terminal, individually-gateable nanotransistors. I have labeled

these DNA structures with single streptavidin molecules, as a model for the placement of semiconductor nanocrystals at the junctions. Moreover, I have shown selective silver and copper plating of branched DNA constructs, with crystallinity that depends on plating conditions. I have fabricated DNA-templated nickel nanostructures on surfaces and demonstrated their reversible interaction with a histidine-labeled protein, as a model system for patterning histidine-tagged nanostructures on surfaces. Previous methods were limited to decorating DNA scaffolds using streptavidin-biotin interactions. Finally, I have developed DNA shadow nanolithography, which uses angled thin-film deposition and anisotropic etching to transfer patterns of surface-aligned DNA onto substrates as nanoscale trenches with linewidths <30 nm. Nanotrenches can be post-processed with microfabrication methods to modify their properties; I have constructed metal lines and nanopores from such trenches. This dissertation summarizes the principles and methods for synthesis and characterization of DNA-templated nanomaterials. These biologically templated constructs may be useful in the fabrication of self-assembled chemical and electrical sensors, and as structural materials for nanofabrication and nanopatterning on surfaces.

# ACKNOWLEDGEMENTS

Several individuals deserve recognition for their service to me during my time at BYU. I thank John Craw, Allison Nelson; Darbi Chávez, Randall Stoltenberg, Adam Washburn, Dr. Huijun Xin and Dr. Ryan T. Kelly for their contributions to my research and for many hours of stimulating discussions. I thank Joshua Beutler, Weisheng Hu, Tao Pan and Joseph Bussio for help in the cleanroom. I thank Dr. John Gardner, Michael Standing, Dr. Jeffrey Farrer and Dr. Richard VanFleet for training and assistance with electron microscopes. I thank Robert C. Davis for technical discussions and for the use of his electron-beam lithography system. I thank Dr. John N. Harb for useful discussions on scientific and administrative topics. I thank Dr. Roger G. Harrison for numerous hours spent in collaboration and for helpful discussions. I thank Dr. Steven R. Goates for his critical evaluations of my work. I particularly express my thanks to the members of my graduate committee, Dr. Matthew C. Asplund, Dr. David V. Dearden, Dr. Paul B. Farnsworth, and Dr. Matthew R. Linford, for the time they took to influence my work through the years and for their criticism and advice which served my research greatly. I also wish to thank the Department of Chemistry and Biochemistry at BYU and its staff for the support and the great environment it provided for me during my stay.

I acknowledge financial support from the Department of Defense, the Army Research Office, the National Science Foundation, the Petroleum Research Fund administered by the American Chemical Society and the Department of Chemistry and Biochemistry at BYU. I wish to express special appreciation to the donors of the Garth L.

Lee Research Fellowship, the Roland K. Robins Graduate Research Fellowship, the Charles E. & Margaret P. Maw Research Fellowship, and the Loren C. & Maurice F. Bryner Award, whose generosity and vision provided me with additional economic resources.

In a very especial manner I thank my advisor, Dr. Adam T. Woolley, for his scientific leadership and for his sincere concern for my professional development. He proved to be a great mentor, a loyal friend, and a man of an unimpeachable character. I thank him for giving me the example, the guidance, the freedom, the resources, and the encouragement that I needed along the way to come to the end of this endeavor.

Finally, I wish to thank my sweet wife, Darlette who patiently and lovingly supported my efforts during these many years and who also gave me three beautiful daughters to cheer up our time at BYU.

Héctor Alejandro Becerril García

# TABLE OF CONTENTS

# LIST OF FIGURES

# LIST OF TABLES

# CHAPTER 1: INTRODUCTION

## *1.1. Nanomaterials and Nanofabrication*

### 1.1.1. Justification

Nanomaterials are physical bodies that have dimensions on the order of several nanometers (nm, 1 nm = $10^{-9}$ m). Nanomaterials can display distinct mechanical, optical, electronic or chemical properties as a direct result of their nanometer dimensions. These nanoscale-induced properties are strongly dependent on the size, shape, chemical composition, and internal structure of the nanomaterial, as well as on the type of interfaces that the nanomaterial establishes with its surroundings.

Synthetic nanomaterials can be found in unexpected places. The recently identified metal nanoparticles that impart unfading color to archeological glazes from Spain [1] and Italy [2, 3], and the newly discovered carbon nanostructures in Damascene steel [4], which seem to be responsible for the remarkable sharpness and durability this material, are just two examples of man-made goods benefiting from serendipitously included nanomaterials.

Scientific interest in the properties of nanomaterials and their deliberate synthesis began in the second half of the twentieth century. As early as 1959, U.S. physicist Richard Feynman challenged the scientific community to tackle "the problem of manipulating and controlling things on a small scale" [5]. His rhetoric focused on the

potentially large economic and technological advantages of storing information and manipulating matter at the nanometer scale. Feynman delineated some of the theoretical and practical challenges involved in such efforts and proposed solutions to a number of these. For example, he mentioned the need for improved understanding of the physics of nanometer-scale objects, and the absence of techniques for mass-producing these structures in a controlled manner. Feynman proposed that if the resolution of the electron microscope of his day could be improved by a factor 10 it could become a tool for the fabrication and inspection of such materials. He also proposed serial nanofabrication approaches based on sequential evaporation of materials at controlled locations. Finally, he questioned if mechanical machines with moving parts could be reduced to be able to operate on nanometer-size objects. Feynman also speculated about the novel array of material properties that would be achieved if atoms and molecules could be rearranged in predetermined, "unnatural" patterns to form nanostructured solids containing electronic circuits, waveguides, etc.

In spite of such an early and clear invitation to develop what is now know as nanoscience, it was not until the decade of the 1980's (**Fig. 1.1A**) that interest in the systematic study, design and production of nanomaterials began to increase. Since that time the scientific community has launched itself on a multidisciplinary quest (**Fig. 1.1B**) for the mastery of nanoscale phenomena.

Also in this same period, publications aimed at the general population presented futuristic projections that elaborated on the ultimate potential of industrial-scale production of nanomaterials [6, 7]. These expressed the hope that "nanotechnology" would eventually mass-produce macroscopic objects with atomic precision, that it would

be energy efficient and would generate no waste. While the expected benefits from such a technological feat could be revolutionizing, it is unclear if they will ever be realized.

Awareness of the topic grew, and by the turn of the century, various countries had recognized the significance of nanomaterials and allocated significant funding to their research [8]. Current investigations in nanomaterials seek to understand and to harness nanoscale phenomena to enhance functional properties of everyday materials, devices and products. The state of the art of the nanofabrication field is encouraging, with technologies that are already at the commercial stage, such as surface-customized semiconductor nanocrystals for unquenchable fluorescent detection [9-11] in the life sciences.

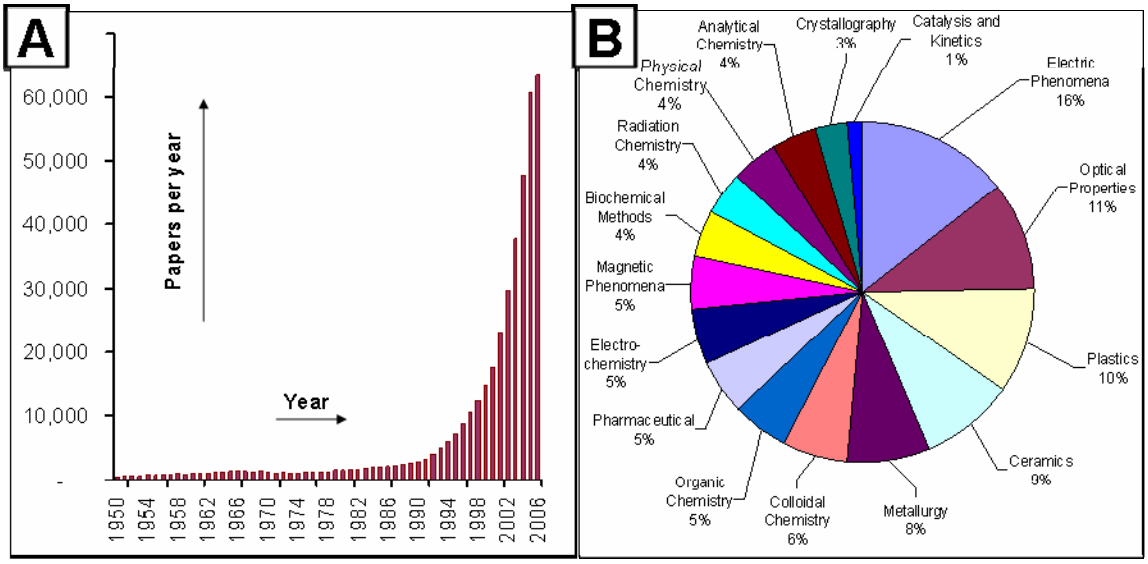


**Figure 1.1.** Analysis of journal publications containing the keywords nano or sub-micron using SciFinder Scholar™, a scientific search engine from the American Chemical Society (ACS). **(A)** Histogram showing the trend in the number of published papers per year. **(B)** Clasification of the papers shown in **(A)** by ACS section title.

### 1.1.2. Bottom-up vs. Top-down Nanofabrication

Nanofabrication is the process of producing structures with predetermined compositions, shapes, and interfaces at the nanometer size scale. In the laboratory, such a stringent degree of control over matter is not achieved easily, and multidisciplinary

approaches to the problem are often required. Nanofabrication techniques can be roughly classified as following either a "top-down" or "bottom-up" strategy [12], although increasingly, the tendency is to combine the two [13, 14]. Top-down approaches to nanofabrication advocate the use of macroscale manufacturing operations to manipulate matter at the nanoscale. Top-down nanofabrication requires high-precision, heavily automated, high-maintenance, and expensive equipment to achieve the smallest possible spatial resolution of individual patterning and processing steps. Ancillary expenses include controlled working environments, highly skilled staff, and extremely pure starting materials. The main advantages of this nanofabrication strategy are high throughput, low cost per device, high reproducibility, and process reliability. Its most significant disadvantages are the steep capital investment required for establishing a top-down nanofabrication facility (10-100M U.S. dollars [15]), and the need for producing extremely large numbers of devices to compensate for escalating equipment costs. Thus, state of the art top-down nanofabrication facilities tend to be out of reach for most research institutions and companies.

Bottom-up nanofabrication proposes ways to overcome the disadvantages of the top-down approach, and the implementation of this nanofabrication concept has led to the development of multiple strategies. The unifying principle for all bottom-up nanofabrication variants is the use of nanometer-scale units of known composition and properties to assemble nano-, meso-, and eventually macroscale objects while maintaining nanoscale control over the final composition and structure. Bottom-up strategies propose fabrication scenarios where the building units are treated as molecular entities. Nanoscale building blocks (NBBs) can be synthesized by chemical methods,

extracted from living organisms, or they can be the microorganisms themselves. The assembly of these NBBs would ideally be carried out inexpensively using liquid or liquid/solid environments. The hypothetical result of bottom-up nanofabrication processes would be the controlled formation of nanostructured devices or products in large quantities, inside simple chemical reactors.

#### 1.1.2.1. Bottom-up Nanofabrication by Self-assembly

Bottom-up nanofabrication is strongly tied to the concept of biological self-assembly [16-21]. Living organisms become organized and grow without the aid of external manufacturing equipment; individual cells develop from within, thanks to self-regulating constructive and destructive processes. Following this ideal, bottom-up nanofabrication processes seek to take advantage of the chemical affinity and electrostatic interactions between distinct NBBs to achieve ordering and self-assembly. The NBBs used in chemical self-assembly can be synthetic or biological materials. Synthetic NBBs include colloidal nanoparticles [22-27], carbon nanotubes [28-30], semiconductor nanowires [31, 32], polymers and copolymers [13, 33, 34], etc. Viruses [35-39], peptides [40, 41], and nucleic acids [42, 43] are biological materials used as NBBs.

During chemical self-assembly the target structure forms by taking materials and energy from its finely-tuned chemical environment, which could be as simple as a temperature-controlled solution of the reactants in a buffer. Chemical self-assembly has potentially low processing costs and moderate equipment requirements which would constitute a major economic advantage relative to top-down nanofabrication.

Another potential advantage of bottom-up nanofabrication resides in its theoretical ability to produce molar-scale quantities of nanostructures in parallel. On the other hand, there are currently many disadvantages of bottom-up nanofabrication. These comprise poor performance of the self-assembled materials, low assembly yields, limited throughput, restricted complexity of the fabricated materials, challenges in large-area patterning, and suboptimal reproducibility. Indubitably, these issues spring from both the complexity of the self-assembly process and the relative newness of the field. Current developments are encouraging, but economically feasible bottom-up nanofabrication is still a long-term goal.

### 1.1.3. Template-mediated Nanofabrication

Bottom-up nanofabrication is often accomplished by introducing templates that guide the self-assembly of NBBs into nanoscale constructs of predetermined shapes. The interactions between these templates and the NBBs are complex and result from the interplay of multiple forces that attract or repel material to or from the template. Top-down nanofabrication techniques may also utilize nanostructured templates to produce nanoscale features with mainstream microfabrication tools, but in this case the template merely acts as a physical barrier that patterns the deposition of the templated material.

Nanofabrication templates can be classified as sacrificial or structural depending on whether or not the template remains after nanofabrication. Porous alumina membranes exemplify sacrificial templates. These membranes are used to direct the deposition of metallic nanowires [44, 45], semiconductor nanowires [46, 47] and proteins [48] inside their nanometer-size pores. The deposited nanostructures are then released by dissolution

of the alumina template. Other sacrificial templates that have been used for nanofabrication include polymer nanospheres [49, 50], carbon nanotubes [51], and multilayer lipid-deoxyribonucleic acid (DNA) systems [52].

Structural templates are also used in nanofabrication. For example, phase-segregated block-copolymer surfaces have recently been used to direct the assembly of proteins to different polymer components of the surface [53, 54]. Such copolymer surfaces are structural templates that remain attached to the synthesized nanomaterial to provide spatial organization and mechanical strength. Other structural nanofabrication templates include self-organized facets on inorganic crystals [55, 56], and biological macromolecules such as nucleic acids [20, 57] and proteins [58].

### 1.1.4. Biological Macromolecular Templates for Nanofabrication

Biological macromolecules such as DNA and polypeptides may be uniquely suited as templating agents because their size and shape are readily controlled by polymerization and folding, and because of their rich chemical functionality, which may allow them to interact with NBBs of interest. Indeed, nature has developed numerous macromolecular nanofabrication systems that guide the assembly of structures such as microtubules, lipid membranes, cellular organelles, etc. Importantly, biological nanofabrication systems perform best *in vivo*, and their direct utilization in synthetic nanofabrication is not trivial. The group of Angela Belcher pioneered the genetic engineering of M13 viral strains that display peptides with affinity for relevant inorganic semiconductor crystals [18, 39, 59, 60], and magnetic materials [18, 61, 62]. Her group has also isolated peptides that can recognize and bind to defects on germanium surfaces [63], and other peptides that can bind to polymer surfaces [64, 65]. Other groups have also modified viruses to serve as

NBBs [66, 67]. While such results are highly encouraging, the direct appropriation of biochemical pathways of more complex organisms for synthetic nanofabrication remains an ambitious long-term goal. Still, templated bottom-up nanofabrication can benefit now from the selective incorporation of principles and materials from biological systems. The fields of biomineralization [17, 21, 68], peptide-mediated self-assembly [12, 69, 70] and DNA-templated organic synthesis [43, 71, 72] exemplify how biological macromolecules can be utilized to facilitate synthesis and nanofabrication.

## *1.2. Self-assembled DNA-templated Nanomaterials*

### 1.2.1. The DNA Molecule

DNA's high information content, predictable reactivity and general ruggedness make it a promising templating agent for nanofabrication [42, 73-75]. Because of its functionality *in vivo*, this molecule has attracted significant attention in the field of chemical self-assembly.

#### 1.2.1.1. Function of DNA in Nature

Living organisms use DNA as the repository of their genetic blueprint. In eukaryotic organisms, each living cell stores its DNA inside the nucleus. There, nuclear enzymes, proteins, and protein-DNA complexes organize, read, repair and replicate nuclear DNA. Outside the nucleus, another set of enzymes detects and digests foreign DNA. The information inherent in the nuclear DNA is transcribed into messenger ribonucleic acid (RNA) molecules. These messengers are transferred to the ribosome, where translation and protein assembly takes place. Newly minted proteins are further modified in the cytoplasm and released to perform their functions as biological nanomachines [76]. In spite of its apparently passive role, DNA is the key element of the cellular

nanofabrication apparatus, because it contains all the information necessary to construct and program the entire system.

#### 1.2.1.2. Overview of DNA Structure

DNA comprises a family of macromolecules that share common structural motifs which combine to form covalently and non-covalently bonded supramolecular entities of varying shape and size. The basic structural unit of DNA is the nucleotide, itself composed of a monophosphorylated deoxyribose sugar attached to a nitrogenated aromatic nucleobase. The four nucleobases found in DNA nucleotides are: adenine (A) and guanine (G), which are purine derivatives; and the pyrimidine derivatives cytosine (C) and thymine (T). Concatenation of N nucleotides through phosphodiester bonds forms a chain or a DNA strand (**Fig. 1.2A**) with $N^4$ different possible nucleobase sequences. Sequence diversity is DNA's information storage mechanism, with a tremendous density of 2.86 bits per linear nm [77].

DNA polymerase enzymes add nucleotides to the 3' position of a growing DNA chain [78]. The sugar carbon in this position bears a hydroxyl group that condenses with the phosphate group on the 5' sugar carbon from the incoming nucleotide. Thus, DNA molecules have a sense or direction, and by convention their sequence is given by identifying the nucleobases from 5' to 3'.

The nucleobases within DNA experience non-covalent interactions such as π-stacking and base-pairing. These interactions add stability to the macromolecule. In π-stacking, the planar aromatic rings in contiguous nucleobases within each DNA strand align face to face (**Fig. 1.2B**) to minimize their energy by extended electron delocalization.

Additionally, π-stacking gives directional stiffness to the molecule and is responsible for the twist in dsDNA.

Base-pairing is a more selective type of interaction than π-stacking. Base-pairing is due to multiple hydrogen bond bridges between two specific nucleobases in a coplanar orientation. Specific base-pairing occurs between adenine and thymine nucleotides with formation of 2 hydrogen bonds (**Fig. 1.2C**), and between cytosine and guanine nucleotides with 3 hydrogen bonds (**Fig. 1.2D**). Mismatched interactions are possible, but these carry energy penalties.

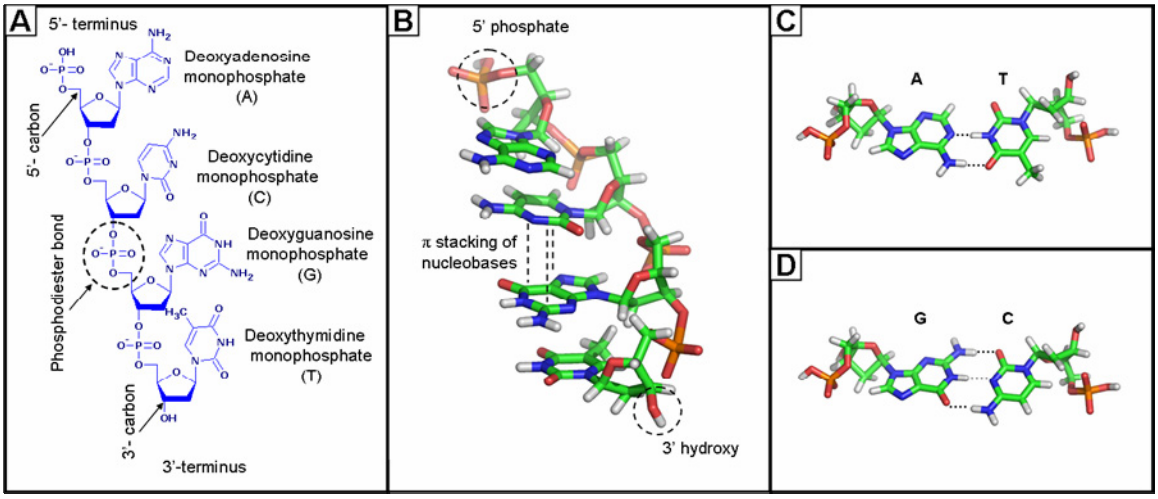


**Figure 1.2.** Structural elements of the DNA molecule. **(A)** Chain of four nucleotides with the sequence 5'-ACGT-3' showing the structure of individual nucleobases, phosphodiester links and 5' and 3' capping groups. **(B)** Orthoscopic view of **(A)** showing characteristic alignment of nucleobases. **(C-D)** Watson and Crick dinucleotide pairs interacting through hydrogen bonds.

Base-pairing can occur within a single strand of DNA, forming hairpin- and loop-like structures. It can also occur intermolecularly, forming the familiar DNA double-helix between complementary portions of the interacting strands. This iconic right-handed double-helix is a supramolecular DNA structure called B-DNA (**Fig. 1.3A**). Its structure was first elucidated from X-ray diffraction and chemical reactivity data by Watson and Crick [79], for which the 1962 Nobel Prize in Medicine was awarded [80, 81]. DNA can

also fold into a wider, right-handed double helix called A-DNA (**Fig. 1.3B**) when its sequence contains long polypurine stretches, or into a left-handed double-helical form named Z-DNA (**Fig. 1.3C**), which is favored by a sequence that alternates purine and pyrimidine residues [82, 83]. Similarly, other base-pairing modes can exist once a DNA double-helix is formed, and these lead to the formation of short segments of triple [84] and quadruple helices [85]. Although these alternative helical forms have important biological functions and even some applications in nanofabrication, this work deals only with B-DNA.

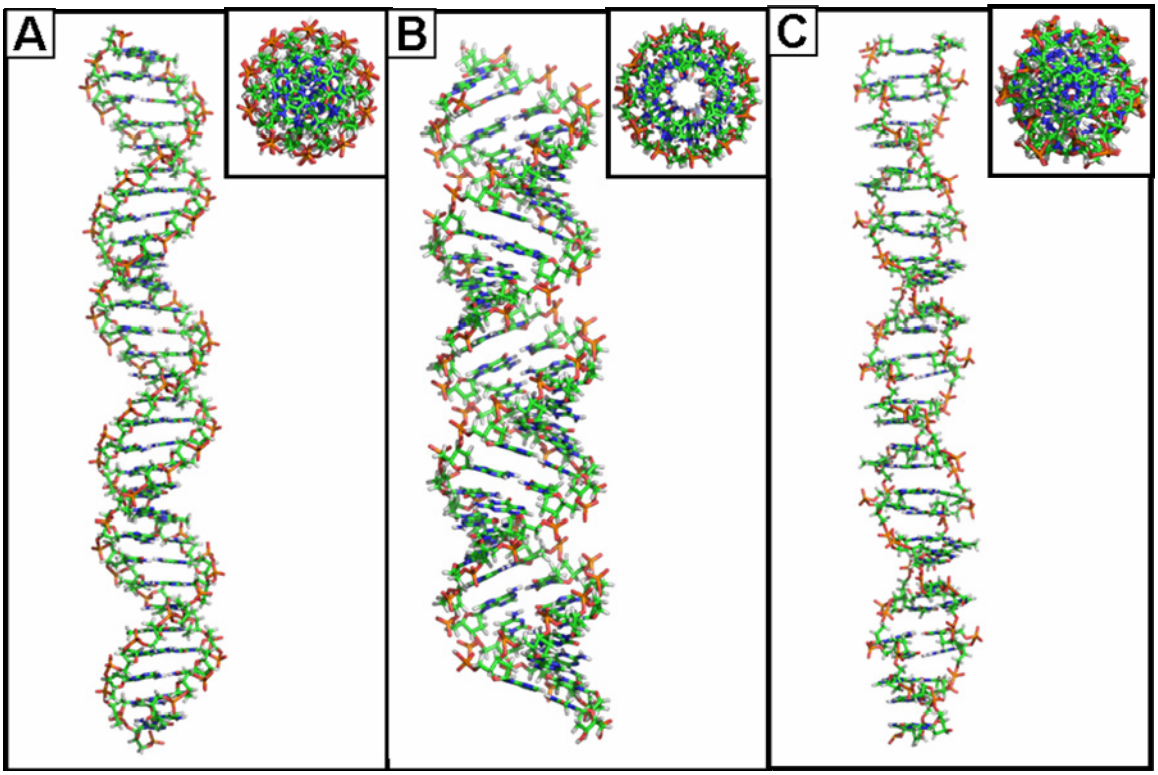


**Figure 1.3.** Three different families of DNA double helices. **(A)** Right-handed B-DNA structure determined by Watson and Crick. **(B)** Right-handed A-DNA. **(C)** Left-handed Z-DNA. Insets show axial views of the helices.

### 1.2.1.3. DNA Melting Temperature and Secondary Structure

The secondary structure of a single-stranded DNA (ssDNA) molecule is determined by intramolecular base pairing. The stability of a base-paired region in solution depends

on its length, nucleotide composition and the ionic strength of the medium. Longer base-paired regions are more stable against disruption by shear and thermal energy. A-T pairs contribute -4 kcal/mol while G-C pairs contribute -15 kcal/mol of stabilization energy [86, 87]. Moderate ionic concentrations screen long-range repulsive phosphate-phosphate interactions without affecting short-range hydrogen bonds.

The DNA melting temperature ($T_m$) is defined as the temperature at which 50% of the possible base-pairs have been separated. $T_m$ is a relative measure of the stability of the secondary structure formed by a particular sequence and can be calculated using empirical correlations [88], such as **Equation 1.1**,

$$T_m = 81.5 + 16.6 \log [Na^+] + \frac{41(G+C)}{L} - \frac{500}{L} \qquad \text{[Eq. 1.1]}$$

which is useful for sequences 20-100 bases long, or **Equation 1.2**, used for sequences shorter than 20 bases.

$$T_m = (A+T)2 + (G+C)4 - \log (0.050) + 16.6 \log [Na^+] \qquad \text{[Eq. 1.2]}$$

In both cases, the letters ***A***, ***C***, ***T*** and ***G*** represent the number of the respective nucleobases present in the sequence, and ***L*** is the sequence length.

Beyond these simple models, there are several academic online servers [89-91] that utilize extensive tables of experimentally determined free-energy values and other thermodynamic parameters [92-94] to calculate $T_m$ and predict the secondary structure of DNA and RNA sequences. These $T_m$ and secondary structure calculations are useful in the design of suitable DNA sequences for many biochemical protocols, such as DNA amplification by the polymerase chain reaction (PCR) [95], which is a technique utilized in fields ranging from molecular biology to criminal forensics.

### 1.2.1.4. Enzymatic Manipulation of DNA

PCR is an example of the use of cellular enzymes for the extracellular manipulation of DNA. The cellular battery of DNA-handling tools includes enzymes that read, cut, twist, unwind, repair, and mark specific DNA sequences. Many of these enzymes are commercially available for use in molecular biology, and extensive compilations of experimental procedures involving DNA and enzymes are available [96]. Enzymatic modification of DNA has been used to enhance DNA templates for nanofabrication and self-assembly [97, 98].

### 1.2.1.5. DNA Sources

DNA can be harvested from organisms including viruses, bacteria, and higher animals. Such natural DNA is inexpensive and readily available from specialized vendors. One commonly used natural DNA molecule comes from the λ-bacteriophage [99]. λ-DNA is a linear molecule 48,502 base-pairs long (~16 μm). It possesses a 12 base-long ssDNA 5' overhang at each end, which is utilized to close the molecule into a replicating circle once the λ-virus injects the DNA into a host cell. λ-DNA is utilized in biochemistry as a transfection vector to introduce and express foreign genes in a host bacteria. λ-DNA is also commonly used in nanofabrication. **Table 1.1** shows commercially available, natural DNA molecules commonly used in nanofabrication.

**Table 1.1. Examples of Commercially Available DNA and Their Sources.**

| Molecule | Length (base pairs) | Shape | Source | Genbank# |
|---|---|---|---|---|
| **λ-DNA** | **48,502** | **Linear** | **Lambda bacteriophage** | **NC_001416** |
| **M13mp18** | **7,249** | **Circular** | **M13 bacteriophage** | **X02513** |
| **φX174** | **5,386** | **Circular** | **φX174 bacteriophage** | **NC_01422** |

The sequence of natural DNA molecules can be customized through enzymatic manipulations, but extensive modifications are neither practical nor economical. On the other hand, short fragments of DNA (oligonucleotides) can be synthesized with pre-specified sequences using automated equipment [100-102]. During synthesis nucleotides are added in sequence from the 3' to the 5'end. Derivatized nucleotides can be added at any point along the polymer chain. The length of synthetic DNA oligonucleotides is limited to ~150 units because of the finite reaction yield of individual coupling steps. Synthetic oligonucleotides are used in combination with enzymes for multiple genetic engineering procedures including PCR. DNA oligonucleotides also find applications in DNA self-assembly.

### 1.2.2. Chemical Interactions of DNA with Other Nanomaterials

DNA contains chemical handles that allow it to interact with inorganic nanomaterials to form self-assembled nanostructures. The main chemical handles in DNA are: (1) the negatively charged phosphate backbone; (2) metal-chelating nucleobases; and (3) aromatic rings that form a hydrophobic core.

The phosphate groups on the DNA backbone are deprotonated and bear a negative charge except at pH <2.5. In each DNA strand, the negative charges of the phosphates occur at a linear density of 1 every 0.34 nm. DNA molecules in solution tightly condense cations to bring the charge density down to ~1 charge every 0.7 nm. This behavior was first predicted by Manning [103-105], and the critical value of 0.7 nm is the Bjerrum length ($\lambda_B$), or the distance at which the electrostatic force between two point charges becomes smaller than the background thermal agitation. $\lambda_B$ is a function of the temperature and the dielectric constant of the medium as shown in **Equation 1.3**,

$$\lambda_B = \frac{e^2}{4\pi\varepsilon k_B T} \qquad \text{[Eq. 1.3]}$$

where $e$ is the electron charge, $\varepsilon$ is the dielectric constant of the medium, $k_B$ is Boltzmann's constant and **T** is the temperature in degrees Kelvin.

After the initial counterion condensation, DNA molecules seek to attract sufficient cations to achieve charge neutrality. The portion of solution that is accessible to the DNA for this process scales with the Debye length ($\lambda_D$), which measures spatial reach of electrostatic interactions in a material. For dilute electrolyte solutions, $\lambda_D$ can be calculated using **Equation 1.4**,

$$\lambda_D = \sqrt{\frac{\varepsilon k_B T}{2N_A e^2 I}} \qquad \text{[Eq. 1.4]}$$

where $N_A$ is Avogadro's number and $I$ is the ionic strength of the solution, calculated by **Equation 1.5**,

$$I = \frac{1}{2}\sum_{i=1}^{n} c_i z_i^2 \qquad \text{[Eq. 1.5]}$$

in which $c_i$ is the concentration of the $i^{th}$ ionic species and $z_i$ is the number of electric charges it bears.

Under biological conditions, or in typical DNA-templated nanofabrication buffers, the DNA molecules condense sodium or magnesium cations until charge neutrality is achieved. These cations can be exchanged for transition metal cations which have higher charge density and polarizability than sodium or magnesium. Transition metal cations localized on DNA are important precursors for the formation of DNA-templated metal nanostructures.

Metal cations can also interact with the aromatic nucleobases in DNA through dative bonds. In effect, ssDNA oligonucleotides can wrap around metal cations and charged metal clusters, stabilizing them against flocculation and precipitation [106]. Double-stranded DNA (dsDNA) is more rigid but can still interact with transition metal cations that are condensed on the molecule [107]. Chelation of transition metal ions distorts the double helix structure and causes a slight decrease in the length of DNA molecules and a increase in their diameter [108-110]. Nucleobase chelation favors the exchange of Group IA-IIA metal ions for transition metal ions, because the former do not participate in dative bonding.

The aromatic nucleobases in DNA form intermolecular π-stacking bonds with molecules containing aromatic systems that can insert themselves between consecutive nucleotides in the double helix. This DNA intercalation distorts the shape and hampers the *in vivo* functionality of dsDNA. Many intercalators such as benzene and polycyclic aromatics are potent carcinogens, while other intercalators such as cis-platin are utilized to kill rapidly replicating cancerous cells. Intercalation can be used in nanofabrication to insert chemical functionality into DNA and to couple DNA to other nanomaterials.

The structure and reactivity of DNA molecules can also be modified by temperature and pH. Temperatures above the $T_m$ transform a dsDNA into separate ssDNA molecules. These can then react with ssDNA oligonucleotides to form new secondary structure. Indeed, temperature programming of multicomponent DNA oligonucleotide systems can separate all strands and promote assembly of a target product based on $T_m$ differences. DNA solutions are resistant to temperature damage and withstand controlled heating as high as 95 °C for several minutes, while temperatures of ~20 °C are recommended for

their long term storage. Temperature treatment of DNA solutions is also useful for denaturing or inhibiting enzymes that could degrade the DNA.

The pH of DNA solutions should be kept above 4, to prevent depurination of the nucleotides, and below 11, to avoid hydrolysis of the phosphodiester bonds. Within these limits the pH can be varied to favor interaction of other nanomaterials with DNA.

DNA is sensitive to chemical oxidants, UV light and free radicals [111-113]. Oxidants are able to attack sugar moieties and cleave phosphodiester bonds. UV light with 260 nm wavelength is absorbed strongly by the DNA nucleobases, and this localized energy can be transferred to oxygen, forming singlet oxygen and other oxygenated radicals that attack nucleobases and transform them into oxidized derivatives such as 8-oxoguanine or thymidine glycol. In a biological context these nucleobase mutations can lead to loss of functionality, cellular death or cancer. In a nanofabrication context, DNA damage by oxidants, UV and free radicals leads to single- and double-strand breakage, with loss of structural integrity. When this type of damage is severe, DNA molecules can be degraded to disconnected oligonucleotides unfit to serve as nanofabrication templates. Importantly, the combination of mild reducing agents and multivalent transition metals can also damage DNA by *in situ* generation of singlet oxygen and unstable ionic species like $Cu^{+}$ [114].

Mechanical forces can also damage DNA. Typical DNA molecules are very high-molecular weight polymers, and viscous shear from rapid vortexing can cause chain breakage. Also, repeated cycles of freezing and thawing of DNA solutions can fragment long DNA molecules due to the volumetric expansion during ice formation.

### 1.2.3. DNA as a Nanofabrication Material

DNA has been used as nanofabrication a material in at least three different ways: (1) fabrication of two-dimensional DNA scaffolds; (2) DNA-mediated assembly of nanoparticle clusters; and (3) selective deposition of inorganic or biological materials on DNA templates.

#### 1.2.3.1. Self-assembled DNA Lattices

In 1982 Nadrian Seeman proposed the use of non-linear DNA molecules to construct periodic networks with customizable connectivity [115]. He then demonstrated the fabrication of a small four-armed junction made from DNA oligonucleotides [116]. After experimenting with the properties of junctions and more complex DNA objects [117, 118], Seeman introduced the double crossover DNA motif [119] to increase the stiffness of the DNA scaffold, and succeed in making a two-dimensional DNA lattice [120]. New DNA motifs of increasing complexity followed, including the paranemic crossover [121], the triple crossover [122], the DNA triangle [123], the three helix-bundle [124], and recently the six-pointed DNA star [125]. Several types of DNA lattices have since been produced [126-135]. Some lattices have been made specifically as scaffolds for the localization of nanoparticles [136-139], proteins [140-142] and DNA oligonucleotides [143].

Beyond strictly periodic lattices, other two-dimensional DNA-self assembling approaches have been pursued. For instance, algorithmic self-assembly allows the use of two-dimensional DNA nanostructures to perform computational operations [144-151]. The method is based on the fabrication of DNA tiles with strict connectivity rules which encode the problem to be solved. After mixing and thermal annealing of the tiles, the

solution to the problem is obtained by inspection of the final assembly. Another unique DNA self-assembly method recently demonstrated is DNA origami [152], in which a long ssDNA molecule is folded into a designed shape by interaction with multiple DNA oligonucleotides that anchor the final geometry in place.

Self-assembling DNA nanostructures often require large numbers of synthetic DNA oligonucleotides, on the order of several tens to hundreds per shape [152], making DNA self-assembly research relatively expensive. Moreover, the oligonucleotide sequences need to be optimized to ensure proper assembly [153-157]. Finally, the mechanical strain in the final construct must be minimized [158, 159] to achieve effective self-assembly.

#### 1.2.3.2. DNA-mediated Assembly of Nanoparticles

The field of DNA-directed assembly of nanoparticle clusters can be subdivided in two main efforts: (1) selective nanoparticle aggregation for chemical analysis; and (2) aggregation of nanoparticles for structural purposes.

The group of Chad Mirkin has pioneered the concept of DNA-mediated nanoparticle aggregation for chemical analysis [22, 160, 161], using oligonucleotide-functionalized nanoparticles (OFN) that interact and aggregate upon chemical recognition of a DNA analyte. The group has used the colorimetric change in OFN systems as a reporter mechanism to detect DNA oligonucleotides [160, 162-164], triplex-forming DNA sequences [165], proteins [166], and DNA-binding molecules [167]. The optical properties of aggregates of OFNs were shown to depend on the size of the aggregate rather than the length of the oligonucleotide linkers [168]. Mirkin's group also developed OFN-based electrical methods for reporting oligonucleotiode binding [169, 170], and

investigated the effects of the metal nanoparticle on the stability and hybridization properties of metal nanoparticle-bound ssDNA [171-175].

The group of Wolfgang Fritzche has developed optical [176-178] and electrical [179, 180] methods to detect DNA hybridization using nanoparticle-labeled oligonucleotides. Further, OFNs containing semiconductor nanoparticles have been used to perform photoelectrochemical [181] and fluorescent [182, 183] reporting of DNA hybridization.

Several groups have researched the DNA-mediated structural organization of nanoparticles. The group of Alivisatos demonstrated the organization of OFNs into "nanocrystal molecules" [184-186], and used gel electrophoresis to purify OFNs with discrete numbers of oligonucleotides [187], which resulted in more reproducible, higher-yield assemblies. Mirkin's group described DNA-mediated assembly of binary nanoparticle networks [188], the organization of OFNs on DNA-coated diatom silica shells as rapid a way of forming nanostructured materials for catalytic and optical applications [189], and structural studies of OFN networks that show them to be fractal objects [175, 190]. Other researchers reported kinetic studies showing that OFNs with partially rigid linkers between the nanoparticle and the DNA oligonucleotides assemble faster and more effectively because the oligonucleotides are more available for reaction [191]. Recently, Alivisatos and Seeman reported two-dimensional ordering of single-oligonucleotide-functionalized gold nanoparticles using a stiff, DNA scaffold based on triangular DNA motifs [192].

### 1.2.3.3. DNA-templated Deposition of Nanomaterials

The field of DNA-templated deposition of nanomaterials was inaugurated by the report of selective growth of a semiconductor material on a circular DNA molecule [193]. In that work, the DNA was deposited on a surface and ion exchanged with $Cd^{2+}$, followed by rinsing and exposure to gaseous $H_2S$. Electron microscopy of the product showed that a discontinuous chain of small, ~5 nm diameter CdS nanoparticles had formed on the DNA molecule. Following this report, the group of Erez Braun demonstrated the continuous growth of a silver metal wire on a DNA template [194]. They suspended a single λ-DNA molecule across microfabricated, oligonucleotide-functionalized gold electrodes using the natural λ-overhangs. The immobilized λ-DNA template was ion-exchanged with silver cations and chemically reduced to form a discontinuous chain of silver nanoparticles on the DNA. Electroless plating was used to deposit more silver onto these nanoparticles, forming a continuous, electrically conductive nanowire, ~100 nm in cross-section. From this result Braun's group proposed that DNA could be useful for the self-assembly of nanoelectronic circuits [195]. Using similar DNA metallization schemes, several research groups have since fabricated electrically conductive DNA-templated nanowires made of palladium [196-198], silver [140, 199] and gold [200-202]. Self-assembled DNA nanotubes [136, 203] and three-helix bundles [124] have also been metallized to form electrically conductive silver nanowires. The conductivity of nanowires templated on single DNA molecules has been found to be two orders of magnitude lower than that of the bulk metal in the case of silver [199], and one order of magnitude lower in the case of gold [202]. Non-conductive DNA-templated nanostructures made out of palladium [204], platinum [205, 206], gold [207], copper

[208, 209], nickel [210-212], cobalt [213], copper sulfide [214], and iron oxide [215] have also been reported.

The combination of DNA self-assembly and DNA-templated nanofabrication would seem ideally suited for constructing nanometer-scale electronic devices. Success in this area would allow the assembly of large quantities of such electronic devices at high integration densities using inexpensive chemical methods; however, a fully self-assembled DNA-templated electronic circuit has not yet been produced. Some stepping stones toward the realization that goal have been demonstrated, including: (1) investigations on the selectivity of electroless plating on DNA [110, 114, 206, 216]; (2) construction of branched DNA junctions as templates for three-terminal electronic devices [217-219]; (3) selective localization of carbon nanotubes [220-222], metal nanoparticles [192, 223] and proteins [140, 224] on DNA; and (4) specialized nanofabrication substrates for repeated localization and inspection of DNA-templated nanostructures using atomic force microscopy (AFM) and scanning electron microscopy (SEM) [225], and for AFM and transmission electron microscopy (TEM) [226].

Furthermore, an especially significant development in DNA-templated nanoelectronics came once again from Braun's group. They demonstrated DNA-molecular lithography, which allows sequence-specific localization of a metal-reducing agent, ssDNA binding proteins, antibodies, carbon nanotubes, and structural branching points on λ DNA [201, 224]. This impressive toolset was used to create working DNA-templated, carbon nanotube field-effect transistors [227]. Importantly, even after such a clear proof of concept, significant refinement of the

methodology is still necessary to achieve self-assembling multicomponent nanoelectronic circuits at high integration densities.

The poor electrical performance of DNA-templated materials is another issue that has hampered the realization of DNA-templated nanoelectronic devices. DNA-templated materials are nanocrystalline and have high defect densities [110, 198, 202, 216]. These defects cause the materials to have non-ohmic current-voltage profiles and to suffer from intense resistive heating. A nanowire cross-section of ~50 nm or greater is necessary to attain quasi-ohmic behavior. At a time when the microelectronic industry already talks openly about commercial production of microprocessors with critical dimensions in the 45 nm range [228, 229], the utilization of 30 nm DNA-templated circuits with untested performance seems unlikely.

DNA-templated nanomaterials are still attractive for nanofabrication applications where the size, shape and composition of self-assembled nanostructures need to be controlled. DNA can template the deposition of numerous types of inorganic, organic, and biological materials. My research has dealt with extending the range of materials that can be templated by DNA, and with developing new DNA-templating schemes. For example, I have developed protocols to localize histidine-tagged proteins onto $Ni^{2+}$-treated DNA templates aligned on surfaces [212]. Localization of proteins on DNA had been restricted previously to recombinant proteins that bind to ssDNA, or to streptavidin which binds strongly to biotin-functionalized DNA. Development of specific protocols for the synthesis of a wide variety of DNA-templated nanomaterials on surfaces will enable the self-assembly of nanostructures with rich compositional complexity. Such

nanomaterials may find application as surface modifiers to control and direct the adsorption of chemical and biological entities.

### 1.2.4. Typical Synthetic Procedures for DNA-templated Nanomaterials

DNA-templated synthesis of nanomaterials requires a suitable surface, DNA, a solution containing precursor materials, and a method for transforming these precursors into their final form. The typical preparation of these elements is discussed below.

#### 1.2.4.1. Surface Cleaning

Synthesis of DNA-templated nanostructures begins with proper cleaning of the substrate. The surfaces that I have used in my research include muscovite mica, single-crystal silicon, thermally grown silicon dioxide, alkylsilane self-assembled monolayers, thin gold films, and synthetic polymer coatings. Other substrates utilized in the field include highly oriented pyrolytic graphite (HOPG), aminosilane films, and glass. The minimum requirements for a substrate for DNA-templated nanofabrication are: (1) the surface must have affinity for DNA; and (2) the surface should be sufficiently flat, typically <10 nm root mean square roughness on a 100 $\mu m^2$ image, to allow characterization of individual DNA molecules by AFM.

Muscovite mica is a nanostructured aluminosilicate mineral with a layered morphology. In this material, sheets of potassium cations electrostatically bind anionic aluminosilicate planes, forming a multilayer structure [230]. Applying a shearing stress to mica causes fractures along the potassium ion planes, producing a clean, atomically flat, negatively charged surface. HOPG is also a layered structure that is composed of

graphene sheets held together by van der Waals interactions [231]. This solid responds to shearing stress in a manner analogous to mica.

Single-crystal silicon and thermally grown $SiO_2$ on silicon wafers are already sufficiently flat as a result of chemomechanical polishing. These surfaces may require oxidizing cleaning to remove adventitious carbon and other contaminants which render the surfaces hydrophobic with time. A 3 min dipping of the substrate in a boiling piranha solution (7:3 mixture of $H_2SO_4$ and $H_2O_2$), followed by extensive water rinsing, is effective in eliminating organic contaminants. This cleaning method also creates a newly oxidized surface terminated with silanol groups. Silanol-terminated surfaces acquire a negative charge when placed in contact with solutions with pH > 5.

High-quality alkylsilane films can be formed readily on freshly cleaned, silanol-terminated surfaces using alkylsilane reagents that contain one alkoxy or one halogen leaving group. For example, exposing silanol-terminated surfaces to vapors of methoxydimethyloctadecylsilane at high temperatures causes a condensation reaction that produces a covalent siloxane bond between the surface and the octadecylsilane, with the loss of one methanol molecule. Importantly, for DNA-templated nanofabrication, silane reagents that contain two or three leaving groups should be avoided since they may produce films with increased roughness due to silane polymerization. The formation of aminosilane or other silane films on silicon and silica follows similar strategies. Silane functionalization of silicon and silica neutralizes the natural negative charge of these surfaces, and may or may not introduce new surface charges, depending on the silane headgroup. Glass surfaces have some chemical resemblance to silica, although they also contain Group IA and IIA cations. These surfaces can be cleaned and silane

functionalized in the same way as silica. However, typical glass plates and cover slips are too rough for DNA-templated nanofabrication, such that specialized glass substrates suitable for microscopy applications must be used.

Gold films may be evaporated or sputtered onto several types of substrates. A thin chromium or titanium adhesion-promoting layer is often evaporated first to serve as an interface between siliceous materials (glass, mica, silicon, silica, etc.) and gold. Gold films tend to be significantly rougher than silicon surfaces, and this roughness can increase upon film annealing. Slow evaporation (~1 Å/s) onto a suitable adhesion layer in a clean evaporation system is the best way to limit film roughness. Gold films can be cleaned in piranha solution, but dip times must be kept under 1 min to preserve the adhesion layer.

Synthetic polymer films are formed by spin-coating a dilute polymer solution over a substrate. The thickness and morphology of the deposited layer depend on the polymer concentration, its molecular weight, the spinning conditions, the evaporation characteristics of the solvent, etc. Empirical development of spin-coating recipes is always required when working with a new system. Spin-coated polymer films can provide flat surfaces with designed chemistries.

#### 1.2.4.2. Alignment of DNA Molecules on Surfaces

Cleaned surfaces must often be conditioned to be able to interact with DNA molecules. Anionic surfaces such as mica, glass, silicon, silica and some polymers can be treated with cationic species to present a positively charged layer to polyanionic DNA molecules. Brief incubation of anionic surfaces with dilute solutions of magnesium cations (~50 mM) [232, 233], or with solutions of poly-L-lysine (~1 ppm) [234],

followed by rinsing with purified water creates a positively charged surface that readily adsorbs DNA molecules.

Gold surfaces must be modified to have positive charges that retain DNA molecules from solution. This can be accomplished by incubating the metal with dilute solutions of molecules containing both gold-binding and amine functional groups; for example, 50 ppm cystamine ($NH_2CH_2CH_2SSCH_2CH_2NH_2$) in water imparts a positive charge to gold surfaces to promote efficient DNA adsorption.

Neutral alkylsilane layers [235, 236] and spin-coated films of hydrophobic polymers [237] may retain DNA through van der Waals interactions and require no further preparation. The hydrophobic nature of these surfaces favors the formation of bundles of DNA molecules, since the polar nucleic acid backbones seek to minimize their contact with the surface by forming rope-like structures. If bundles are not desired the surfaces can be incubated with ~10 ppm poly-L-lysine in water.

DNA can be aligned on cleaned, conditioned surfaces by molecular combing [238-240]. Briefly, this procedure involves translating a minuscule drop of a dilute aqueous DNA solution over a conditioned surface, followed by rinsing with purified water. Inside the drop, DNA molecules positioned close to the liquid/solid interface experience surface-attractive interactions. As the drop of solution moves, some of these surface-interacting DNA molecules stay behind, coming out of solution and becoming directionally aligned on the surface as the moving air-liquid interface sweeps along their length. Rinsing with water removes unwanted deposits of salts from the buffer solution. Translation of a drop of DNA solution may be accomplished by a number of mechanisms, including surface-tension mediated motion [240, 241], gas blowing [204,

242], or adsorption of a drop on filter paper. Spin-coating of small amounts of DNA solutions has also been reported to be effective in aligning DNA on surfaces [243], but this method suffers from strong variations in the alignment direction, and the deposition density increases toward the edges of the substrate. Microfabricated polydimethylsiloxane stamps can also be utilized to align DNA on surfaces [244], and this method claims to provide a high degree of spatial control over DNA deposition.

#### 1.2.4.3. Overview of Electroless Plating

A typical DNA-templated metal synthesis is essentially a mild electroless deposition process designed to form nanometer-scale metal sheaths around DNA templates. The simplest formulation for an electroless deposition bath must include a metal source, a metal chelator, a pH regulator, and a reducing agent [245, 246].

Non-chelating salts of transition metals, such as acetates, sulfates, nitrates and chlorides function well as metal sources for electroless plating [247]. To stabilize the metal in solution, and to fine-tune the reduction potential of the reducing agent [248], the pH of the electroless plating bath must be set using reagents that do not coprecipitate with the metal during plating. High concentrations of acids or bases such as $Na_2CO_3$, KOH, $NH_3$, $H_2SO_4$, HCl, etc. are used to impose a working pH. Buffers containing acetates, citrates, phosphates, carbonates, or ammonium can also be used. Chelating buffers such as citrate should be used with care to not reduce the amount of metal available for plating [249, 250].

On the other hand, a metal chelator such as cyanide, citrate, ammonium, tartrate, EDTA, etc. is added to the bath with multiple purposes: (1) to keep the metal cations in solution when the pH of the bath would lead to precipitation; (2) to prevent undesired

reduction of the metal cations by the reducing agent; and (3) to establish a chemical equilibrium that regulates the concentration of reducible metal ions in the bath.

The reducing agent is the most critical component in the formulation of the electroless plating bath. Reducers for electroless processes are either small organic molecules such as formaldehyde [251], hydroquinone, ascorbic acid [252], hydrazine [253], dimethylamineborane [254], etc.; or inorganic species including $NaBH_4$ [255], $H_3PO_2$, $Na_2S_2O_3$ [256], and $Sn^{2+}$ [257]. Reducing agents for electroless plating must be gentle enough to maintain bath stability, but sufficiently aggressive to ensure complete reduction of cations to metal. This subtle balance can be achieved by selecting a pH in the bath that causes changes in the active form and the reducing potential of the reducing agent [248]. Hydroquinone [258] and formaldehyde [259] are examples of reducing agents with reduction potentials that become more positive at acidic pH values. Other agents become uncontrollable at certain pH values due to collateral reactions. For example, acidic solutions of sodium borohydride are highly unstable and readily hydrolyze to $H_2$, $NaB(OH)_4$ and heat, even when no metal is present [260], while basic solutions of the same chemical have useful lifetimes on the order of days.

The exact composition of an electroless plating bath is strongly dependent on the plating metal. The solubility and complexing behavior of the metal cations dictate the type of chelating agent required. For example, gold baths use cyanide salts as complexants [253, 256], while copper baths utilize the less toxic EDTA and tartrate [209, 250]. Furthermore, the formal reduction potential of the plating metal guides the choice of reducing agent, which in turn determines the working pH of the bath. Finally, a complete electroless plating system comprises the electroless bath, the substrate and any

catalyst or seeding elements necessary to activate the substrate for electroless deposition. The plating metal may also influence the way the substrate is prepared for plating and which activators are utilized.

Metallic and insulating substrates can be plated electrolessly to modify their surface properties. After extensive cleaning, substrates that cannot nucleate metal cations from the plating bath are activated. Activation can involve functionalization of the surface or treatment with metal nanoparticles [261, 262]. Self-assembled monolayers have been used to coat surfaces with amine, carboxyl, hydroxyl, glycol and thiol groups which can localize metallic species from solution [263, 264]. For activation with metal particles, the substrates are treated with concentrated solutions of noble metal colloids or partially oxidized metal ions such as $Sn^{2+}$ to allow adsorption of these species on the surface [250, 265]. The activated substrates are then placed in the plating bath where they compete with chelators for the metal cations. The concentration and relative binding affinity of the different chelators involved determines if the bath plates and how long it takes to form an initial metallic layer on the substrate. Metal substrates and those that have been treated with noble metal nanoparticles provide abundant adsorption sites for metal cations. The reducing agent molecules from the bath transfer electrons to these adsorbed ions, transforming them into adatoms on the surface. Substrates that have been activated by electropositive metal ions such as $Sn^{2+}$ perform *in situ* reduction of metal cations that have less positive potentials than the activating ion. Thus, activating ions are completely oxidized to $Sn^{4+}$, and cations from the bath are deposited on the substrate as metal adatoms. In all cases, the deposition of metal on the substrate creates a rough, high-

energy surface that favors further adsorption of cations from solution, which are then reduced by the bath, etc. in an autocatalytic cycle [266].

Electrodeposition and electroless plating are complementary. Advantages of electroless plating over electrodeposition include: (1) establishing electrical contact to the plating substrate is not required, and insulating substrates can be plated; (2) the plating is not restricted to external surfaces of the substrate; and (3) the thickness of the deposit does not vary with the area, shape or orientation of different surfaces on a complex substrate. Conversely, some disadvantages of electroless plating include: (1) complexity of plating baths; (2) lifespan of the plating baths; and (3) the local coexistence of reduction and oxidation reactions can cause coprecipitation and inclusion of residual bath components in the final plated film.

#### 1.2.4.4. Electroless Plating on DNA

For DNA-templated nanofabrication, electroless deposition offers clear advantages vs. electroplating, as simultaneous electrical contact to multiple DNA molecules on surfaces is not possible. Importantly, selective electroless plating of DNA molecules on surfaces requires several adjustments to the chemistry of plating baths. First, the bath must have a pH and composition compatible with DNA molecules. Baths having extremes of pH or those that produce free radicals will quickly degrade DNA. Second, the plating system must be selective enough to prevent indiscriminate metal deposition on the substrate that supports the DNA templates. This can be accomplished by deactivating the substrate through functionalization with alkylmonolayers, by increasing the concentration of chelators in the bath, or by adding agents that attach to the substrate. Third, the interaction between the bath's chelating agents and the plating

cations must not be stronger than the interaction between the DNA and the plating cations. This last requirement allows the DNA to nucleate the selective deposition of material, but it also limits the chemistries that can be used for direct electroless plating on DNA. This constraint can be overcome in certain cases by seeding or sensitizing the DNA with an initial layer of silver or palladium, after which other metals can be plated electrolessly onto the DNA-templated metallic deposit.

Finally, solutions that do not contain reducing agents may use chemistries to deposit other types of materials on DNA; for example, baths that contain sulfide precursors [52, 214] can be used to produce DNA-templated metal sulfides.

## *1.3. Characterization of DNA-templated Nanomaterials*

### 1.3.1. Spectroscopic Methods

Spectroscopic methods are useful for obtaining compositional information of materials in solutions or on surfaces, and are a valuable tool for assessing the progress of a DNA-templated nanomaterial synthesis. The most useful spectroscopic techniques for my work in DNA-templated nanofabrication are ultraviolet and visible light absorption spectroscopy (UV-Vis), X-ray photoelectron spectroscopy (XPS) and energy dispersive X-ray analysis (EDX).

#### 1.3.1.1. Ultraviolet and Visible Light Absorption

UV-Vis spectroscopy [267] probes electronic transitions that result from the absorption of photons with wavelengths between 200-800 nm. A source with a broad emission spectrum sends light through a solution of the species of interest. Light that passes through the sample is sent into a monochromator that disperses the beam according to wavelength and maps these onto a detector element. The detected array of

intensities is compared with those obtained when the sample is replaced by an analytical blank. The result is a UV-Vis spectrum, a plot of absorbance ($A_\lambda$) of the analyte vs. wavelength. **Fig. 1.4** shows absorption spectra of DNA solutions of different concentrations.

For systems with non-interacting chromophores, $A_\lambda$ is linearly proportional to the concentration, as shown in **Equation 1.6**, where $c$ is the concentration of the analyte, $\varepsilon_\lambda$ is the molar absorptivity at a given wavelength and $b$ is the sample thickness.

$$A_\lambda = \varepsilon_\lambda c b \qquad \text{[Eq. 1.6]}$$

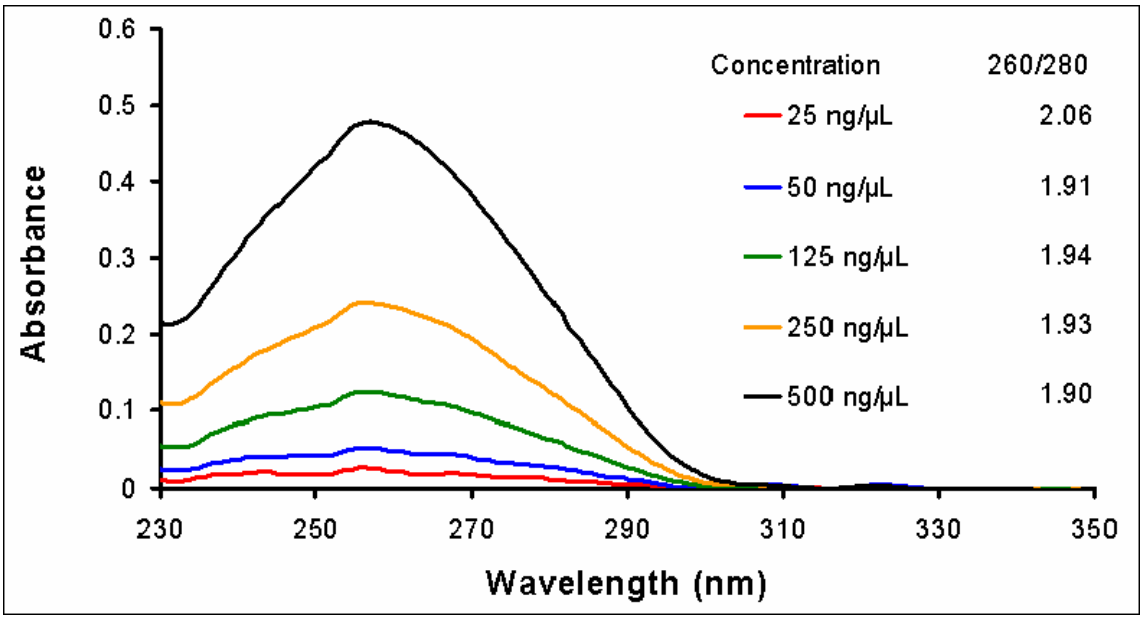


**Figure 1.4.** UV-Vis spectra of DNA solutions of different concentrations.

In molecular biology, UV-Vis spectroscopy is used to determine the concentration and purity of dilute solutions of DNA. The aromatic nucleobases in the DNA absorb 260 nm light, while peptide residues, which are common contaminants in DNA from natural sources, absorb at 280 nm. Thus, the ratio of $A_{260}/A_{280}$ is a gross measurement of DNA purity, and values of between 1.8 and 2.2 indicate pure DNA [268]. Further, given the

260 nm absorbance, the concentration of DNA in solution can be calculated using **Equation 1.7**,

$$[mM] = \frac{A_{260} D_f M_f}{MW} \qquad \text{[Eq. 1.7]}$$

where $[mM]$ is the milimolar concentration of the DNA solution, $D_f$ is the dilution factor between the measured aliquot and the actual stock solution, $M_f$ is a mass to concentration conversion factor equal to 33,000 for ssDNA and 50,000 for dsDNA, and $MW$ is the molecular weight of the DNA analyzed.

In DNA-templated nanofabrication, UV-Vis is useful for determining the concentration of DNA solutions, measuring the yields of enzymatic manipulations and preparing stoichiometric mixtures of distinct types of DNA molecules for self-assembly. Importantly, DNA measured by UV-Vis may get damaged oxidatively or become contaminated, so it should not be utilized for subsequent nanofabrication or biochemical protocols.

#### 1.3.1.2. X-ray Photoelectron Spectroscopy

XPS is an ultrahigh-vaccum ($<10^{-9}$ torr) surface analysis technique that probes the kinetic energy distribution of electrons ejected from solids by interactions with monochromatic X-ray photons. Kai M. Siegbahn received the 1981 Nobel Prize in Physics for the development of this technique [269].

Inside an XPS instrument [269-271], an X-ray beam is generated by accelerating electrons from a tungsten filament into an aluminum or magnesium target. Elastic and inelastic energy transfer occurs, resulting in a broad distribution of emitted X-ray energies, with a few very intense, element-characteristic X-ray emission peaks

originating from resonant transitions of the 1s electrons in the target atoms. One of these intense lines is selected, filtered and allowed to interact with the analyte in the sample chamber. As an X-ray photon penetrates the sample, it can transfer its energy to tightly bound inner-shell electrons in the material, exciting them enough to escape from the entire sample. The photoelectrons thus produced are guided by electromagnetic lenses through a scanned electron velocity selector and finally reach an electron multiplier, which counts the number of electron hits as a function of electron kinetic energy. The difference between the total energy of the incident X-ray photon and the residual kinetic energy of the ejected photoelectron is called the binding energy. Electron binding energies are characteristic of the parent atoms, and experimentally measured shifts in these energies provide information about the chemical bonding of the atom. An XPS spectrum (**Fig. 1.5**) is a plot of the number of electrons incident at the detector vs. binding energy.

X-ray photons interact weakly with matter and can excite electrons deep inside the sample. Still, XPS is a surface-selective technique because only those photoelectrons generated in the top ~10 nm of a solid are able to escape from the sample and be detected. The lateral resolution of XPS is limited by the size of the X-ray beam, which is typically on the order of

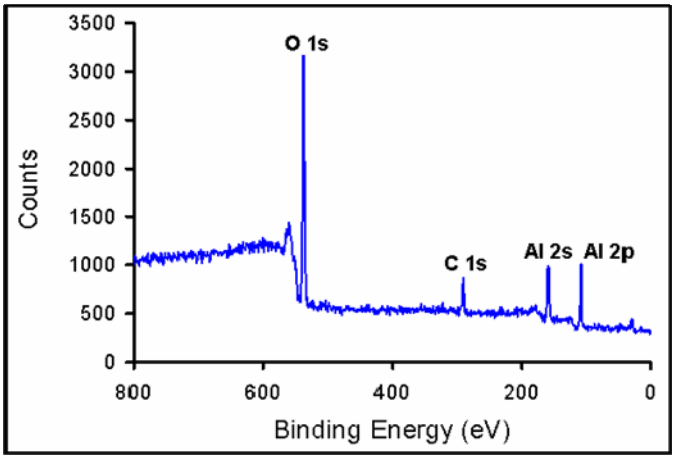


**Figure 1.5.** XPS of a thick aluminum film showing photoelectrons emitted with binding energies characteristic of aluminum, carbon and oxygen.

several micrometers [272]. Moreover, the low scattering cross-section of X-rays with matter complicates XPS analysis of isolated nanostructures on surfaces, because common X-ray sources do not have a high enough photon density to obtain appropriate signal. Synchrotron X-ray sources have sub-micron resolution and are sufficiently bright to analyze nanostructrures on surfaces but their availability is limited [273, 274]. Other experimental techniques such as EDX (Section 1.3.1.3) are better suited to study the elemental composition of single nanostructures.

In DNA-templated nanofabrication, the coarse lateral resolution of XPS and its insensitivity to individual nanostructures limit its application to the characterization of the surfaces used for DNA alignment. Importantly, XPS analysis of these surfaces is useful to verify modification of the substrates with self-assembled monolayers, spin-coated polymers, and thin (<10 nm) metal films.

#### 1.3.1.3. Energy-dispersive X-ray Analysis

EDX is a fundamental tool for elemental analysis in materials science. EDX is used routinely to study microphase segregation in metal alloys and ceramic composites, and to understand how composition and microstructure affect the properties of these materials [275-277].

During an EDX experiment [278, 279] an energetic electron beam impinges on the atoms of the analyte, ejects inner-shell electrons, and leaves these atoms in a highly unstable, singly ionized state. These ions gain partial stabilization when electrons from their own outer shells are used to occupy core vacancies, emitting the excess energy as a characteristic X-ray photon, which can be counted and energy-analyzed by the EDX detector. Analogously to XPS, the energy of the detected X-ray can be utilized to identify

the atom. Unlike XPS, the energy resolution of EDX is insufficient to discriminate between chemical bonding states of the parent atom.

EDX analyzers are coupled to scanning and scanning-transmission electron microscopes to take advantage of the tightly focused, highly coherent electron beam used for imaging. Cold-cathode, field-emission electron guns produce high beam currents which translate into large X-ray signals from the sample. These bright sources can be used in the generation of X-ray maps, which are multidimensional micrographs that combine topographical and compositional information in the same image [280]. X-ray maps are also used to calculate relative concentrations of different components on surfaces [281]. Furthermore, the exquisite spatial and dynamic control of the electron beam in scanning electron microscopes allows compositional EDX analysis of individual micro- and nanostructures [212, 282]. For such work the electron beam is either stationed at a single point within the sample, translated over a specific path, or raster-scanned to excite a selected area. The timing of these beam operations can be controlled to allow collection of adequate signals at each point of interest. The spatial resolution in EDX is directly proportional to the beam acceleration voltage, and inversely proportional to the sample thickness. EDX data with spatial resolution on the order of ~10 nm can be achieved using high-energy (~200 keV) electron beams and thin (<50 nm) samples.

EDX analysis is an important tool in the characterization of DNA-templated nanomaterials, as EDX can profile the elemental composition of selected areas of individual nanostructures (**Fig. 1.6**). Unfortunately, biological materials and beam-sensitive features may not produce sufficient X-rays to be studied by EDX before heat-induced sample damage occurs. Deposition of carbonaceous materials on the sample

during EDX analysis also obscures individual nanostructures and skews the results toward higher carbon content. Sample damage and carbon contamination can be reduced by decreasing the energy of the electron beam, although this decreases resolution and limits the range of observable X-ray energies from the sample.

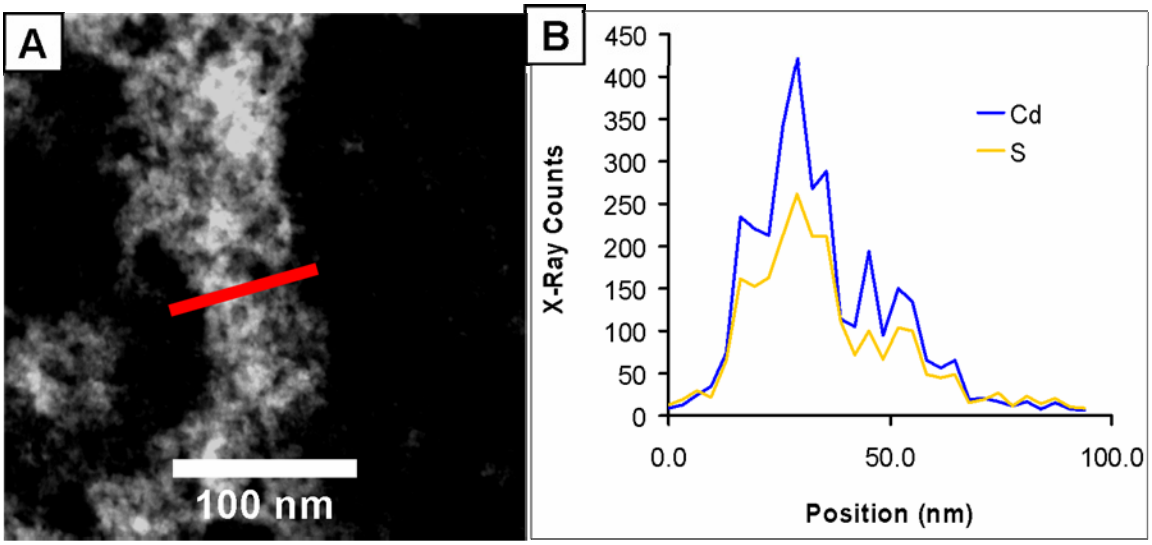


**Figure 1.6.** EDX profile of the elemental composition of an individual DNA-templated CdS nanostructure. **(A)** STEM image of the nanostructure under analysis. The red line marks the path of the excitation beam over the nanostructure. **(B)** Plot of the number of collected Cd and S characteristic X-rays as a function of position along the red line in **(A).**

### 1.3.2. Scanning Probe Microscopy

#### 1.3.2.1. Development of Scanning Probe Microscopy

In 1981 Heinrich Rohrer and Gerd Binnig at IBM's Zurich research center developed the scanning tunneling microscope (STM) [283-286], and in so doing launched the revolutionary field of scanning probe microscopy. For their invention, Rohrer and Binnig were awarded the 1986 Nobel Prize in Physics [286]. In contrast to the electron microscope, which compresses three-dimensional space into a two-dimensional plane, STM datasets are three-dimensional representations of surfaces, or range images, where the color of each pixel encodes the local value of a measured property.

An STM images individual atoms on electrically conductive surfaces by establishing a tunneling current between an atomically sharp metal tip and surface atoms. The magnitude of the tunneling current is modulated by the tip-surface separation and the spatial overlap of electron wavefunctions between the terminal atom on the tip and the closest atom on the surface. Controlled scanning of the STM tip over the sample is performed by a high-precision piezoelectric tip translation system coupled to fast feedback electronics that monitor the tunneling current [286, 287]. STMs can operate in two main modes: constant current or constant height. In constant current mode, the feedback loop actuates the piezoelectric to keep the sample-tip current constant during scanning. Constant current STM images contain topographical information. In constant height mode, the tip is held at fixed height during scanning, and the value of the tunneling current is monitored. Constant height STM images contain information regarding the electronic states of the sample. The STM tip can also apply localized electric fields to trap individual atoms and translate them across the surface [287-289].

#### 1.3.2.2. Atomic Force Microscopy

In 1986, Gerd Binnig, Calvin Quate and Christoph Gerber developed AFM [290], the first and most popular derivation of STM. The first AFM scanned a surface with a sharp diamond stylus mounted on a conductive cantilever, while an STM registered the deflection of the cantilever due to attractive and repulsive atomic forces between the sample and tip. This hybrid setup allowed direct atomic resolution study of the topography of insulating samples. Modern AFM instruiments utilize optical signal transduction which is faster and tolerates larger cantilever deflections than the STM,

simplifies the construction and operation of the apparatus [291-293], and allows imaging in liquid environments [294, 295].

**Fig. 1.7** shows a typical AFM setup. For imaging, the sample and tip are set in relative motion by means of two sets of piezoelectric actuators in a raster-scan pattern, while carefully controlling tip-sample separation. A third piezoelectric causes controlled oscillatory motion of the cantilever for certain imaging modes. The optical transduction system comprises a low power diode laser that is reflected off the top surface of the cantilever onto an array of photodetectors, which track and encode the position of the beam (and hence, the Z position of the tip) as voltage differences. These signals are processed to produce a topographical map of the surface and to monitor the tip-sample separation.

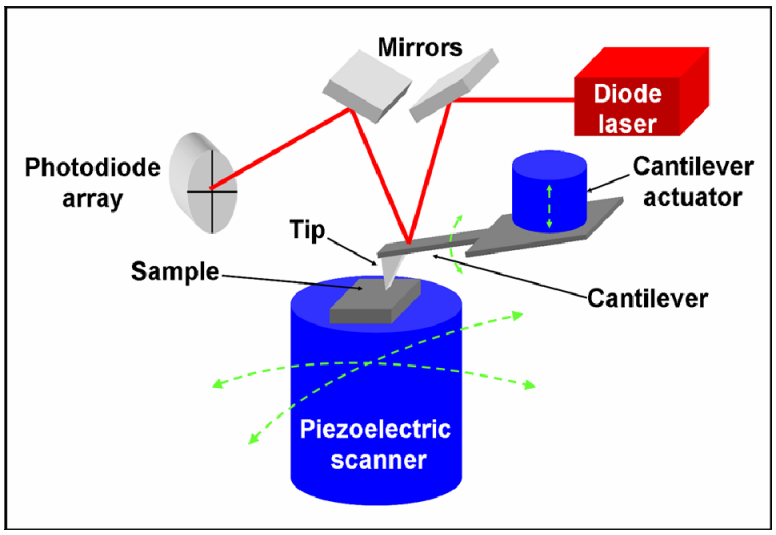


**Figure 1.7.** Typical AFM setup. The piezoelectric scanner supports the sample and bends in orthogonal directions (horizontal green arrows) to create a raster-scan motion. The slight curvature of the sample path "bends" the collected images but is corrected through software processing. The cantilever piezoelectric resonates the tip (vertical green arrows) for imaging in tapping mode. The optical transduction system reflects the laser beam from the cantilever onto the photodiode array.

Other setups (unlike **Fig 1.7**) combine the scanning and tip-vibrating piezoelectric elements into one "AFM head", and are designed so the head can be placed directly over

large samples, set on optical microscopy stages or used in combination with other characterization instruments.

#### 1.3.2.3. Tapping and Contact Mode AFM

The original AFM instrument operated in two types of imaging modes [290, 296]. In one, either the cantilever or the sample was driven vertically at a resonance frequency while scanning to provide a modulated tunneling current signal. In the second mode, the sample was scanned and the cantilever was deflected to keep the tunneling current constant. Modern AFM vendors have developed other imaging methods based on the ideas of constant or modulated feedback. Contact and tapping mode imaging are the most direct and widely used implementations of the early AFM imaging work.

Contact mode imaging maintains a constant deflection of the cantilever as it presses against the sample surface during scanning [296]. Uneven topography modifies the cantilever deflection and displaces the laser across the photodetector. The feedback loop then actuates the sample or tip holder until the deflection set-point is reached. Contact mode has the highest imaging resolution because the tip and substrate are in continuous contact. Importantly, imaging in contact mode may damage the tip and the sample depending on the chosen deflection set-point and the nature of the surface. Such damage may not be detected easily, and contact images can differ from the original sample or contain tip-induced artifacts. In general, biological samples cannot be imaged in contact mode because they rarely can withstand the mechanical drag of the tip [297]. Even hard samples deposited on flat substrates are difficult to image in contact mode if adhesion to the surface is low, because sample can be swept off during scanning.

Contact AFM is useful for lattice-resolved studies on crystalline solids [298, 299], for measurements of the mechanical properties of materials [300, 301] and for general imaging of inorganic and polymer surfaces [302-305]. In my DNA-templated nanofabrication experiments, I found that contact mode imaging would fragment fully formed DNA-templated nanomaterials. Importantly, an extension of contact AFM, denominated AFM lithography [306-308], is useful for manipulating DNA and DNA-templated nanomaterials. AFM lithography lets the user apply localized shearing forces on a sample by moving the tip in the X, Y and Z directions to cause bending or breakage of surface features [309, 310]. **Fig. 1.8** shows how AFM lithography has been used to sever a thin DNA-templated nanowire in order to characterize electrical properties before and after the cutting.

Tapping mode AFM imaging is an intermittent-contact technique that preserves the structure of delicate samples [297, 311]. Imaging in tapping mode implies a loss of resolution since the tip is not always sensing the sample. In practice, this effect may be small when compared to the often severe image degradation due to tip wear in contact mode. Tapping mode can image soft materials or weakly adsorbed isolated nanostructures on surfaces with reduced tip wear and sample damage.

During tapping mode imaging the cantilever is oscillated slightly below its resonance frequency and the amplitude of the oscillation (amplitude set-point) is monitored as the tip comes in proximity to the sample. The surface and tip are considered "engaged" when the tip oscilation amplitude reaches a user-defined percentage, normally ~90%, of the free oscillation magnitude. For imaging, the feedback loop maintains the tip oscillation amplitude constant by raising or lowering the tip or the sample. Ideally, when

the system is engaged the tip and the sample interact only briefly at the moment in the oscillation cycle where the tip has the lowest kinetic energy, so damage to the tip and sample is reduced. In practice [296], long-range attractive and repulsive tip-substrate interactions may complicate imaging. The amplitude set-point can be increased to overcome these effects, at the cost of longer and more energetic contact between tip and sample.

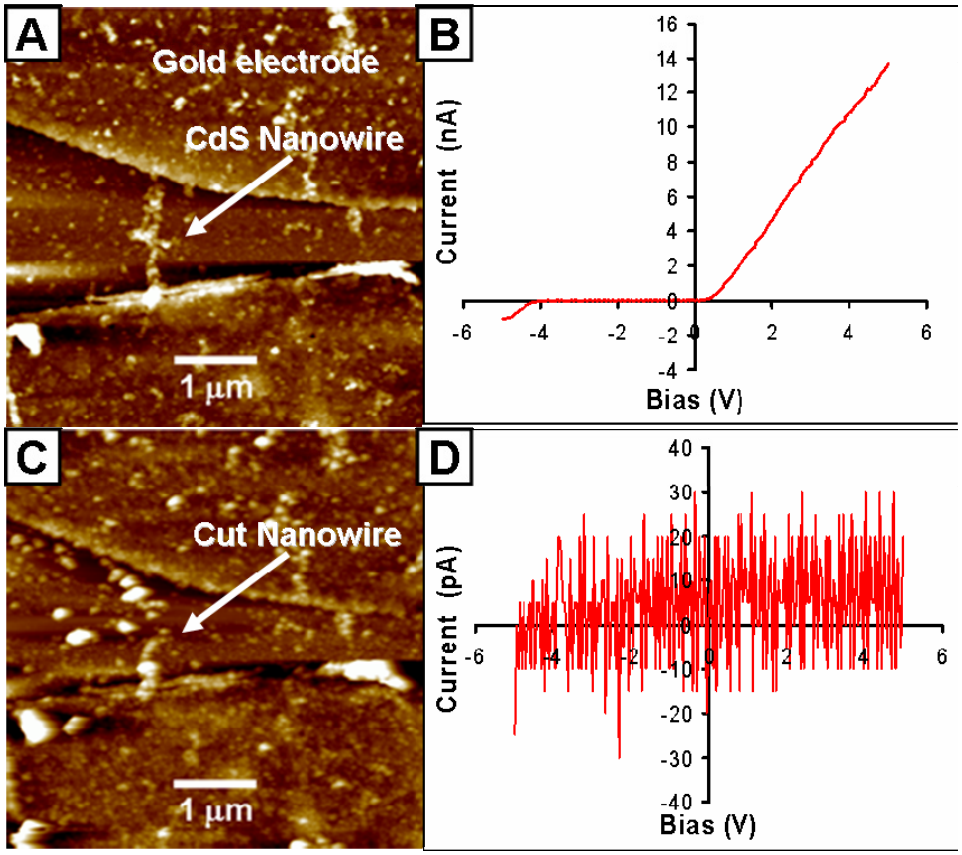


**Figure 1.8.** Cutting a DNA-templated CdS nanowire using AFM lithography. **(A)** Tapping mode AFM image of the intact nanowire between gold microelectrodes. **(B)** Diode-like current-voltage characteristics of the nanowire. **(C)** Tapping mode AFM image of the nanowire after cutting with an AFM tip in lithography mode. The tip was translated from left to right over the surface and the nanowire at a speed of at 100 nm/s while maintaining a cantilever deflection of 8 V. **(D)** The current-voltage relation after the cut shows more than 1000x reduction in conductance.

Tapping mode AFM is used to image biological structures on surfaces, including proteins [312-316], nucleic acids [87, 232, 317-320] and live cells [321-325] in air or

liquid environments. Tapping mode AFM tips can be end-functionalized with biological agents to probe interactions with corresponding receptors [326-328]. AFM tips are also functionalized chemically to obtain images with chemical affinity and topographic contrast [326, 329, 330].

Tapping mode AFM is the main imaging tool I used at all stages of the DNA-templated nanofabrication process. AFM imaging in this mode does not appreciably disturb surface-aligned DNA molecules or DNA-templated constructs. Furthermore, the resolution of tapping mode AFM in the Z-direction is sufficient for distinguishing between ssDNA and dsDNA [240] and for detecting changes in the height of DNA molecules as they are ion-exchanged with transition metal cations [212]. Finally, tapping mode AFM is valuable for studying the morphology or structural characteristics (such as height, grain size, roughness, etc.) of DNA-templated nanomaterials.

#### 1.3.2.4. Experimental Considerations that Limit Resolution in AFM

The imaging resolution in AFM in the Z-direction is <1Å [291]. This value is influenced by the quality of the piezoelectric actuators and their controller electronics, and by the effectiveness of the vibration isolation system around the instrument. High resolution in the vertical direction is achieved readily by placing the instrument in a dedicated location protected from thermal drift, air currents, and mechanical and acoustic vibrations. Using active vibration suppression systems [240] or setting up the instrument on a suspended platform [331] are effective manners of eliminating high-frequency vibrations from collected images.

The resolution in the X-Y plane in an AFM image is typically on the order of several nanometers [332]. This limit is set primarily by the radius and cone half angle of the imaging tip. The finite size of the imaging tip also causes a number of artifacts in AFM images. For instance, topographic features that are small in the Z-direction and have lateral dimensions narrower than the tip radius are imaged to be at least as wide as the tip itself. Also, multiple features that are separated by less than a tip radius are imaged as a merged single entity, and surface dips or grooves that are smaller than the tip radius may not be detected either. Moreover, tall structures can interact with the sides of the imaging tip and appear even wider than shorter features, such that their imaged contours may be distorted heavily by convolution with the tip shape. These artifact effects become more prevalent as the tip wears down and becomes broader or more irregular in shape. In spite of tip-induced imaging artifacts, which are detected readily by experienced users, AFM is a widely used surface characterization technique that provides nanometer-scale topographic information from a variety of materials and requires little sample preparation.

Vendors of AFM tips have developed microfabrication processes that produce probes with improved aspect ratio, reduced end radius and smaller cone half angle. Such sharp tips enhance lateral resolution and minimize artifacts caused by interactions of the sample with the tip side. Conventional, less expensive AFM tips can also be enhanced temporarily by carbon nanotube attachment [333]. The modified tip performs well for substrates with low affinity for the carbon nanotube, and the lateral resolution of such a tip is 1-2 nm [332]. Alternatively, carbon nanotubes can be grown directly on AFM tips

[334-336], or soldered to probes using an electron beam [337] for more permanent tip modification.

Finally, the sampling and scanning rates also impact AFM resolution. Depending on the size of the image and the roughness of the surface, the number of sampled points may not be enough to fully represent the topography [338]. In such a case the image size can be reduced, or a different instrument with higher sampling capacity must be used. Additionally, the finite response time of scanners may cause smoothing of high-frequency data at high scanning speeds. Monitoring changes in the power spectrum of an image as a function of scanning rate and image size can help to optimize the representation of the surface.

### 1.3.3. Electron Microscopy

In 1928 Ernst Ruska was working on focusing electron beams using magnetic fields produced by a direct current in a wire coil. He discovered that coiling the wire around a doughnut-shaped iron "polepiece" increased the focusing power of his "electron lens" significantly. In 1933 Ruska fabricated a multi-lens electron microscope that imaged at magnifications greater than diffraction-limited optical microscopy. In 1986 Ruska shared the Nobel Prize in Physics for his work in electron optics [339].

#### 1.3.3.1. Imaging Components of the Electron Microscope

The imaging components of an electron microscope are the electron source, the electromagnetic lenses, and the limiting apertures. Other necessary microscope components that will not be discussed here include the shielding that protects the operator from X-rays generated during manipulation of the high-energy electron beam, the

high-voltage supply that feeds into the electron source, electron detectors, the temperature control system, and the ultrahigh vacuum system.

Modern electron microscopes utilize a field-emission electron gun to produce a bright and highly coherent electron beam [340]. Inside the gun, the field emitter is a long thin-pointed tungsten needle held at several kilovolts of negative potential relative to an extraction electrode. Electrons at the tip experience electric fields on the order of several volts per nanometer and can tunnel out of the metal. These extracted electrons are accelerated by another set of electrodes to a user-selected potential between 1-1000 kV and focused into the microscope column as the primary beam.

Inside the column [341], several metal apertures and electromagnetic lenses collimate the electron beam to reduce spherical aberrations and narrow the energy distribution to reduce chromatic aberrations. Asymmetric electromagnetic coils adjust the shape of the beam spot to control astigmatism. Importantly, modern electromagnetic lenses are still coils of wire wound around hollow, water cooled iron and cobalt pole pieces, similar to Ruska's initial design.

The conditioned primary beam interacts with the sample, and the generated signals are selected and registered by another set of lenses, apertures, charged grids, and detectors. The manner in which the beam probes the sample depends on the type of electron microscope used [342]. In SEM and scanning-transmission electron microscopy (STEM), a tightly focused primary beam raster-scans the sample plane by means of electromagnetic deflection coils. This allows controlled generation and collection of signals from selected regions of the sample. In non-scanned TEM, the beam is defocused to illuminate the viewing area of the sample. This set up allows collection of bright-field

images, dark-field images and electron diffraction patterns from a specimen. **Fig. 1.9** shows basic schematics of TEM, STEM and SEM instruments.

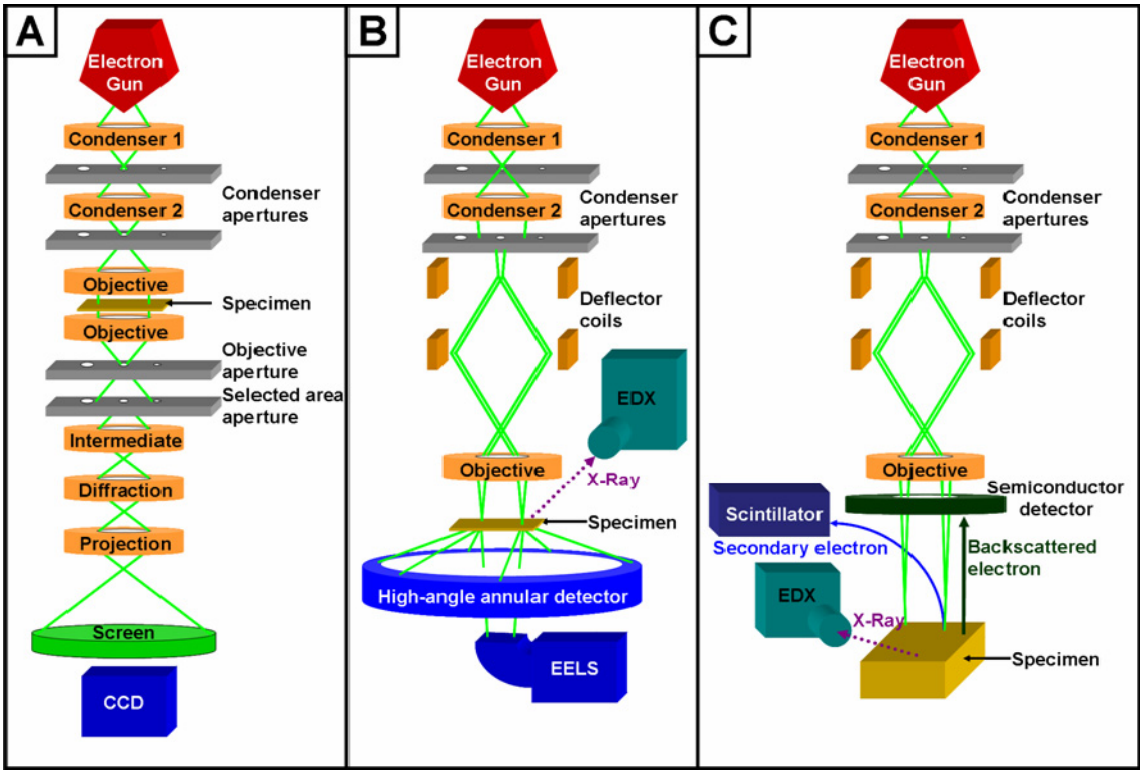


**Figure 1.9.** Schematic representation of the optical components of TEM, STEM and SEM. **(A)** TEM optics form a defocused, parallel beam to illuminate the sample, which sits inside the objective lens. The "intermediate lens" is an array of variable strength lenses that achieves magnification. The objective aperture selects diffracted beams to form images. The diffraction lens causes the microscope to produce images or diffraction patterns. The screen can be lifted to capture images with a CCD. **(B)** STEM forms a focused probe that is scanned over the sample using deflective coils. Magnification is achieved by reducing the scanned area. Strongly diffracted beams are collected to form STEM images. Transmitted electrons are analyzed for energy losses. An EDX attachment collects sample X-rays. **(C)** SEM uses a scanned, narrow probe to image thick samples. A backscattered electron detector, a secondary electron detector and an EDX detector can be used individually or in tandem to form multidimensional images. Magnification is achieved like in STEM.

### 1.3.3.2. Electron–Specimen Interactions

In electron microscopy the wave-particle duality becomes readily apparent. The highly energetic primary beam electrons that penetrate the specimen may behave as particles that collide with individual atoms, or may act as waves that interact with the total irradiated area of the sample. Particle-like interactions include elastic and inelastic

scattering, while electron diffraction patterns and the formation of image contrast in TEM are manifestations of wave-like electron–specimen interactions.

Elastically scattered primary-beam electrons [343] come in close proximity to atomic nuclei in the sample, where they experience forces that modify their trajectory without changing their energy significantly. These electrons are critical in TEM. Indeed, the thin (<100 nm) specimens used in TEM are called “electron-transparent” as the majority of the primary beam electrons go through the sample without scattering. A small number of the primary electrons experience one elastic scattering event, typically with forward deflection through a small angle (<0.5°), and pass through the sample. The remaining elastically scattered electrons experience more severe forward deflections, and a few are backscattered up through the sample. These backscattered electrons are not collected in TEM but are an important signal for SEM instruments. Both scattered and non-scattered electrons can also behave as waves, and their interference produces image contrast in TEM.

Inelastically scattered electrons generate many different types of analytical signals [344], including photons with energies from the X-ray to the infrared range, and cause the ejection of secondary and Auger electrons. Inelastic electron interactions are most important for thick samples such as those imaged by SEM.

Energetic primary beam electrons can penetrate several microns into a bulk sample and are scattered multiple times, interacting with a relatively large volume of material, which is denominated the interaction or excitation volume [345]. Inside this interaction volume, the primary beam electrons collide with valence and core-level electrons from atoms in the sample and cause electronic excitation and atomic ionization.

A fraction of the electrons ejected from ionized atoms within the interaction volume can emerge from the sample as secondary electrons, a name given since they do not originate from the primary beam. Secondary electrons are produced most effectively in the topmost layers of the sample, especially at raised or sharp-edged topographic features. Secondary electrons in SEM typically have kinetic energies <50 eV, and must be pulled toward the detector using positively charged grids placed close to the sample. Secondary electrons are blocked readily by surface topography, creating shadowing effects (contrast) in SEM images.

Ionized sample atoms which have lost core electrons are highly unstable and relax by filling their vacancies with outer-shell electrons as explained in Section 1.3.1.3. The energy difference between the outer-shell electron and the vacancy it occupies is liberated in the form of an X-ray photon of energy characteristic to that element [346]. Unlike secondary electron generation, X-ray emission is not surface-selective because X-rays generated anywhere in the interaction volume can escape from the sample easily.

Diffraction of electrons by thin crystalline samples in TEM can provide useful local crystallographic information. To operate in diffraction mode in TEM, the diffraction lens is activated and the intermediate lens is focused on the plane of the objective aperture (see **Fig. 1.9A**) instead of being focused in the plane of the selected area aperture, which is the configuration for imaging. In modern microscopes this operation is accomplished with the push of a button.

Incident electrons from the primary beam behave as waves that diffract from the collection of nuclei in a crystalline sample. Each plane of atoms acts as the source of a new diffracted wave with identical wavelength to the original, generating a set of

diffracted beams that propagate only in spatial directions for which constructive interference occurs. Diffracted beams are collected at an imaging detector as a pattern of very fine spots of different intensities on a dark background; modern microscopes label the diffraction patterns with a scale bar in units of $nm^{-1}$. Using that scale, the inverse of the measured distance from the central beam to any diffracted spot gives the spacing between the planes that generated that selected spot, and the **g** vector, which joins the central beam to the selected diffraction spot, is orthonormal to that particular family of atomic planes in the sample. Careful examination of the interplanar distances and angles in the diffraction pattern allows assignment of the local crystalline structure. The crystalline orientation of the sample may also be determined unequivocally by comparing data from three diffraction patterns taken from the same sample area but using different tilt angles with respect to the incoming electron beam.

Polycrystalline samples give diffraction patterns formed by concentric bright rings on a dark background, indicating that the incoming electron waves have encountered numerous crystals with varied orientations which project rotated single-crystal diffraction patterns that superimpose at the detector plane. The radius of the concentric rings gives the interplanar distances but the **g** vectors cannot be determined individually.

Furthermore, with selecting apertures it is possible to form TEM images from only one of the diffracted beams by using the objective aperture to block all other diffraction spots in a single-crystal pattern or other rings in the polycrystalline case. The result is a dark-field image that shows those structural features of the specimen (crystal planes and other defects) that contributed to the aperture-selected diffracted beam.

Dark-field is the basic imaging mode of STEM instruments, which ignores the directly transmitted beam and forms images by collecting all strongly diffracted beams in a high-angle annular detector (HAAD), as shown in **Fig. 1.9B**.

#### 1.3.3.3. SEM

SEM provides a fast alternative to AFM for the examination of large areas containing DNA-templated nanostructures. Indeed, field-emission SEM can analyze surfaces at magnifications and resolutions comparable to AFM in a fraction of the time, but SEM is restricted to conductive substrates. Thus, DNA-templated nanostructures on mica, glass, or thick (>200nm) oxide on silicon cannot be observed by SEM. Furthermore, SEM inspection of surfaces typically deposits a carbon layer of variable thickness that precludes subsequent AFM observation or manipulation of the surface nanostructures. Also, SEM electron beams can cause evaporation of metal nanoparticles from a sample. Finally, SEM provides only a two-dimensional projection of the nanostructures on the substrate, and measurement of Z-dimensions by SEM is neither precise nor straightforward when compared to AFM.

In spite of these limitations, SEM imaging of nanostructures is useful because SEM can collect larger image fields than AFM and SEM images do not have tip-induced artifacts. Importantly, only secondary electron imaging is useful for characterization of DNA-templated nanomaterials since these nanostructures are too narrow and thin to be efficient sources of backscattered electrons. For good imaging, the accelerating potential of the electron beam must be kept small to minimize specimen penetration and interaction volume. This limits the signal from under or around the nanostructure and improves edge definition. Beam energies between 2-5 keV give the best results, although

energies up to 10 keV can be tolerated. Additionally, the spot size of the beam must be adjusted to the minimum setting to reduce carbon contamination and sample damage.

SEM coupled with EDX is useful in examining the elemental composition of individual DNA-templated nanostructures on surfaces. For EDX analysis it is necessary to use an accelerating potential >10 kV so primary beam electrons have enough energy to produce $K_\alpha$ X-rays from first-row transition metals; beam energies of at least 25 kV are needed for $K_\alpha$ emission from second-row transition metals. The spot size of the electron beam also needs to be increased to adjust the amount of X-rays generated and the detector dead time.

When all these conditions are met, SEM imaging and related EDX studies can be a great asset in the characterization of DNA-templated nanomaterials. **Fig. 1.10** shows AFM and SEM data collected from a single DNA-templated silver nanostructure.

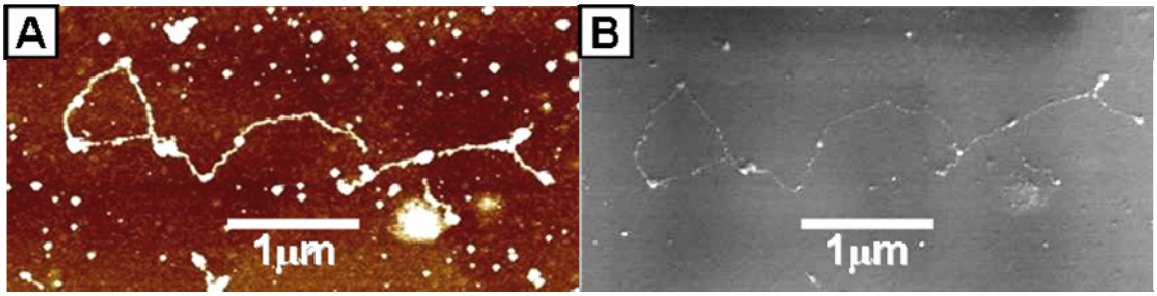


**Figure 1.10.** Tandem characterization of the same DNA-templated silver nanostructure with AFM and SEM. **(A)** Tapping mode AFM image showing DNA-templated and non-templated deposits. Z scale is 5 nm. **(B)** SEM of the same area shows fewer deposits corresponding to metal particles, suggesting that many of the non-templated features in **(A)** are not produced by the plating process.

### 1.3.3.4. TEM and STEM

Both AFM and SEM are useful for observing the size and shape of DNA-templated materials, and SEM-coupled EDX can analyze the elemental composition of individual nanostructures. However, the lateral resolution of AFM and

SEM is on the order of a few nanometers; moreover, neither approach allows the study of the internal structure of DNA-templated deposits. In contrast, TEM and STEM provide the ability to look inside materials and investigate their crystallography and composition. **Fig. 1.11A** shows a TEM image of a DNA-templated CdS nanowire in which the structure of the material is revealed as a continuous chain of randomly oriented nanocrystals, showing lattice fringes with spacings characteristic of the hexagonal (Wurtzite) phase of CdS. **Fig 1.11B** shows a selected area electron diffraction pattern from the material, again with spacings consistent with the Wurtzite structure. **Fig 1.11C** is an analysis of the observed spacings with respect to hexagonal CdS, cubic CdS and cubic CdO that clearly establishes the presence of hexagonal CdS. Neither AFM nor SEM could provide this information.

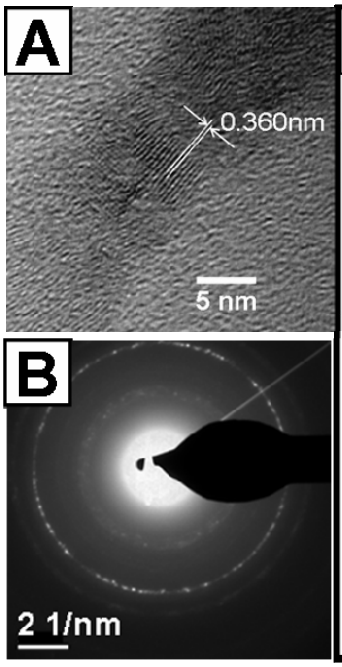


C

| Structure | h | k | l | Expected d (nm) | % Match |
|---|---|---|---|---|---|
| CdS (Hex) | 1 | 0 | 0 | 0.359 | 100% |
| | 0 | 0 | 2 | 0.336 | 97% |
| | 1 | 0 | 1 | 0.316 | 100% |
| | 1 | 0 | 2 | 0.245 | 100% |
| | 1 | 1 | 0 | 0.207 | 96% |
| CdS (Cubic) | 1 | 1 | 1 | 0.336 | 97% |
| | 0 | 0 | 2 | 0.291 | 99% |
| | 2 | 0 | 2 | 0.206 | 97% |
| | 1 | 1 | 3 | 0.175 | 0% |
| | 2 | 2 | 2 | 0.168 | 101% |
| CdO (Cubic) | 1 | 1 | 1 | 0.271 | 107% |
| | 0 | 0 | 2 | 0.235 | 104% |
| | 2 | 0 | 2 | 0.166 | 102% |
| | 1 | 1 | 3 | 0.142 | 0% |

**Figure 1.11.** Use of TEM for elucidation of the crystalline structure of individual DNA templated nanostructures. **(A)** Lattice-resolved, bright-field TEM image of a DNA-templated CdS nanowire showing a chain of ~10 nm diameter nanoparticles. **(B)** Electron diffraction pattern from multiple wires. **(C)** Comparison of interplanar spacings for hexagonal CdS, cubic CdS, and cubic CdO. Both cubic CdS and CdO lack the <100> plane spacing and show other spacings not observed in **(B)** (0% match).

**Fig. 1.12** is a collection of STEM images of several DNA-templated nanomaterials with their corresponding characteristic X-ray peaks obtained by *in situ* EDX analysis. Advantages of performing EDX with STEM vs. SEM include the reduction of background signals from the substrate, and greatly improved spatial resolution.

Some important disadvantages of the use of TEM or STEM for characterization of DNA-templated nanostructures include: (1) the entire DNA-templated nanofabrication process has to be carried out on fragile ~50-nm-thick carbon films deposited on TEM grids; (2) copper from the grid may contaminate the DNA-templated deposit; and (3) TEM and STEM are limited in analyzing large sample areas. Thus, a judicious combination of AFM, SEM, TEM and STEM for characterization of DNA-templated nanomaterials is more desirable than the use of any one isolated technique.

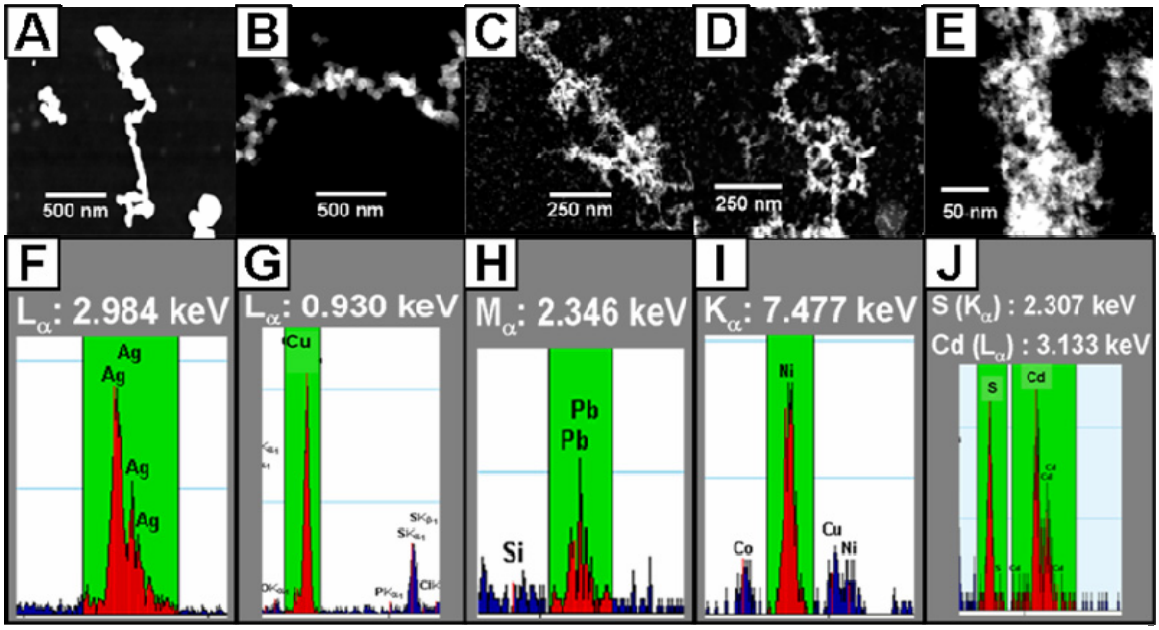


**Figure 1.12.** STEM and EDX characterization of diverse DNA templated nanomaterials. **(A-E)** STEM HAAD images of DNA-templated nanostructures made from **(A)** silver, **(B)** copper, **(C)** lead, **(D)** nickel, and **(E)** cadmium sulfide. **(F-J)** Portions of EDX spectra collected from the samples in **(A-E)** showing characteristic X-ray peaks that confirm the composition of the synthesized nanostructures.

## 1.4. Dissertation Overview

I have researched the use of surface-aligned DNA molecules as templates for nanofabrication. Chapter 2 details a method for blocking negatively charged silicon and silica surfaces with alkali metal cations to reduce non-specific surface deposition during copper and silver electroless plating of DNA molecules aligned on these substrates. Chapter 2 also shows for the first time specific metal (silver) deposition on ssDNA molecules aligned on surfaces. Chapter 3 illustrates the design, assembly and AFM characterization of a branched DNA motif, as well as its selective labeling with single streptavidin molecules. This chapter also shows TEM investigations of the selective coating of these branched DNA constructs with silver and copper metal. The theme of DNA-templated metals and proteins continues in Chapter 4, which describes the synthesis and characterization of DNA-templated nickel nanorods and their use as templates for the reversible deposition of histidine-tagged phosducin-like protein. Chapter 5 introduces the concept of DNA shadow nanolithography, which combines angled deposition of thin films and anisotropic etching to form DNA-free, templated trench patterns on surfaces. These trenches have linewidths <30 nm and can be used to template the fabrication of metal lines or form enclosed nanopores. Chapter 6 completes this work with conclusions and a discussion of future directions for DNA-templated nanomaterials research.

## 1.5. References


1. Darque-Ceretti, E.; Helary, D.; Bouquillon, A.; Aucouturier, M. Gold Like Lustre: Nanometric Surface Treatment for Decoration of Glazed Ceramics in Ancient Islam, Moresque Spain and Renaissance Italy, *Surf. Eng.* **2005**, *21*, 352-358.
2. Padovani, S.; Sada, C.; Mazzoldi, P.; Brunetti, B.; Borgia, I.; Sgamellotti, A.; Giulivi, A.; D'Acapito, F.; Battaglin, G. Copper in Glazes of Renaissance Luster Pottery: Nanoparticles, Ions, and Local Environment, *J. Appl. Phys.* **2003**, *93*, 10058-10063.
3. Padovani, S.; Puzzovio, D.; Sada, C.; Mazzoldi, P.; Borgia, I.; Sgamellotti, A.; Brunetti, B.G.; Cartechini, L.; D'Acapito, F.; Maurizio, C.; Shokoui, F.; Oliaiy, P.; Rahighi, J.; Lamehi-Rachti, M.; Pantos, E. XAFS Study of Copper and Silver Nanoparticles in Glazes of Medieval Middle-East Lusterware (10th-13th Century), *Appl. Phys. A* **2006**, *83*, 521-528.
4. Reibold, M.; Paufler, P.; Levin, A.A.; Kochmann, W.; Paetzke, N.; Meyer, D.C. Materials: Carbon Nanotubes in an Ancient Damascus Sabre, *Nature* **2006**, *444*, 286.
5. Feynman, R., In *Miniaturization*, Gilbert, H. D., Ed. Reinhold: New York, **1961**; pp 282-296.
6. Drexler, K.E., *Engines of Creation*. 1st ed.; Anchor Press/Doubleday: Garden City, NY, **1986**; p 298.
7. Drexler, K.E., *Unbounding the Future: The Nanotechnology Revolution*. 1st ed.; Morrow: New York, **1991**; p 304.
8. National Nanotechnology Initiative. http://www.wtec.org/loyola/nano/IWGN.Implementation.Plan/nni.implementation.plan.pdf (March, 2007).
9. Thorne, R.G.; Nicholson, C. In Vivo Diffusion Analysis with Quantum Dots and Dextrans Predicts the Width of Brain Extracellular Space, *Proc. Natl. Acad. Sci. USA* **2006**, *103*, 5567-5572.
10. Swift, J.L.; Heuff, R.; Cramb, D.T. A Two-Photon Excitation Fluorescence Cross-Correlation Assay for a Model Ligand-Receptor Binding System Using Quantum Dots, *Biophys. J.* **2006**, *90*, 1396-1410.
11. Ferrara, D.E.; Weiss, D.; Carnell, P.H.; Vito, R.P.; Vega, D.; Gao, X.; Nie, S.; Taylor, W.R. Quantitative 3D Fluorescence Technique for the Analysis of 'En Face' Preparations of Arterial Walls Using Quantum Dot Nanocrystals and Two-Photon Excitation Laser Scanning Microscopy, *Am. J. Physiol. Regul. Integr. Comp. Physiol.* **2006**, *290*, R114-R123.
12. Zhang, S.; Zhao, X. Design of Molecular Biological Materials Using Peptide Motifs, *J. Mat. Chem.* **2004**, *14*, 2082-2086.
13. Cheng, J.Y.; Mayes, A.M.; Ross, C.A. Nanostructure Engineering by Templated Self-Assembly of Block Copolymers, *Nat. Mater.* **2004**, *3*, 823-828.
14. Henzie, J.; Barton, J.E.; Stender, C.L.; Odom, T.W. Large-Area Nanoscale Patterning: Chemistry Meets Fabrication, *Acc. Chem. Res.* **2006**, *39*, 249-257.
15. Center of Nanoscale Science and Engineering, State University of New York at Albany. http://cnse.albany.edu/about_cnse/quick_facts.html (March. 2007).

16. Seeman, N.C.; Belcher, A.M. Emulating Biology: Building Nanostructures from the Bottom Up, *Proc. Natl. Acad. Sci. USA* **2002**, *99*, 6451-6455.
17. Aizenberg, J. Crystallization in Patterns: A Bio-Inspired Approach, *Adv. Mater.* **2004**, *16*, 1295-1302.
18. Mao, C.; Solis, D.J.; Reiss, B.D.; Kottmann, S.T.; Sweeney, R.Y.; Hayhurst, A.; Georgiou, G.; Iverson, B.; Belcher, A.M. Virus-Based Toolkit for the Directed Synthesis of Magnetic and Semiconducting Nanowires, *Science* **2004**, *303*, 213-217.
19. Seeman, N.C. Structural DNA Nanotechnology. An Overview, *Meth. Mol. Biol.* **2005**, *303*, 143-166.
20. Lin, C.; Liu, Y.; Rinker, S.; Yan, H. DNA Tile Based Self-Assembly: Building Complex Nanoarchitectures, *ChemPhysChem* **2006**, *7*, 1641-1647.
21. Sumper, M.; Brunner, E. Learning from Diatoms: Nature's Tools for the Production of Nanostructured Silica, *Adv. Funct. Mater.* **2006**, *16*, 17-26.
22. Mirkin, C.A.; Letsinger, R.L.; Mucic, R.C.; Storhoff, J.J. A DNA-Based Method for Rationally Assembling Nanoparticles into Macroscopic Materials, *Nature* **1996**, *382*, 607-609.
23. Lu, Y.; Yin, Y.; Li, Z.-Y.; Xia, Y. Synthesis and Self-Assembly of Au@$SiO_2$ Core-Shell Colloids, *Nano Lett.* **2002**, *2*, 785-788.
24. Penn, R.L.; Oskam, G.; Strathmann, T.J.; Searson, P.C.; Stone, A.T.; Veblen, D.R. Epitaxial Assembly in Aged Colloids, *J. Phys. Chem. B* **2001**, *105*, 2177-2182.
25. Shenhar, R.; Rotello, V.M. Nanoparticles: Scaffolds and Building Blocks, *Acc. Chem. Res.* **2003**, *36*, 549-561.
26. Yatsui, T.; Nomura, W.; Ohtsu, M. Self-Assembly of Size- and Position-Controlled Ultralong Nanodot Chains Using Near-Field Optical Desorption, *Nano Lett.* **2005**, *5*, 2548-2551.
27. Kang, Y.; Erickson, K.J.; Taton, T.A. Plasmonic Nanoparticle Chains Via a Morphological, Sphere-to-String Transition, *J. Am. Chem. Soc.* **2005**, *127*, 13800-13801.
28. Blanchet, G.B.; Subramoney, S.; Bailey, R.K.; Jaycox, G.D.; Nuckolls, C. Self-Assembled Three-Dimensional Conducting Network of Single-Wall Carbon Nanotubes, *Appl. Phys. Lett.* **2004**, *85*, 828-830.
29. Ismach, A.; Joselevich, E. Orthogonal Self-Assembly of Carbon Nanotube Crossbar Architectures by Simultaneous Graphoepitaxy and Field-Directed Growth, *Nano Lett.* **2006**, *6*, 1706-1710.
30. Wang, Y.; Maspoch, D.; Zou, S.; Schatz, G.C.; Smalley, R.E.; Mirkin, C.A. Controlling the Shape, Orientation, and Linkage of Carbon Nanotube Features with Nano Affinity Templates, *Proc. Natl. Acad. Sci, USA* **2006**, *103*, 2026-2031.
31. Huang, M.H.; Mao, S.; Feick, H.; Yan, H.; Wu, Y.; Kind, H.; Weber, E.; Russo, R.; Yang, P. Room-Temperature Ultraviolet Nanowire Nanolasers, *Science* **2001**, *292*, 1897-1899.
32. Yan, H.; He, R.; Johnson, J.; Law, M.; Saykally, R.J.; Yang, P. Dendritic Nanowire Ultraviolet Laser Array, *J. Am. Chem. Soc.* **2003**, *125*, 4728-4729.
33. Hinderling, C.; Keles, Y.; Stoeckli, T.; Knapp, H.F.; De los Arcos, T.; Oelhafen, P.; Korczagin, I.; Hempenius, M.A.; Vancso, G.J.; Pugin, R.; Heinzelmann, H.

Organometallic Block Copolymers as Catalyst Precursors for Templated Carbon Nanotube Growth, *Adv. Mater.* **2004**, *16*, 876-879.
34. Cheng, J.Y.; Jung, W.; Ross, C.A. Magnetic Nanostructures from Block Copolymer Lithography: Hysteresis, Thermal Stability, and Magnetoresistance, *Phys. Rev. B* **2004**, *70*, 064417.
35. Lee, S.-W.; Lee, S.K.; Belcher, A.M. Virus-Based Alignment of Inorganic, Organic, and Biological Nanosized Materials, *Adv. Mater.* **2003**, *15*, 689-692.
36. Koltover, I. Biomolecular Self-Assembly: Stacks of Viruses, *Nat. Mater.* **2004**, *3*, 584-586.
37. Petitjean, A.; Nierengarten, H.; van Dorosselaer, A.; Lehn, J.-M. Self-Organization of Oligomeric Helical Stacks Controlled by Substrate Binding in a Tobacco Mosaic Virus Like Self-Assembly Process, *Angew. Chem. Int. Ed. Engl.* **2004**, *43*, 3695-3699.
38. Johnson, J.M.; Tang, J.; Nyame, Y.; Willits, D.; Young, M.J.; Zlotnick, A. Regulating Self-Assembly of Spherical Oligomers, *Nano Lett.* **2005**, *5*, 765-770.
39. Huang, Y.; Chiang, C.-Y.; Lee, S.K.; Gao, Y.; Hu, E.L.; De Yoreo, J.; Belcher, A.M. Programmable Assembly of Nanoarchitectures Using Genetically Engineered Viruses, *Nano Lett.* **2005**, *5*, 1429-1434.
40. Scheibel, T.; Parthasarathy, R.; Sawicki, G.; Lin, X.M.; Jaeger, H.; Lindquist, S.L. Conducting Nanowires Built by Controlled Self-Assembly of Amyloid Fibers and Selective Metal Deposition, *Proc. Natl. Acad. Sci. USA* **2003**, *100*, 4527-4532.
41. Mayes, E.L.; Mann, S. Mineralization in Nanostructured Biocompartments: Biomimetic Ferritins for High-Density Data Storage, *Nanobiotechnol.* **2004**, 278-287.
42. Csáki, A.; Maubach, G.; Born, D.; Reichert, J.; Fritzsche, W. DNA-Based Molecular Nanotechnology, *Single Mol.* **2002**, *3*, 275-280.
43. Gothelf, K.V.; Brown, R.S. A Modular Approach to DNA-Programmed Self-Assembly of Macromolecular Nanostructures, *Chem.-Eur. J.* **2005**, *11*, 1062-1069.
44. Wang, Q.; Wang, G.; Han, X.; Wang, X.; Hou, J.G. Controllable Template Synthesis of Ni/Cu Nanocable and Ni Nanotube Arrays: A One-Step Coelectrodeposition and Electrochemical Etching Method, *J. Phys. Chem. B* **2005**, *109*, 23326-23329.
45. Li, F.; Zhu, M.; Liu, C.; Zhou, W.L.; Wiley, J.B. Patterned Metal Nanowire Arrays from Photolithographically-Modified Templates, *J. Am. Chem. Soc.* **2006**, *128*, 13342-13343.
46. Liang, J.; Chik, H.; Yin, A.; Xu, J. Two-Dimensional Lateral Superlattices of Nanostructures: Nonlithographic Formation by Anodic Membrane Template, *J. Appl. Phys.* **2002**, *91*, 2544-2546.
47. Zhang, X.; Hao, Y.; Meng, G.; Zhang, L. Fabrication of Highly Ordered InSb Nanowire Arrays by Electrodeposition in Porous Anodic Alumina Membranes, *J. Electrochem. Soc* **2005**, *152*, C664-C668.
48. Hou, S.; Wang, J.; Martin, C. R. Template-Synthesized Protein Nanotubes, *Nano Lett.* **2005**, *5*, 231-234.

49. Shiu, J.-Y.; Kuo, C.-W.; Chen, P.; Mou, C.-Y. Fabrication of Tunable Superhydrophobic Surfaces by Nanosphere Lithography, *Chem. Mater.* **2004**, *16*, 561-564.
50. Zhang, X.; Hicks, E.M.; Zhao, J.; Schatz, G.C.; Van Duyne, R.P. Electrochemical Tuning of Silver Nanoparticles Fabricated by Nanosphere Lithography, *Nano Lett.* **2005**, *5*, 1503-1507.
51. De Poortere, E.P.; Stormer, H.L.; Huang, L.M.; Wind, S.J.; O'Brien, S.; Huang, M.; Hone, J. Single-Walled Carbon Nanotubes as Shadow Masks for Nanogap Fabrication, *Appl. Phys. Lett.* **2006**, *88*, 143124.
52. Liang, H.; Angelini, T.E.; Braun, P.V.; Wong, G.C.L. Roles of Anionic and Cationic Template Components in Biomineralization of CdS Nanorods Using Self-Assembled DNA-Membrane Complexes, *J. Am. Chem. Soc.* **2004**, *126*, 14157-14165.
53. Kumar, N.; Hahm, J. Nanoscale Protein Patterning Using Self-Assembled Diblock Copolymers, *Langmuir* **2005**, *21*, 6652-6655.
54. Cresce, A.V.; Silverstein, J.S.; Bentley, W.E.; Kofinas, P. Nanopatterning of Recombinant Proteins Using Block Copolymer Templates, *Macromol.* **2006**, *39*, 5826-5829.
55. Teichert, C. Self-Organized Semiconductor Surfaces as Templates for Nanostructured Magnetic Thin Films, *Appl. Phys. A* **2003**, *76*, 653-664.
56. Kitahara, T.; Sugawara, A.; Sano, H.; Mizutani, G. Anisotropic Optical Second-Harmonic Generation from the Au Nanowire Array on the NaCl(110) Template, *Appl. Surf. Sci.* **2003**, *219*, 271-275.
57. Pinto, Y.Y.; Le, J.D.; Seeman, N.C.; Musier-Forsyth, K.; Taton, T.A.; Kiehl, R.A. Sequence-Encoded Self-Assembly of Multiple-Nanocomponent Arrays by 2D DNA Scaffolding, *Nano Lett.* **2005**, *5*, 2399-2402.
58. Blum, A.S.; Soto, C.M.; Wilson, C.D.; Whitley, J.L.; Moore, M.H.; Sapsford, K.E.; Lin, T.; Chatterji, A.; Johnson, J.E.; Ratna, B.R. Templated Self-Assembly of Quantum Dots from Aqueous Solution Using Protein Scaffolds, *Nanotechnology* **2006**, *17*, 5073-5079.
59. Lee, S.-W.; Mao, C.; Flynn, C.E.; Belcher, A.M. Ordering of Quantum Dots Using Genetically Engineered Viruses, *Science* **2002**, *296*, 892-895.
60. Flynn, C.E.; Mao, C.; Hayhurst, A.; Williams, J.L.; Georgiou, G.; Iverson, B.; Belcher, A.M. Synthesis and Organization of Nanoscale II-VI Semiconductor Materials Using Evolved Peptide Specificity and Viral Capsid Assembly, *J. Mater. Chem.* **2003**, *13*, 2414-2421.
61. Reiss, B.D.; Mao, C.; Solis, D.J.; Ryan, K.S.; Thomson, T.; Belcher, A.M. Biological Routes to Metal Alloy Ferromagnetic Nanostructures, *Nano Lett.* **2004**, *4*, 1127-1132.
62. Nam, K.T.; Kim, D.-W.; Yoo, P.J.; Chiang, C.-Y.; Meethong, N.; Hammond, P.T.; Chiang, Y.-M.; Belcher, A.M. Virus-Enabled Synthesis and Assembly of Nanowires for Lithium Ion Battery Electrodes, *Science* **2006**, *312*, 885-888.
63. Sinensky, A.K.; Belcher, A.M. Biomolecular Recognition of Crystal Defects: A Diffuse-Selection Approach, *Adv. Mater.* **2006**, *18*, 991-996.

64. Sanghvi, A.B.; Miller, K.P.H.; Belcher, A.M.; Schmidt, C.E. Biomaterials Functionalization Using a Novel Peptide That Selectively Binds to a Conducting Polymer, *Nat. Mater.* **2005**, *4*, 496-502.
65. Yoo, P.J.; Nam, K.T.; Qi, J.; Lee, S.-K.; Park, J.; Belcher, A.M.; Hammond, P.T. Spontaneous Assembly of Viruses on Multilayered Polymer Surfaces, *Nat. Mater.* **2006**, *5*, 234-240.
66. Steinmetz, N.F.; Calder, G.; Lomonossoff, G.P.; Evans, D.J. Plant Viral Capsids as Nanobuilding Blocks: Construction of Arrays on Solid Supports, *Langmuir* **2006**, *22*, 10032-10037.
67. Lin, T. Structural Genesis of the Chemical Addressability in a Viral Nano-Block, *J. Mater. Chem.* **2006**, *16*, 3673-3681.
68. Addadi, L.; Joester, D.; Nudelman, F.; Weiner, S. Mollusk Shell Formation: A Source of New Concepts for Understanding Biomineralization Processes, *Chem.-Eur. J.* **2006**, *12*, 980-987.
69. Hartgerink, J.D.; Granja, J.R.; Milligan, R.A.; Ghadiri, M.R. Self-Assembling Peptide Nanotubes, *J. Am. Chem. Soc.* **1996**, *118*, 43-50.
70. Makabe, K.; McElheny, D.; Tereshko, V.; Hilyard, A.; Gawlak, G.; Yan, S.; Koide, A.; Koide, S. Atomic Structures of Peptide Self-Assembly Mimics, *Proc. Natl. Acad. Sci. USA* **2006**, *103*, 17753-17758.
71. Gartner, Z.J.; Liu, D.R. The Generality of DNA-Templated Synthesis as a Basis for Evolving Non-Natural Small Molecules, *J. Am. Chem. Soc.* **2001**, *123*, 6961-6963.
72. Gartner, Z.J.; Tse, B.N.; Grubina, R.; Doyon, J.B.; Snyder, T.M.; Liu, D.R. DNA-Templated Organic Synthesis and Selection of a Library of Macrocycles, *Science* **2004**, *305*, 1601-1605.
73. Seeman, N.C. At the Crossroads of Chemistry, Biology, and Materials: Structural DNA Nanotechnology, *Chem. Biol.* **2003**, *10*, 1151-1159.
74. Seeman, N.C. DNA in a Material World, *Nature* **2003**, *421*, 427-431.
75. Turberfield, A. DNA as an Engineering Material, *Phys. World* **2003**, *16*, 43-46.
76. Nelson, D.L.; Cox, M.M., Protein Metabolism. In *Lehninger Principles of Biochemistry*, Freeman and Co.: New York, **2005**; pp 1034-1048.
77. Klug, W.S.; Cummings, M.R., Nucleic Acid Chemistry. In *Concepts of Genetics*, Prentice Hall: Upper Saddle River, NJ, **1997**; pp 273-283.
78. Sambrook, J.; Fritsch, E.F.; Maniatis, T., DNA Polymerases. In *Molecular Cloning: A Laboratory Manual*, 2nd ed.; Cold Spring Harbor Laboratory Press: Cold Spring Harbor, NY, **1989**; Vol. *1*, pp 5.34-5.59.
79. Watson, J.D.; Crick, F.H.C. Molecular Structure of Nucleic Acids. A Structure for Deoxyribose Nucleic Acid, *Nature* **1953**, *171*, 737-738.
80. Crick, F.H. On the Genetic Code, *Science* **1963**, *139*, 461-464.
81. Watson, J.D. Involvement of Ribonucleic Acid in the Synthesis of Proteins, *Science* **1963**, *140*, 17-26.
82. Dickerson, R.E.; Drew, H.R.; Conner, B.N.; Wing, R.M.; Fratini, A.V.; Kopka, M.L. The Anatomy of A-, B-, and Z-DNA, *Science* **1982**, *216*, 475-485.
83. Dickerson, R.E.; Conner, B.N.; Kopka, M.L.; Drew, H.R. The Geometry of A, B, and Z DNA, *Nucl. Acids Res.* **1983**, 35-59.

84. Escude, C.; Sun, J.-S., DNA Major Groove Binders: Triple Helix-Forming Oligonucleotides, Triple Helix-Specific DNA Ligands and Cleaving Agents. In *Topics in Current Chemistry*, Springer: Berlin/Heidelberg, Germany, **2005**; Vol. *253*, pp 109-148.
85. Panyutin, I.G.; Kovalsky, O.I.; Budovsky, E.I.; Dickerson, R.E.; Rikhirev, M.E.; Lipanov, A.A. G-DNA: A Twice-Folded DNA Structure Adopted by Single-Stranded Oligo(dG) and Its Implications for Telomeres, *Proc. Natl. Acad. Sci, USA* **1990**, *87*, 867-870.
86. Breslauer, K.J.; Frank, R.; Blocker, H.; Marky, L.A. Predicting DNA Duplex Stability from the Base Sequence, *Proc. Natl. Acad. Sci. USA* **1986**, *83*, 3746-3750.
87. Krautbauer, R.; Rief, M.; Gaub, H.E. Unzipping DNA Oligomers, *Nano Lett.* **2003**, *3*, 493-496.
88. Sambrook, J.; Fritsch, E.F.; Maniatis, T., Conditions for Hybridization of Oligonucleotide Probes. In *Molecular Cloning: A Laboratory Manual*, 2nd ed.; Cold Spring Harbor Laboratory Press: Cold Spring Harbor, NY, **1989**; Vol. *2*, pp 11.45-11.57.
89. Blake, R.D.; Bizzaro, J.W.; Blake, J.D.; Day, G.R.; Delcourt, S.G.; Knowles, J.; Marx, K.A.; SantaLucia, J., Jr. Statistical Mechanical Simulation of Polymeric DNA Melting with Meltsim, *Bioinformatics* **1999**, *15*, 370-375.
90. Zuker, M. Mfold Web Server for Nucleic Acid Folding and Hybridization Prediction, *Nucl. Acids Res.* **2003**, *31*, 3406-3415.
91. Wiese, K.C.; Hendriks, A. Comparison of P-RNAPredict and Mfold-Algorithms for RNA Secondary Structure Prediction, *Bioinformatics* **2006**, *22*, 934-942.
92. SantaLucia, J., Jr. A Unified View of Polymer, Dumbbell, and Oligonucleotide DNA Nearest-Neighbor Thermodynamics, *Proc. Natl. Acad. Sci. USA* **1998**, *95*, 1460-1465.
93. Bommarito, S.; Peyret, N.; SantaLucia, J., Jr. Thermodynamic Parameters for DNA Sequences with Dangling Ends, *Nucl. Acids Res.* **2000**, *28*, 1929-1934.
94. SantaLucia, J., Jr.; Hicks, D. The Thermodynamics of DNA Structural Motifs, *Annu. Rev. Biophys. Biomol. Struct.* **2004**, *33*, 415-440.
95. Sambrook, J.; Fritsch, E.F.; Maniatis, T., In Vitro Amplification of DNA by the Polymerase Chain Reaction. In *Molecular Cloning: A Laboratory Manual*, 2nd ed.; Cold Spring Harbor Laboratory Press: Cold Spring Harbor, NY, **1989**; Vol. *2*, pp 14.1-14.17.
96. Sambrook, J.; Fritsch, E.F.; Maniatis, T., *Molecular Cloning: A Laboratory Manual*. 2nd ed.; Cold Spring Harbor Laboratory Press: Cold Spring Harbor, NY **1989**; Vol. *1-3*.
97. Zhang, Y.W.; Seeman, N.C. A Solid-Support Methodology for the Construction of Geometrical Objects from DNA, *J. Am. Chem. Soc.* **1992**, *114*, 2656-2663.
98. O'Neill, P.; Rothemund, P.W.K.; Kumar, A.; Fygenson, D.K. Sturdier DNA Nanotubes Via Ligation, *Nano Lett.* **2006**, *6*, 1379-1383.
99. Sambrook, J.; Fritsch, E.F.; Maniatis, T., Bacteriophage Vectors. In *Molecular Cloning: A Laboratory Manual*, 2nd ed.; Cold Spring Harbor Laboratory Press: Cold Spring Harbor, NY, **1989**; Vol. *1*, pp 2.2-2.18.
100. Narang, S.A. DNA Synthesis, *Tetrahedron* **1983**, *39*, 3-22.

101. Itakura, K.; Rossi, J.J.; Wallace, R.B. Synthesis and Use of Synthetic Oligonucleotides, *Ann. Rev. Biochem.* **1984**, *53*, 323-356.
102. Caruthers, M.H. Gene Synthesis Machines: DNA Chemistry and Its Uses, *Science* **1985**, *230*, 281-285.
103. Manning, G.S. Limiting Laws and Counterion Condensation in Polyelectroyte Solutions. I. Colligative Properties, *J. Chem. Phys.* **1969**, *51*, 924-933.
104. Manning, G.S. Application of Polyelectrolyte "Limiting Laws" To the Helix-Coil Transition of DNA. I. Excess Univalent Cations, *Biopolymers* **1972**, *11*, 937-949.
105. Manning, G.S. Application of Polyelectrolyte "Limiting Laws" To the Helix-Coil Transition of DNA. II. Effect of $Mg^{2+}$ Counterions, *Biopolymers* **1972**, *11*, 951-955.
106. Petty, J.T.; Zheng, J.; Hud, N.V.; Dickson, R.M. DNA-Templated Ag Nanocluster Formation, *J. Am. Chem. Soc.* **2004**, *126*, 5207-5212.
107. Wang, J.; Rincon, O.; Polsky, R.; Dominguez, E. Electrochemical Detection of DNA Hybridization Based on DNA-Templated Assembly of Silver Cluster, *Electrochem. Commun.* **2003**, *5*, 83-86.
108. Duguid, J.; Bloomfield, V.A.; Benevides, J.; Thomas, G.J., Jr. Raman Spectroscopy of DNA-Metal Complexes. I. Interactions and Conformational Effects of the Divalent Cations: Mg, Ca, Sr, Ba, Mn, Co, Ni, Cu, Pd, and Cd, *Biophys. J.* **1993**, *65*, 1916-1928.
109. Moreno-Herrero, F.; Herrero, P.; Moreno, F.; Colchero, J.; Gomez-Navarro, C.; Gomez-Herrero, J.; Baro, A.M. Topographic Characterization and Electrostatic Response of M-DNA Studied by Atomic Force Microscopy, *Nanotechnology* **2003**, *14*, 128-133.
110. Seidel, R.; Ciacchi, L.C.; Weigel, M.; Pompe, W.; Mertig, M. Synthesis of Platinum Cluster Chains on DNA Templates: Conditions for a Template-Controlled Cluster Growth, *J. Phys. Chem. B* **2004**, *108*, 10801-10811.
111. Lysetska, M.; Knoll, A.; Boehringer, D.; Hey, T.; Krauss, G.; Krausch, G. UV Light-Damaged DNA and Its Interaction with Human Replication Protein A: An Atomic Force Microscopy Study, *Nucl. Acids Res.* **2002**, *30*, 2686-2691.
112. Karanjawala, Z.E.; Lieber, M.R. DNA Damage and Aging, *Mech. Ageing Develop.* **2004**, *125*, 405-415.
113. Nakabeppu, Y.; Tsuchimoto, D.; Furuichi, M.; Sakumi, K. The Defense Mechanisms in Mammalian Cells against Oxidative Damage in Nucleic Acids and Their Involvement in the Suppression of Mutagenesis and Cell Death, *Free Radical Res.* **2004**, *38*, 423-429.
114. Becerril, H.A.; Stoltenberg, R.M.; Monson, C.F.; Woolley, A.T. Ionic Surface Masking for Low Background in Single- and Double-Stranded DNA-Templated Silver and Copper Nanorods, *J. Mater. Chem.* **2004**, *14*, 611-616.
115. Seeman, N.C. Nucleic Acid Junctions and Lattices, *J. Theor. Biol.* **1982**, *99*, 237-47.
116. Kallenbach, N.R.; Ma, R.I.; Seeman, N.C. An Immobile Nucleic Acid Junction Constructed from Oligonucleotides, *Nature* **1983**, *305*, 829-831.
117. Chen, J.H.; Seeman, N.C. Synthesis from DNA of a Molecule with the Connectivity of a Cube, *Nature* **1991**, *350*, 631-633.

118. Mao, C.; Sun, W.; Seeman, N.C. Assembly of Borromean Rings from DNA, *Nature* **1997**, *386*, 137-138.
119. Seeman, N.C.; Wang, H.; Yang, X.P.; Liu, F.R.; Mao, C.D.; Sun, W.Q.; Wenzler, L.; Shen, Z.Y.; Sha, R.J.; Yan, H.; Wong, M.H.; Sa-Ardyen, P.; Liu, B.; Qiu, H.X.; Li, X.J.; Qi, J.; Du, S.M.; Zhang, Y.W.; Mueller, J.E.; Fu, T.J.; Wang, Y.L.; Chen, J.H. New Motifs in DNA Nanotechnology, *Nanotechnology* **1998**, *9*, 257-273.
120. Winfree, E.; Liu, F.R.; Wenzler, L.A.; Seeman, N.C. Design and Self-Assembly of Two-Dimensional DNA Crystals, *Nature* **1998**, *394*, 539-544.
121. Shen, Z.; Yan, H.; Wang, T.; Seeman, N.C. Paranemic Crossover DNA: A Generalized Holliday Structure with Applications in Nanotechnology, *J. Am. Chem. Soc.* **2004**, *126*, 1666-1674.
122. LaBean, T.H.; Yan, H.; Kopatsch, J.; Liu, F.; Winfree, E.; Reif, J.H.; Seeman, N.C. Construction, Analysis, Ligation, and Self-Assembly of DNA Triple Crossover Complexes, *J. Am. Chem. Soc.* **2000**, *122*, 1848-1860.
123. Liu, D.; Wang, M.; Deng, Z.; Walulu, R.; Mao, C. Tensegrity: Construction of Rigid DNA Triangles with Flexible Four-Arm DNA Junctions, *J. Am. Chem. Soc.* **2004**, *126*, 2324-2325.
124. Park, S.H.; Barish, R.; Li, H.; Reif, J.H.; Finkelstein, G.; Yan, H.; LaBean, T.H. Three-Helix Bundle DNA Tiles Self-Assemble into 2D Lattice or 1D Templates for Silver Nanowires, *Nano Lett.* **2005**, *5*, 693-696.
125. He, Y.; Tian, Y.; Ribbe, A.E.; Mao, C. Highly Connected Two-Dimensional Crystals of DNA Six-Point-Stars, *J. Am. Chem. Soc.* **2006**, *128*, 15978-15979.
126. Yan, H.; LaBean, T.H.; Feng, L.; Reif, J.H. Directed Nucleation Assembly of DNA Tile Complexes for Barcode-Patterned Lattices, *Proc. Natl. Acad. Sci, USA* **2003**, *100*, 8103-8108.
127. Sha, R.J.; Liu, F.R.; Millar, D.P.; Seeman, N.C. Atomic Force Microscopy of Parallel DNA Branched Junction Arrays, *Chem. Biol.* **2000**, *7*, 743-751.
128. Mao, C.D.; Sun, W.Q.; Seeman, N.C. Designed Two-Dimensional DNA Holliday Junction Arrays Visualized by Atomic Force Microscopy, *J. Am. Chem. Soc.* **1999**, *121*, 5437-5443.
129. Feng, L.; Park, S.H.; Reif, J.H.; Yan, H. A Two-State DNA Lattice Switched by DNA Nanoactuator, *Angew. Chem. Int. Ed. Engl.* **2003**, *42*, 4342-4346.
130. Chelyapov, N.; Brun, Y.; Gopalkrishnan, M.; Reishus, D.; Shaw, B.; Adleman, L. DNA Triangles and Self-Assembled Hexagonal Tilings, *J. Am. Chem. Soc.* **2004**, *126*, 13924-13925.
131. Lund, K.; Liu, Y.; Lindsay, S.; Yan, H. Self-Assembling a Molecular Pegboard, *J. Am. Chem. Soc.* **2005**, *127*, 17606-17607.
132. He, Y.; Tian, Y.; Chen, Y.; Deng, Z.; Ribbe, A.E.; Mao, C. Sequence Symmetry as a Tool for Designing DNA Nanostructures, *Angew. Chem. Int. Ed. Engl.* **2005**, *44*, 6694-6696.
133. He, Y.; Chen, Y.; Liu, H.; Ribbe, A.E.; Mao, C. Self-Assembly of Hexagonal DNA Two-Dimensional (2D) Arrays, *J. Am. Chem. Soc.* **2005**, *127*, 12202-12203.
134. Reishus, D.; Shaw, B.; Brun, Y.; Chelyapov, N.; Adleman, L. Self-Assembly of DNA Double-Double Crossover Complexes into High-Density, Doubly Connected, Planar Structures, *J. Am. Chem. Soc.* **2005**, *127*, 17590-17591.

135. Park, S.H.; Pistol, C.; Ahn, S.J.; Reif, J.H.; Lebeck, A.R.; Dwyer, C.; LaBean, T.H. Finite-Size, Fully Addressable DNA Tile Lattices Formed by Hierarchical Assembly Procedures, *Angew. Chem. Int. Ed. Engl.* **2006**, *45*, 735-739.
136. Park, S.H.; Yan, H.; Reif, J.H.; LaBean, T.H.; Finkelstein, G. Electronic Nanostructures Templated on Self-Assembled DNA Scaffolds, *Nanotechnology* **2004**, *15*, S525-S527.
137. Li, H.; Park, S.H.; Reif, J.H.; LaBean, T.H.; Yan, H. DNA-Templated Self-Assembly of Protein and Nanoparticle Linear Arrays, *J. Am. Chem. Soc.* **2004**, *126*, 418-419.
138. Zhang, J.; Liu, Y.; Ke, Y.; Yan, H. Periodic Square-Like Gold Nanoparticle Arrays Templated by Self-Assembled 2D DNA Nanogrids on a Surface, *Nano Lett.* **2006**, *6*, 248-251.
139. Sharma, J.; Chhabra, R.; Liu, Y.; Ke, Y.; Yan, H. DNA-Templated Self-Assembly of Two-Dimensional and Periodical Gold Nanoparticle Arrays, *Angew. Chem. Int. Ed. Engl.* **2006**, *45*, 730-735.
140. Yan, H.; Park, S.H.; Finkelstein, G.; Reif, J.H.; LaBean, T.H. DNA-Templated Self-Assembly of Protein Arrays and Highly Conductive Nanowires, *Science* **2003**, *301*, 1882-1884.
141. Park, S.H.; Yin, P.; Liu, Y.; Reif, J.H.; LaBean, T.H.; Yan, H. Programmable DNA Self-Assemblies for Nanoscale Organization of Ligands and Proteins, *Nano Lett.* **2005**, *5*, 729-733.
142. He, Y.; Tian, Y.; Ribbe, A.E.; Mao, C. Antibody Nanoarrays with a Pitch of ~20 Nanometers, *J. Am. Chem. Soc.* **2006**, *128*, 12664-12665.
143. Lin, C.; Liu, Y.; Yan, H. Self-Assembled Combinatorial Encoding Nanoarrays for Multiplexed Biosensing, *Nano Lett.* **2007**, *7*, 507-512.
144. Adleman, L.M. Computing with DNA, *Sci. Am.* **1998**, *279*, 54-61.
145. Mao, C.D.; LaBean, T.H.; Reif, J.H.; Seeman, N.C. Logical Computation Using Algorithmic Self-Assembly of DNA Triple-Crossover Molecules, *Nature* **2000**, *407*, 493-496.
146. Braich, R.S.; Chelyapov, N.; Johnson, C.; Rothemund, P.W.K.; Adleman, L. Solution of a 20-Variable 3-Sat Problem on a DNA Computer, *Science* **2002**, *296*, 499-502.
147. Carbone, A.; Seeman, N.C. Circuits and Programmable Self-Assembling DNA Structures, *Proc. Natl. Acad. Sci. USA* **2002**, *99*, 12577-12582.
148. Reif, J.H. Computing: Success and Challenges, *Science* **2002**, *296*, 478-479.
149. Yan, H.; Feng, L.; LaBean, T.H.; Reif, J.H. Parallel Molecular Computations of Pairwise Exclusive-or (XOR) Using DNA "String Tile" Self-Assembly, *J. Am. Chem. Soc.* **2003**, *125*, 14246-14247.
150. Rothemund, P.W.K.; Papadakis, N.; Winfree, E. Algorithmic Self-Assembly of DNA Sierpinski Triangles, *PLoS Biol.* **2004**, *2*, 2041-2053.
151. Barish, R.D.; Rothemund, P.W.K.; Winfree, E. Two Computational Primitives for Algorithmic Self-Assembly: Copying and Counting, *Nano Lett.* **2005**, *5*, 2586-2592.
152. Rothemund, P.W.K. Folding DNA to Create Nanoscale Shapes and Patterns, *Nature* **2006**, *440*, 297-302.

153. Liu, W.; Wang, S.; Gao, L.; Zhang, F.; Xu, J. DNA Sequence Design Based on Template Strategy, *J. Chem. Inf. Comput. Sci.* **2003**, *43*, 2014-2018.
154. Seeman, N.C.; Kallenbach, N.R. Design of Immobile Nucleic Acid Junctions, *Biophys. J.* **1983**, *44*, 201-209.
155. Seeman, N.C. Denovo Design of Sequences for Nucleic-Acid Structural-Engineering, *J. Biomol. Struct. Dyn.* **1990**, *8*, 573-581.
156. LaBean, T.H.; Yan, H.; Kopatsch, J.; Liu, F.R.; Winfree, E.; Reif, J.H.; Seeman, N.C. Construction, Analysis, Ligation, and Self-Assembly of DNA Triple Crossover Complexes, *J. Am. Chem. Soc.* **2000**, *122*, 1848-1860.
157. Goodman, R.P. NANEV: A Program Employing Evolutionary Methods for the Design of Nucleic Acid Nanostructures, *BioTechniques* **2005**, *38*, 548-550.
158. Birac, J.J.; Sherman, W.B.; Kopatsch, J.; Constantinou, P.E.; Seeman, N.C. Architecture with Gideon, a Program for Design in Structural DNA Nanotechnology, *J. Mol. Graph. Model.* **2006**, *25*, 470-480.
159. Sherman, W.B.; Seeman, N.C. Design of Minimally Strained Nucleic Acid Nanotubes, *Biophys. J.* **2006**, *90*, 4546-4557.
160. Storhoff, J.J.; Elghanian, R.; Mucic, R.C.; Mirkin, C.A.; Letsinger, R.L. One-Pot Colorimetric Differentiation of Polynucleotides with Single Base Imperfections Using Gold Nanoparticle Probes, *J. Am. Chem. Soc.* **1998**, *120*, 1959-1964.
161. Thaxton, C.S.; Mirkin, C.A. DNA-Gold-Nanoparticle Conjugates. In *Nanobiotechnology*, Niemeyer, C.M.; Mirkin, C.A., Eds. Wiley-VCH: Weinheim, Germany, **2004**, pp 288-307.
162. Reynolds, R.A.; Mirkin, C.A.; Letsinger, R.L. A Gold Nanoparticle/Latex Microsphere-Based Colorimetric Oligonucleotide Detection Method, *Pure Appl. Chem.* **2000**, *72*, 229-235.
163. Taton, T.A.; Mirkin, C.A.; Letsinger, R.L. Scanometric DNA Array Detection with Nanoparticle Probes, *Science* **2000**, *289*, 1757-1760.
164. Cao, Y.C.; Jin, R.; Thaxton, C.S.; Mirkin, C.A. A Two-Color-Change, Nanoparticle-Based Method for DNA Detection, *Talanta* **2005**, *67*, 449-455.
165. Han, M.S.; Lytton-Jean, A.K.R.; Mirkin, C.A. A Gold Nanoparticle Based Approach for Screening Triplex DNA Binders, *J. Am. Chem. Soc.* **2006**, *128*, 4954-4955.
166. Nam, J.-M.; Park, S.-J.; Mirkin, C.A. Bio-Barcodes Based on Oligonucleotide-Modified Nanoparticles, *J. Am. Chem. Soc.* **2002**, *124*, 3820-3821.
167. Han, M.S.; Lytton-Jean, A.K.R.; Oh, B.-K.; Heo, J.; Mirkin, C.A. Colorimetric Screening of DNA-Binding Molecules with Gold Nanoparticle Probes, *Angew. Chem. Int. Ed. Engl.* **2006**, *45*, 1807-1810.
168. Storhoff, J.J.; Lazarides, A.A.; Mucic, R.C.; Mirkin, C.A.; Letsinger, R.L.; Schatz, G.C. What Controls the Optical Properties of DNA-Linked Gold Nanoparticle Assemblies?, *J. Am. Chem. Soc.* **2000**, *122*, 4640-4650.
169. Park, S.J.; Lazarides, A.A.; Mirkin, C.A.; Brazis, P.W.; Kannewurf, C.R.; Letsinger, R.L. The Electrical Properties of Gold Nanoparticle Assemblies Linked by DNA, *Angew. Chem. Int. Ed. Engl.* **2000**, *39*, 3845-3848.
170. Park, S.J.; Taton, T.A.; Mirkin, C.A. Array-Based Electrical Detection of DNA with Nanoparticle Probes, *Science* **2002**, *295*, 1503-1506.

171. Li, Z.; Jin, R.C.; Mirkin, C.A.; Letsinger, R.L. Multiple Thiol-Anchor Capped DNA-Gold Nanoparticle Conjugates, *Nucl. Acids Res.* **2002**, *30*, 1558-1562.
172. Demers, L.M.; Oestblom, M.; Zhang, H.; Jang, N.-H.; Liedberg, B.; Mirkin, C.A. Thermal Desorption Behavior and Binding Properties of DNA Bases and Nucleosides on Gold, *J. Am. Chem. Soc.* **2002**, *124*, 11248-11249.
173. Storhofff, J.J.; Elghanian, R.; Mirkin, C.A.; Letsinger, R.L. Sequence-Dependent Stability of DNA-Modified Gold Nanoparticles, *Langmuir* **2002**, *18*, 6666-6670.
174. Jin, R.C.; Wu, G.S.; Li, Z.; Mirkin, C.A.; Schatz, G.C. What Controls the Melting Properties of DNA-Linked Gold Nanoparticle Assemblies?, *J. Am. Chem. Soc.* **2003**, *125*, 1643-1654.
175. Park, S.-J.; Lazarides, A.A.; Storhoff, J.J.; Pesce, L.; Mirkin, C.A. The Structural Characterization of Oligonucleotide-Modified Gold Nanoparticle Networks Formed by DNA Hybridization, *J. Phys. Chem. B* **2004**, *108*, 12375-12380.
176. Reichert, J.; Csáki, A.; Köhler, J.M.; Fritzsche, W. Chip-Based Optical Detection of DNA Hybridization by Means of Nanobead Labeling, *Anal. Chem.* **2000**, *72*, 6025-6029.
177. Fritzsche, W. DNA-Gold Conjugates for the Detection of Specific Molecular Interactions, *Rev. Mol. Biotechnol.* **2001**, *82*, 37-46.
178. Csáki, A.; Kaplanek, P.; Möeller, R.; Fritzsche, W. The Optical Detection of Individual DNA-Conjugated Gold Nanoparticles Labels after Metal Enhancement, *Nanotechnology* **2003**, *14*, 1262-1268.
179. Möeller, R.; Csáki, A.; Köehler, J.M.; Fritzsche, W. Electrical Classification of the Concentration of Bioconjugated Metal Colloids after Surface Adsorption and Silver Enhancement, *Langmuir* **2001**, *17*, 5426-5430.
180. Möeller, R.; Powell, R.D.; Hainfeld, J.F.; Fritzsche, W. Enzymatic Control of Metal Deposition as Key Step for a Low-Background Electrical Detection for DNA Chips, *Nano Lett.* **2005**, *5*, 1475-1482.
181. Willner, I.; Patolsky, F.; Wasserman, J. Photoelectrochemistry with Controlled DNA-Cross-Linked CdS Nanoparticle Arrays, *Angew. Chem. Int. Ed. Engl.* **2001**, *40*, 1861-1864.
182. Gerion, D.; Parak, W.J.; Williams, S.C.; Zanchet, D.; Micheel, C.M.; Alivisatos, A.P. Sorting Fluorescent Nanocrystals with DNA, *J. Am. Chem. Soc.* **2002**, *124*, 7070-7074.
183. Gerion, D.; Chen, F.; Kannan, B.; Fu, A.; Parak, W.J.; Chen, D.J.; Majumdar, A.; Alivisatos, A.P. Room-Temperature Single-Nucleotide Polymorphism and Multiallele DNA Detection Using Fluorescent Nanocrystals and Microarrays, *Anal. Chem.* **2003**, *75*, 4766-4772.
184. Alivisatos, A.P.; Johnsson, K.P.; Peng, X.; Wilson, T.E.; Loweth, C.J.; Bruchez, M.P., Jr.; Schultz, P.G. Organization of 'Nanocrystal Molecules' Using DNA, *Nature* **1996**, *382*, 609-611.
185. Loweth, C.J.; Caldwell, W.B.; Peng, X.; Alivisatos, A.P.; Schultz, P.G. DNA-Based Assembly of Gold Nanocrystals, *Angew. Chem. Int. Ed. Engl.* **1999**, *38*, 1808-1812.
186. Zanchet, D.; Micheel, C.M.; Parak, W.J.; Gerion, D.; Williams, S.C.; Alivisatos, A.P. Electrophoretic and Structural Studies of DNA-Directed Au Nanoparticle Groupings, *J. Phys. Chem. B* **2002**, *106*, 11758-11763.

187. Zanchet, D.; Micheel, C.M.; Parak, W.J.; Gerion, D.; Alivisatos, A.P. Electrophoretic Isolation of Discrete Au Nanocrystal/DNA Conjugates, *Nano Lett.* **2001**, *1*, 32-35.
188. Mucic, R.C.; Storhoff, J.J.; Mirkin, C.A.; Letsinger, R.L. DNA-Directed Synthesis of Binary Nanoparticle Network Materials, *J. Am. Chem. Soc.* **1998**, *120*, 12674-12675.
189. Rosi, N.L.; Thaxton, C.S.; Mirkin, C.A. Control of Nanoparticle Assembly by DNA-Modified Diatom Templates, *Angew. Chem. Int. Ed. Engl.* **2004**, *43*, 5500-5503.
190. Park, S.Y.; Lee, J.-S.; Georganopoulou, D.; Mirkin, C.A.; Schatz, G.C. Structures of DNA-Linked Nanoparticle Aggregates, *J. Phys. Chem. B* **2006**, *110*, 12673-12681.
191. Maye, M.M.; Nykypanchuk, D.; van der Lelie, D.; Gang, O. A Simple Method for Kinetic Control of DNA-Induced Nanoparticle Assembly, *J. Am. Chem. Soc.* **2006**, *128*, 14020-14021.
192. Zheng, J.; Constantinou, P.E.; Micheel, C.; Alivisatos, A.P.; Kiehl, R.A.; Seeman, N.C. Two-Dimensional Nanoparticle Arrays Show the Organizational Power of Robust DNA Motifs, *Nano Lett.* **2006**, *6*, 1502-1504.
193. Coffer, J.L.; Bigham, S.R.; Li, X.; Pinizzotto, R.F.; Rho, Y.G.; Pirtle, R.M.; Pirtle, I.L. Dictation of the Shape of Mesoscale Semiconductor Nanoparticle Assemblies by Plasmid DNA, *Appl. Phys. Lett.* **1996**, *69*, 3851-3853.
194. Braun, E.; Eichen, Y.; Sivan, U.; Ben-Yoseph, G. DNA-Templated Assembly and Electrode Attachment of a Conducting Silver Wire, *Nature* **1998**, *391*, 775-778.
195. Eichen, Y.; Braun, E.; Sivan, U.; Ben-Yoseph, G. Self-Assembly of Nanoelectronic Components and Circuits Using Biological Templates, *Acta Polym.* **1998**, *49*, 663-670.
196. Richter, J.; Mertig, M.; Pompe, W.; Monch, I.; Schackert, H.K. Construction of Highly Conductive Nanowires on a DNA Template, *Appl. Phys. Lett.* **2001**, *78*, 536-538.
197. Richter, J.; Mertig, M.; Pompe, W.; Vinzelberg, H. Low-Temperature Resistance of DNA-Templated Nanowires, *Appl. Phys. A* **2002**, *74*, 725-728.
198. Lund, J.; Dong, J.; Deng, Z.; Mao, C.; Parviz, B.A. Electrical Conduction in 7 nm Wires Constructed on λ-DNA, *Nanotechnology* **2006**, *17*, 2752-2757.
199. Park, S.H.; Prior, M.W.; LaBean, T.H.; Finkelstein, G. Optimized Fabrication and Electrical Analysis of Silver Nanowires Templated on DNA Molecules, *Appl. Phys. Lett.* **2006**, *89*, 033901.
200. Harnack, O.; Ford, W.E.; Yasuda, A.; Wessels, J.M. Tris(Hydroxymethyl)Phosphine-Capped Gold Particles Templated by DNA as Nanowire Precursors, *Nano Lett.* **2002**, *2*, 919-923.
201. Keren, K.; Krueger, M.; Gilad, R.; Ben-Yoseph, G.; Sivan, U.; Braun, E. Sequence-Specific Molecular Lithography on Single DNA Molecules, *Science* **2002**, *297*, 72-75.
202. Ongaro, A.; Griffin, F.; Beecher, P.; Nagle, L.; Iacopino, D.; Quinn, A.; Redmond, G.; Fitzmaurice, D. DNA-Templated Assembly of Conducting Gold Nanowires between Gold Electrodes on a Silicon Oxide Substrate, *Chem. Mater.* **2005**, *17*, 1959-1964.

203. Liu, D.; Park, S.H.; Reif, J.H.; LaBean, T.H. DNA Nanotubes Self-Assembled from Triple-Crossover Tiles as Templates for Conductive Nanowires, *Proc. Natl. Acad. Sci. USA* **2004**, *101*, 717-722.
204. Deng, Z.X.; Mao, C.D. DNA-Templated Fabrication of 1D Parallel and 2D Crossed Metallic Nanowire Arrays, *Nano Lett.* **2003**, *3*, 1545-1548.
205. Ford, W.E.; Harnack, O.; Yasuda, A.; Wessels, J.M. Platinated DNA as Precursors to Templated Chains of Metal Nanoparticles, *Adv. Mater.* **2001**, *13*, 1793-1797.
206. Mertig, M.; Ciacchi, L.C.; Seidel, R.; Pompe, W.; De Vita, A. DNA as a Selective Metallization Template, *Nano Lett.* **2002**, *2*, 841-844.
207. Weizmann, Y.; Patolsky, F.; Popov, I.; Willner, I. Telomerase-Generated Templates for the Growing of Metal Nanowires, *Nano Lett.* **2004**, *4*, 787-792.
208. Monson, C.F.; Woolley, A.T. DNA-Templated Construction of Copper Nanowires, *Nano Lett.* **2003**, *3*, 359-363.
209. Kudo, H.; Fujihira, M. DNA-Templated Copper Nanowire Fabrication by a Two-Step Process Involving Electroless Metallization, *IEEE Trans. Nanotechnol.* **2006**, *5*, 90-92.
210. Berti, L.; Alessandrini, A.; Menozzi, C.; Facci, P. Controlled DNA-Templated Metal Deposition: Towards Ultra-Thin Nanowires, *J. Nanosci. Nanotechnol.* **2006**, *6*, 2382-2385.
211. Gu, Q.; Cheng, C.; Suryanarayanan, S.; Dai, K.; Haynie, D.T. DNA-Templated Fabrication of Nickel Nanocluster Chains, *Physica E* **2006**, *33*, 92-98.
212. Becerril, H.A.; Ludtke, P.; Willardson, B.M.; Woolley, A.T. DNA-Templated Nickel Nanostructures and Protein Assemblies, *Langmuir* **2006**, *22*, 10140-10144.
213. Gu, Q.; Cheng, C.D.; Haynie, D.T. Cobalt Metallization of DNA: Toward Magnetic Nanowires, *Nanotechnology* **2005**, *16*, 1358-1363.
214. Dittmer, W.U.; Simmel, F.C. Chains of Semiconductor Nanoparticles Templated on DNA, *Appl. Phys. Lett.* **2004**, *85*, 633-635.
215. Nyamjav, D.; Ivanisevic, A. Templates for DNA-Templated $Fe_3O_4$ Nanoparticles, *Biomaterials* **2005**, *26*, 2749-2757.
216. Richter, J. Metallization of DNA, *Physica E* **2003**, *16*, 157-173.
217. Becerril, H.A.; Stoltenberg, R.M.; Wheeler, D.R.; Davis, R.C.; Harb, J.N.; Woolley, A.T. DNA-Templated Three-Branched Nanostructures for Nanoelectronic Devices, *J. Am. Chem. Soc.* **2005**, *127*, 2828-2829.
218. Stanca, S.E.; Ongaro, A.; Eritja, R.; Fitzmaurice, D. DNA-Templated Assembly of Nanoscale Architectures, *Nanotechnology* **2005**, *16*, 1905-1911.
219. Tian, Y.; He, Y.; Ribbe, A.E.; Mao, C. Preparation of Branched Structures with Long DNA Duplex Arms, *Org. Biomol. Chem.* **2006**, *4*, 3404-3405.
220. Xin, H.; Woolley, A.T. DNA-Templated Nanotube Localization, *J. Am. Chem. Soc.* **2003**, *125*, 8710-8711.
221. Xin, H.; Woolley, A.T. High-Yield DNA-Templated Assembly of Surfactant-Wrapped Carbon Nanotubes, *Nanotechnology* **2005**, *16*, 2238-2241.
222. Li, S.; He, P.; Dong, J.; Guo, Z.; Dai, L. DNA-Directed Self-Assembling of Carbon Nanotubes, *J. Am. Chem. Soc.* **2005**, *127*, 14-15.
223. Kiehl, R.A. Nanoparticle Electronic Architectures Assembled by DNA, *J. Nanopart. Res.* **2000**, *2*, 331-332.

224. Keren, K.; Berman, R.S.; Braun, E. Patterned DNA Metallization by Sequence-Specific Localization of a Reducing Agent, *Nano Lett.* **2004**, *4*, 323-326.
225. Becerril, H.A.; Nelson, A.R.; Woolley, A.T., Micromachined Substrates for Molecular Follow up in DNA-Templated Nanofabrication. In *International Workshop on DNA-Based Molecular Electronics*, Fritzsche., W., Ed. Jena, Germany, **2004**; Vol. *725*, pp 31-40.
226. Kearns, G.J.; Foster, E.W.; Hutchison, J.E. Substrates for Direct Imaging of Chemically Functionalized $SiO_2$ Surfaces by Transmission Electron Microscopy, *Anal. Chem.* **2006**, *78*, 298-303.
227. Keren, K.; Berman, R.S.; Buchstab, E.; Sivan, U.; Braun, E. DNA-Templated Carbon Nanotube Field-Effect Transistor, *Science* **2003**, *302*, 1380-1382.
228. Intel's Transistor Technology Breakthrough Represents Biggest Change to Computer Chips in 40 Years. http://www.intel.com/pressroom/archive/releases/20070128comp.htm (March, 2007).
229. Meet the World's First 45nm Processor. http://www.intel.com/technology/silicon/45nm_technology.htm (March, 2007).
230. Dana, J.D., Mica Group. In *Dana's New Mineralogy: The System of Mineralogy of James Dwight Dana and Edward Salisbury Dana.*, 8th ed.; Wiley: New York, **1997**; pp 1444-1451.
231. Dana, J.D., Graphite. In *Dana's New Mineralogy: The System of Mineralogy of James Dwight Dana and Edward Salisbury Dana.*, 8th ed.; Wiley: New York, **1997**; pp 32-34.
232. Hansma, H.G.; Revenko, I.; Kim, K.; Laney, D.E. Atomic Force Microscopy of Long and Short Double-Stranded Single-Stranded and Triple-Stranded Nucleic Acids, *Nucl. Acids Res.* **1996**, *24*, 713-20.
233. Thomson, N.H.; Kasas, S.; Smith, B.; Hansma, H.G.; Hansma, P.K. Reversible Binding of DNA to Mica for AFM Imaging, *Langmuir* **1996**, *12*, 5905-5908.
234. Bussiek, M.; Mucke, N.; Langowski, J. Polylysine-Coated Mica Can Be Used to Observe Systematic Changes in the Supercoiled DNA Conformation by Scanning Force Microscopy in Solution, *Nucl. Acids Res.* **2003**, *31*, e137.
235. Yoda, S.; Han, S.P.; Kudo, H.; Kwak, K.J.; Fujihira, M. Deoxyribonucleic Acid Interaction with Silanized Surfaces, *Jpn. J. Appl. Phys. Part 1* **2004**, *43*, 6297-6302.
236. Han, S.P.; Yoda, S.; Kwak, K.J.; Suga, K.; Fujihira, M. Interpretation of DNA Adsorption on Silanized Surfaces by Measuring Interaction Forces at Various pHs Using Atomic Force Microscopy, *Ultramicroscopy* **2005**, *105*, 148-154.
237. Nakao, H.; Hayashi, H.; Yoshino, T.; Sugiyama, S.; Otobe, K.; Ohtani, T. Development of Novel Polymer-Coated Substrates for Straightening and Fixing DNA, *Nano Lett.* **2002**, *2*, 475-479.
238. Bensimon, A.; Simon, A.; Chiffaudel, A.; Croquette, V.; Heslot, F.; Bensimon, D. Alignment and Sensitive Detection of DNA by a Moving Interface, *Science* **1994**, *265*, 2096-2098.
239. Bensimon, D.; Simon, A.J.; Croquette, V.; Bensimon, A. Stretching DNA with a Receding Meniscus - Experiments and Models, *Phys. Rev. Lett.* **1995**, *74*, 4754-4757.

240. Woolley, A.T.; Kelly, R.T. Deposition and Characterization of Extended Single-Stranded DNA Molecules on Surfaces, *Nano Lett.* **2001**, *1*, 345-348.
241. Otobe, K.; Ohtani, T. Behavior of DNA Fibers Stretched by Precise Meniscus Motion Control, *Nucl. Acids Res.* **2001**, *29*, e109.
242. Li, J.; Bai, C.; Wang, C.; Zhu, C.; Lin, Z.; Li, Q.; Cao, E. A Convenient Method of Aligning Large DNA Molecules on Bare Mica Surfaces for Atomic Force Microscopy, *Nucl. Acids Res.* **1998**, *26*, 4785-4786.
243. Yokota, H.; Sunwoo, J.; Sarikaya, M.; Van den Engh, G.; Aebersold, R. Spin-Stretching of DNA and Protein Molecules for Detection by Fluorescence and Atomic Force Microscopy, *Anal. Chem.* **1999**, *71*, 4418-4422.
244. Guan, J.; Lee, L.J. Generating Highly Ordered DNA Nanostrand Arrays, *Proc. Natl. Acad. Sci, USA* **2005**, *102*, 18321-18325.
245. Ogura, T.; Malcomson, M.; Fernando, Q. Mechanism of Copper Deposition in Electroless Plating, *Langmuir* **1990**, *6*, 1709-1710.
246. Takano, N.; Hosoda, N.; Yamada, T.; Osaka, T. Mechanism of the Chemical Deposition of Nickel on Silicon Wafers in Aqueous Solution, *J. Electrochem. Soc.* **1999**, *146*, 1407-1411.
247. Feldstein, N.; Amodio, P.R. Anionic Inhibition in Electroless Plating, *J. Electrochem. Soc.* **1970**, *117*, 1110-1113.
248. Ohno, I.; Wakabayashi, O.; Haruyama, S. Anodic Oxidation of Reductants in Electroless Plating, *J. Electrochem. Soc.* **1985**, *132*, 2323-2330.
249. Wolfang, R., Electroless Nickel Baths. In *Electroless Nickel Plating*, Finishing Publications LTD: Stevenage, Hertfordshire, UK, **1991**; pp 9-32.
250. Mahlkow, H.; Middeke, R.; Wollf, J., Electrolessly Deposited Copper Coatings. In *Electroplating and Electroless Plating of Copper and Its Alloys*, Kanani, N., Ed. Finishing Publicaitons Limited: Stevenage, Hertfordshire, UK, **2003**; pp 133-157.
251. Tam, T.M. Cyclic Voltammogram of Formaldehyde and Its Related Species in Electroless Copper Solution, *J. Electrochem. Soc.* **1985**, *132*, 806-810.
252. Lam, P.; Kumar, K.; Wnek, G.E.; Przybycien, T.M. Electroless Gold Plating of 316 L Stainless Steel Beads, *J. Electrochem. Soc.* **1999**, *146*, 2517-2521.
253. Iacovangelo, C.D.; Zarnoch, K.P. Substrate-Catalyzed Electroless Gold Plating, *J. Electrochem. Soc.* **1991**, *138*, 983-988.
254. Iacovangelo, C.D. Autocatalytic Electroless Gold Deposition Using Hydrazine and Dimethylamine Borane as Reducing Agents, *J. Electrochem. Soc.* **1991**, *138*, 976-982.
255. Singh, B.K.; Chatterjee, A.; Daw, A.N.; Mitra, R.N. Study of the Contact Resistance of Electroless Nickel-Boron-Doped Silicon Using Sodium Borohydride as Reducing Agent, *J. Electrochem. Soc.* **1989**, *136*, 785-787.
256. Sullivan, A.M.; Kohl, P.A. Electrochemical Study of the Gold Thiosulfate Reduction, *J. Electrochem. Soc.* **1997**, *144*, 1686-1690.
257. Diaz, R.; Arbiol, J.; Cirera, A.; Sanz, F.; Peiro, F.; Cornet, A.; Morante, J.R. Electroless Addition of Catalytic Pd to $SnO_2$ Nanopowders, *Chem. Mater.* **2001**, *13*, 4362-4366.

258. Bailey, S.I.; Ritchie, I.M.; Hewgill, F.R. The Construction and Use of Potential-pH Diagrams in Organic Oxidation-Reduction Reactions, *J. Chem. Soc. Perkin Trans.* **1983**, *11*, 645-652.
259. Muylder, J.V.; Pourbaix, M., Carbon. In *Atlas of Electrochemical Equilibria in Aqueous Solutions*, Pergamon Press: London, UK, **1966**; pp 449-457.
260. Zhang, Q.; Wu, Y.; Sun, X.; Ortega, J. Kinetics of Catalytic Hydrolysis of Stabilized Sodium Borohydride Solutions, *Ind. Eng. Chem. Res.* **2007**, *46*, 1120-1124.
261. Kuzmik, J.J., Plating on Plastics. In *Electroless Plating*, Mallory, G. O.; Hajdu, J. D., Eds. American Electroplaters and Surface Finishers Society: Orlando, FL, **1990**; pp 377-399.
262. Hajdu, J.D., Surface Preparation for Electroless Plating. In *Electroless Plating*, Mallory, G. O.; Hajdu, J. D., Eds. American Electroplaters and Surface Finishers Society: Orlando, FL, **1990**; pp 193-206.
263. Kind, H.; Bittner, A.M.; Cavalleri, O.; Kern, K.; Greber, T. Electroless Deposition of Metal Nanoislands on Aminothiolate-Functionalized Au(111) Electrodes, *J. Phys. Chem. B* **1998**, *102*, 7582-7589.
264. Ishida, M.; Kasuga, M.; Kaneko, T.; Shimoda, T. Selective Deposition of Electroless Plating Films Using the Difference between the Functional Groups of Self-Assembled Monolayers, *Jpn. J. Appl. Phys. Part 2* **2000**, *39*, L227-L229.
265. Wolfang, R., The Practice of Electroless Nickel Plating. In *Electroless Nickel Plating*, Finishing Publications LTD: Stevenage, Hertfordshire, UK, **1991**; pp 33-63.
266. Mallory, G.O., The Fundamental Aspects of Electroless Nickel Plating. In *Electroless Plating*, Mallory, G. O.; Hajdu, J. D., Eds. American Electroplaters and Surface Finishers Society: Orlando, FL, **1990**; pp 1-57.
267. Skoog, D.A.; Holler, J.F.; Nieman, T.A., An Introduction to UV-Vis Molecular Absorption Spectroscopy. In *Principles of Instrumental Analysis*, 5th ed.; Brooks Cole: USA, **1998**; pp 300-306.
268. Sambrook, J.; Fritsch, E.F.; Maniatis, T., Quantitation of DNA and RNA. In *Molecular Cloning: A Laboratory Manual*, 2nd ed.; Cold Spring Harbor Laboratory Press: Cold Spring Harbor, NY, **1989**; Vol. *3*, p E.5.
269. Siegbahn, K. Electron Spectroscopy for Atoms, Molecules and Condensed Matter, *Rev. Mod. Phys.* **1982**, *54*, 709-728.
270. Turner, N.H. Surface Analysis: X-Ray Photoelectron Spectroscopy and Auger Electron Spectroscopy, *Anal. Chem.* **1988**, *60*, 377R-387R.
271. Skoog, D.A.; Holler, J.F.; Nieman, T.A., X-Ray Photoelectron Spectroscopy. In *Principles of Instrumental Analysis*, 5th ed.; Brooks Cole: USA, **1998**; pp 538-543.
272. Rossi, A.; Elsener, B.; Spencer, N.D. XPS Surface Analysis: Imaging and Spectroscopy of Metal and Polymer Surfaces, *Spectroscopy Europe* **2005**, *16*, 14-19.
273. Kiskinova, M.P. Chemical Characterization of Surfaces and Interfaces with Submicron Spatial Resolution, *Surf. Interf. Anal.* **2000**, *30*, 464-471.
274. Renault, O.; Samour, D.; Damlencourt, J.F.; Blin, D.; Martin, F.; Marthon, S.; Barrett, N.T.; Besson, P. $HfO_2/SiO_2$ Interface Chemistry Studied by Synchrotron

Radiation X-Ray Photoelectron Spectroscopy, *Appl. Phys. Lett.* **2002**, *81*, 3627-3629.
275. Bilgin, V.; Kose, S.; Atay, F.; Akyuz, I. The Effect of Sn Concentration on Some Physical Properties of Zinc Oxide Films Prepared by Ultrasonic Spray Pyrolysis, *J. Mater. Sci.* **2005**, *40*, 1909-1915.
276. Ingo, G.M.; Plescia, P.; Angelini, E.; Riccucci, C.; de Caro, T. Bronze Roman Mirrors: The Secret of Brightness, *Appl. Phys. A* **2006**, *83*, 611-615.
277. Kang, S.W.; Kim, W.K.; Rhee, S.W. The Electrical and Interface Properties of Metal-Ferroelectric (Lanthanum Substituted Bismuth Titanate: BLT)-Insulator-Semiconductor (MFIS) Structures with Various Insulators, *J. Mater. Sci.* **2007**, *42*, 652-659.
278. Williams, D.B.; Carter, C.B., X-Ray Spectrometry. In *Transmission Electron Microscopy. A Textbook for Materials Science*, Plenum Press: New York, **1996**; pp 555-570.
279. Goldstein, J.I.; Newbury, D.; Joy, D.; Lyman, C.; Echlin, P.; Lifshin, E.; Sawyer, L.; Michael, J., X-Ray Spectral Measurement, EDS and WDS. In *Scanning Electron Microscopy and X-Ray Microanalysis*, 3rd ed.; Kluwer Academic/Plenum Publishers: New York, **2003**; pp 297-322.
280. Goldstein, J.I.; Newbury, D.; Joy, D.; Lyman, C.; Echlin, P.; Lifshin, E.; Sawyer, L.; Michael, J., X-Ray Mapping. In *Scanning Electron Microscopy and X-Ray Microanalysis*, 3rd ed.; Kluwer Academic/Plenum Publishers: New York, **2003**; pp 485-499.
281. Goldstein, J.I.; Newbury, D.; Joy, D.; Lyman, C.; Echlin, P.; Lifshin, E.; Sawyer, L.; Michael, J., Quantitative X-Ray Analysis. In *Scanning Electron Microscopy and X-Ray Microanalysis*, 3rd ed.; Kluwer Academic/Plenum Publishers: New York, **2003**; pp 391-449.
282. Gao, C.; Li, W.; Morimoto, H.; Nagaoka, Y.; Maekawa, T. Magnetic Carbon Nanotubes: Synthesis by Electrostatic Self-Assembly Approach and Application in Biomanipulations, *J. Phys. Chem. B* **2006**, *110*, 7213-7220.
283. Binnig, G.; Rohrer, H.; Gerber, Ch.; Weibel, E. Tunnelling through a Controllable Vacuum Gap, *Appl. Phys. Lett.* **1981**, *40*, 178-180.
284. Binnig, G.; Rohrer, H.; Gerber, Ch.; Weibel, W. Surface Studies by Scanning Tunneling Microscopy, *Phys. Rev. Lett.* **1982**, *49*, 57-61.
285. Binnig, G.; Frank, K.H.; Fuchs, H.; Garcia, N.; Reihl, B.; Rohrer, H.; Salvan, F.; Williams, A.R. Tunneling Spectroscopy and Inverse Photoemission: Image and Field States, *Phys. Rev. Lett.* **1985**, *55*, 991-994.
286. Binnig, G.; Rohrer, H. Scanning Tunneling Microscopy - from Birth to Adolescence, *Rev. Mod. Phys.* **1987**, *59*, 615-625.
287. Avouris, P. Probing the Wave Properties of Electrons and Manipulating Atoms at Surfaces with the Scanning Tunneling Microscope, *Acc. Chem. Res.* **1994**, *27*, 159-165.
288. Fishlock, T.W.; Oral, A.; Egdell, R.G.; Pethica, J.B. Manipulation of Atoms across a Surface at Room Temperature, *Nature* **2000**, *404*, 743-745.
289. Stroscio, J.A.; Celotta, R.J. Controlling the Dynamics of a Single Atom in Lateral Atom Manipulation, *Science* **2004**, *306*, 242-247.

290. Binnig, G.; Quate, C.F.; Gerber, C. Atomic Force Microscope, *Phys. Rev. Lett.* **1986**, *56*, 930-933.
291. Meyer, G.; Amer, N.M. Novel Optical Approach to Atomic Force Microscopy, *Appl. Phys. Lett.* **1988**, *53*, 1045-1047.
292. Sarid, D., Deflection Detection System. In *Scanning Force Microscopy: With Applications to Electric, Magnetic, and Atomic Forces*, Oxford University Press: New York, **1994**; pp 119-128.
293. Hlady, V.; Pierce, M.; Pungor, A. Novel Method of Measuring Cantilever Deflection During an AFM Force Measurement, *Langmuir* **1996**, *12*, 5244-5246.
294. Hansma, H.G.; Vesenka, J.; Siegerist, C.; Kelderman, G.; Morrett, H.; Sinsheimer, R.L.; Elings, V.; Bustamante, C.; Hansma, P.K. Reproducible Imaging and Dissection of Plasmid DNA under Liquid with the Atomic Force Microscope, *Science* **1992**, *256*, 1180-1184.
295. Hansma, P.K.; Cleveland, J.P.; Radmacher, M.; Walters, D.A.; Hillner, P.E.; Bezanilla, M.; Fritz, M.; Vie, D.; Hansma, H.G.; Prater, C.B.; Massie, J.; Fukunaga, L.; Gurley, J.; Elings, V. Tapping Mode Atomic Force Microscopy in Liquids, *Appl. Phys. Lett.* **1994**, *64*, 1738-1740.
296. Sarid, D., Atomic Force Microscopy. In *Scanning Force Microscopy: With Applications to Electric, Magnetic, and Atomic Forces*, Oxford University Press: New York, **1994**; pp 181-218.
297. Hansma, H.G. Surface Biology of DNA by Atomic Force Microscopy, *Annu. Rev. Phys. Chem.* **2001**, *52*, 71-92.
298. Schimmel, T.; Koch, T.; Kueppers, J.; Lux-Steiner, M. True Atomic Resolution under Ambient Conditions Obtained by Atomic Force Microscopy in the Contact Mode, *Appl. Phys. A* **1999**, *68*, 399-402.
299. Bullard, J.W.; Cima, M.J. Orientation Dependence of the Isoelectric Point of $TiO_2$ (Rutile) Surfaces, *Langmuir* **2006**, *22*, 10264-10271.
300. Lüebben, J.F.; Johannsmann, D. Nanoscale High-Frequency Contact Mechanics Using an AFM Tip and a Quartz Crystal Resonator, *Langmuir* **2004**, *20*, 3698-3703.
301. Dietzel, D.; Faucher, M.; Iaia, A.; Aime, J.P.; Marsaudon, S.; Bonnot, A.M.; Bouchiat, V.; Couturier, G. Analysis of Mechanical Properties of Single Wall Carbon Nanotubes Fixed at a Tip Apex by Atomic Force Microscopy, *Nanotechnology* **2005**, *16*, S73-S78.
302. Gracias, D.H.; Somorjai, G.A. Continuum Force Microscopy Study of the Elastic Modulus, Hardness and Friction of Polyethylene and Polypropylene Surfaces, *Macromol.* **1998**, *31*, 1269-1276.
303. Cho, J.H.; Lee, D.H.; Lim, J.A.; Cho, K.; Je, J.H.; Yi, J.M. Evaluation of the Adhesion Properties of Inorganic Materials with High Surface Energies, *Langmuir* **2004**, *20*, 10174-10178.
304. Knez, M.; Sumser, M.P.; Bittner, A.M.; Wege, C.; Jeske, H.; Hoffmann, D.M.P.; Kuhnke, K.; Kern, K. Binding the Tobacco Mosaic Virus to Inorganic Surfaces, *Langmuir* **2004**, *20*, 441-447.
305. Cheng, X.; Canavan, H.E.; Stein, M.J.; Hull, J.R.; Kweskin, S.J.; Wagner, M.S.; Somorjai, G.A.; Castner, D.G.; Ratner, B.D. Surface Chemical and Mechanical

Properties of Plasma-Polymerized N-Isopropylacrylamide, *Langmuir* **2005**, *21*, 7833-7841.
306. Kim, Y.; Lieber, C.M. Machining Oxide Thin Films with an Atomic Force Microscope: Pattern and Object Formation on the Nanometer Scale, *Science* **1992**, *257*, 375-377.
307. Piner, R.D.; Zhu, J.; Xu, F.; Hong, S.; Mirkin, C.A. "Dip-Pen" Nanolithography, *Science* **1999**, *283*, 661-663.
308. Rolandi, M.; Suez, I.; Dai, H.; Frechet, J.M.J. Dendrimer Monolayers as Negative and Positive Tone Resists for Scanning Probe Lithography, *Nano Lett.* **2004**, *4*, 889-893.
309. Bozovic, D.; Bockrath, M.; Hafner, J.H.; Lieber, C.M.; Park, H.; Tinkham, M. Electronic Properties of Mechanically Induced Kinks in Single-Walled Carbon Nanotubes, *Appl. Phys. Lett.* **2001**, *78*, 3693-3695.
310. Scheuring, S.; Seguin, J.; Marco, S.; Levy, D.; Robert, B.; Rigaud, J.L. Nanodissection and High-Resolution Imaging of the Rhodopseudomonas Viridis Photosynthetic Core Complex in Native Membranes by AFM, *Proc. Natl. Acad. Sci. USA* **2003**, *100*, 1690-1693.
311. Poggi, M.A.; Gadsby, E.D.; Bottomley, L.A.; King, W.P.; Oroudjev, E.; Hansma, H. Scanning Probe Microscopy, *Anal. Chem.* **2004**, *76*, 3429-3444.
312. Scheuring, S.; Fotiadis, D.; Moller, C.; Muller, S.A.; Engel, A.; Muller, D.J. Single Proteins Observed by Atomic Force Microscopy, *Single Mol.* **2001**, *2*, 59-67.
313. Oroudjev, E.; Soares, J.; Arcdiacono, S.; Thompson, J.B.; Fossey, S.A.; Hansma, H.G. Segmented Nanofibers of Spider Dragline Silk: Atomic Force Microscopy and Single-Molecule Force Spectroscopy, *Proc. Natl. Acad. Sci. USA* **2002**, *99*, 6460-6465.
314. Sarkar, A.; Robertson, R.B.; Fernandez, J.M. Simultaneous Atomic Force Microscope and Fluorescence Measurements of Protein Unfolding Using a Calibrated Evanescent Wave, *Proc. Natl. Acad. Sci. USA* **2004**, *101*, 12882-12886.
315. Discher, D.E.; Bhasin, N.; Johnson, C.P. Covalent Chemistry on Distended Proteins, *Proc. Natl. Acad. Sci. USA* **2006**, *103*, 7533-7534.
316. Sewald, N.; Wilking, S.D.; Eckel, R.; Albu, S.; Wollschlaeger, K.; Gaus, K.; Becker, A.; Bartels, F.W.; Ros, R.; Anselmetti, D. Probing DNA-Peptide Interaction Forces at the Single-Molecule Level, *J. Pept. Sci.* **2006**, *12*, 836-842.
317. Hansma, H.G.; Sinsheimer, R.L.; Li, M.Q.; Hansma, P.K. Atomic Force Microscopy of Single- and Double-Stranded DNA, *Nucl. Acids Res.* **1992**, *20*, 3585-3590.
318. Hansma, H.G. Surface Biology of DNA by Atomic Force Microscopy, *Annu. Rev. Phys. Chem.* **2001**, *52*, 71-92.
319. Hansma, H.G.; Kasuya, K.; Oroudjev, E. Atomic Force Microscopy Imaging and Pulling of Nucleic Acids, *Curr. Opin. Struct. Biol.* **2004**, *14*, 380-385.
320. Lyubchenko, Y.L. DNA Structure and Dynamics: An Atomic Force Microscopy Study, *Cell Biochem. Biophys.* **2004**, *41*, 75-98.

321. Oberleithner, H.; Brinckmann, E.; Schwab, A.; Krohne, G. Imaging Nuclear Pores of Aldosterone-Sensitive Kidney Cells by Atomic Force Microscopy, *Proc. Natl. Acad. Sci. USA* **1994**, *91*, 9784-9788.
322. McElfresh, M.; Baesu, E.; Balhorn, R.; Belak, J.; Allen, M.J.; Rudd, R.E. Combining Constitutive Materials Modeling with Atomic Force Microscopy to Understand the Mechanical Properties of Living Cells, *Proc. Natl. Acad. Sci. USA* **2002**, *99*, 6493-6497.
323. Wright, C.J.; Armstrong, I. The Application of Atomic Force Microscopy Force Measurements to the Characterization of Microbial Surfaces, *Surf. Interf. Anal.* **2006**, *38*, 1419-1428.
324. Thordarson, P.; Atkin, R.; Kalle, W.H.J.; Warr, G.G.; Braet, F. Developments in Using Scanning Probe Microscopy to Study Molecules on Surfaces - from Thin Films and Single-Molecule Conductivity to Drug-Living Cell Interactions, *Aust. J. Chem.* **2006**, *59*, 359-375.
325. Yang, L.; Wang, K.; Tan, W.; He, X.; Jin, R.; Li, J.; Li, H. Atomic Force Microscopy Study of Different Effects of Natural and Semisynthetic β-Lactam on the Cell Envelope of Escherichia Coli, *Anal. Chem.* **2006**, *78*, 7341-7345.
326. Wong, S.S.; Joselevich, E.; Woolley, A.T.; Cheung, C.L.; Lieber, C.M. Covalently Functionalized Nanotubes as Nanometre-Sized Probes in Chemistry and Biology, *Nature* **1998**, *394*, 52-55.
327. Woolley, A.T. Biofunctionalization of Carbon Nanotubes for Atomic Force Microscopy Imaging, *Meth. Mol. Biol.* **2004**, *283*, 305-319.
328. Kamruzzahan, A.S.M.; Ebner, A.; Wildling, L.; Kienberger, F.; Riener, C.K.; Hahn, C.D.; Pollheimer, P.D.; Winklehner, P.; Hoelzl, M.; Lackner, B.; Schoerkl, D.M.; Hinterdorfer, P.; Gruber, H.J. Antibody Linking to Atomic Force Microscope Tips Via Disulfide Bond Formation, *Bioconjugate Chem.* **2006**, *17*, 1473-1481.
329. Ito, T.; Citterio, D.; Buehlmann, P.; Umezawa, Y. Observation of Silver and Hydrogen Ion Binding to Self-Assembled Monolayers Using Chemically Modified AFM Tips, *Langmuir* **1999**, *15*, 2788-2793.
330. Hafner, J.H.; Cheung, C.L.; Woolley, A.T.; Lieber, C.M. Structural and Functional Imaging with Carbon Nanotube AFM Probes, *Prog. Biophys. Mol. Biol.* **2001**, *77*, 73-110.
331. Beaulieu, L.Y.; Cumyn, V.K.; Eberman, K.W.; Krause, L.J.; Dahn, J.R. A System for Performing Simultaneous in Situ Atomic Force Microscopy/Optical Microscopy Measurements on Electrode Materials for Lithium-Ion Batteries, *Rev. Sci. Instrum.* **2001**, *72*, 3313-3319.
332. Wong, S.S.; Harper, J.D.; Lansbury, P.T., Jr.; Lieber, C.M. Carbon Nanotube Tips: High Resolution Probes for Imaging Biological Systems, *J. Am. Chem. Soc.* **1998**, *120*, 603-604.
333. Hafner, J.H.; Cheung, C.-L.; Oosterkamp, T.H.; Lieber, C.M. High-Yield Assembly of Individual Single-Walled Carbon Nanotube Tips for Scanning Probe Microscopies, *J. Phys. Chem. B.* **2001**, *105*, 743-746.
334. Hafner, J.H.; Cheung, C.L.; Lieber, C.M. Growth of Nanotubes for Probe Microscopy Tips, *Nature* **1999**, *398*, 761-762.

335. Cheung, C.L.; Hafner, J.H.; Lieber, C.M. Carbon Nanotube Atomic Force Microscopy Tips: Direct Growth by Chemical Vapor Deposition and Application to High Resolution Imaging, *Proc. Natl. Acad. Sci. USA* **2000**, *97*, 3809-3813.
336. Ye, Q.; Cassell, A.M.; Liu, H.; Chao, K.-J.; Han, J.; Meyyappan, M. Large-Scale Fabrication of Carbon Nanotube Probe Tips for Atomic Force Microscopy Critical Dimension Imaging Applications, *Nano Lett.* **2004**, *4*, 1301-1308.
337. Nishijima, H.; Kamo, S.; Akita, S.; Nakayama, Y.; Hohmura, K.I.; Yoshimura, S.H.; Takeyasu, K. Carbon-Nanotube Tips for Scanning Probe Microscopy: Preparation by a Controlled Process and Observation of Deoxyribonucleic Acid, *Appl. Phys. Lett.* **1999**, *74*, 4061-4063.
338. Simpson, G.J.; Sedin, D.L.; Rowlen, K.L. Surface Roughness by Contact Versus Tapping Mode Atomic Force Microscopy, *Langmuir* **1999**, *15*, 1429-1434.
339. Ruska, E. The Development of the Electron Microscope and of Electron Microscopy, *Rev. Mod. Phys.* **1987**, *59*, 627-638.
340. Williams, D.B.; Carter, C.B., Electron Sources. In *Transmission Electron Microscopy. A Textbook for Materials Science*, Plenum Press: New York, **1996**; pp 69-82.
341. Williams, D.B.; Carter, C.B., Lenses, Apertures and Resolution. In *Transmission Electron Microscopy. A Textbook for Materials Science*, Plenum Press: New York, **1996**; pp 87-103.
342. Williams, D.B.; Carter, C.B., The Instrument. In *Transmission Electron Microscopy. A Textbook for Materials Science*, Plenum Press: New York, **1996**; pp 133-153.
343. Williams, D.B.; Carter, C.B., Elastic Scattering. In *Transmission Electron Microscopy. A Textbook for Materials Science*, Plenum Press: New York, **1996**; pp 37-46.
344. Williams, D.B.; Carter, C.B., Inelastic Scattering and Beam Damage. In *Transmission Electron Microscopy. A Textbook for Materials Science*, Plenum Press: New York, **1996**; pp 51-65.
345. Goldstein, J.I.; Newbury, D.; Joy, D.; Lyman, C.; Echlin, P.; Lifshin, E.; Sawyer, L.; Michael, J., Electron Beam-Specimen Interactions. In *Scanning Electron Microscopy and X-Ray Microanalysis*, 3rd ed.; Kluwer Academic/Plenum Publishers: New York, **2003**; pp 61-98.
346. Goldstein, J.I.; Newbury, D.; Joy, D.; Lyman, C.; Echlin, P.; Lifshin, E.; Sawyer, L.; Michael, J., Generation of X-Rays in the SEM Specimen. In *Scanning Electron Microscopy and X-Ray Microanalysis*, 3rd ed.; Kluwer Academic/Plenum Publishers: New York, **2003**; pp 271-295.

# CHAPTER 2: IONIC SURFACE MASKING FOR LOW BACKGROUND IN SINGLE- AND DOUBLE-STRANDED DNA-TEMPLATED SILVER AND COPPER NANORODS*

## 2.1. Introduction

Integrated microprocessors play a central role in many aspects of modern civilization. Continued reductions in feature dimensions, coupled with increased computing power of integrated circuits, have facilitated their application in diverse fields, from space exploration vehicles to intelligent credit cards and implantable medical devices. But how much smaller can circuit components be manufactured? As microchip complexity increases, wires must travel longer distances and occupy more space. Because of their considerable dimensions, wires contribute significantly to the difficulties associated with charge transport speed and energy dissipation, thus limiting the overall performance of integrated circuits [1]. Current mass fabrication procedures can construct features in the 130 nm range [2], but substantially more expensive methods are required presently to reach the low nanometer size regime. Thus, cost effective nanowire fabrication techniques will be needed to facilitate the ultimate miniaturization of integrated electronics.

* This chapter is adapted with permission from *J. Mater. Chem.* **2004**, *14*, 611–616. Copyright 2004 The Royal Society of Chemistry.

Recently, several unconventional approaches have been reported for the templated and potentially parallel construction of nanowires: electrodeposition of metallic fibers inside porous matrices [3], ultrasonication of reverse micelles containing silver solutions [4], metallization of protein microtubules [5] or fibrils [6], directed self-assembly of carbon nanotubes along DNA strands [7], and in-situ growth of metallic sheaths on double stranded (ds) DNA [8–13]. Templated nanostructures of silver [8], platinum [9], palladium [10], gold [11,12] and copper [13] have been synthesized in this last fashion. Bottom-up, DNA-based approaches are particularly appealing because of the potential for using DNA molecules as nanometer-scale localization templates, and because of the inherently parallel fashion in which structures can be fabricated. However, a major disadvantage of previously reported schemes for DNA-templated fabrication of metallic nanowires is the susceptibility to nonspecific substrate metallization. Even though selectivity has been demonstrated in metallizing specific sequences on DNA strands [12], control over nonspecific metallization or contamination of the substrate during metallization has not achieved the same degree of exquisiteness.

Nonspecific metallization presents complications for device characterization using scanning probe microscopy techniques, as delicate device features are often obscured with surface debris. More importantly, this nonspecific metallic background can hinder the performance of the constructed devices. Typical substrate modifications, such as silanization [14] or thiol chemistry [11], are designed to alter surface affinity toward DNA, but do not decrease nonspecific metallization of the substrate. Even when the DNA strand is not in direct contact with the surface, for example as a bridge suspended between two electrodes, atomic force microscopy (AFM) images reveal significant

metallization of the substrate below [8]. Nonspecific metallization has been addressed partially by derivatizing the DNA so that the reducing agent is contained within the strand. Unfortunately, this covalent DNA modification approach does not produce continuous nanowires; thus, a developing step is still required, which can lead to nonspecific metallization [12].

My research has focused on devising facile ways for performing DNA-templated nanofabrication. Woolley's group previously reported a straightforward method to align double- and single-stranded DNA molecules on planar surfaces with simple poly-L-lysine treatment [15], in contrast to more complex surface modification protocols that offer comparable performance [14, 16]. Herein, I demonstrate a significant reduction in nonspecific metallization of the substrate by means of an ionic surface masking approach, which is greatly simplified relative to covalent DNA modification [12].

The ideal masking ion should have high affinity for the $SiO_2$ surface and low or no affinity for binding sites on the DNA. This requires the masking ion to be a cation, so that it can respond to the negative charge of deprotonated surface silanol groups. Moreover, the masking cation must have a charge lower than or at least equal to that of the transition metal ion used for metallization, to minimize displacement of the desired ions from the phosphate sites on the DNA. Further, it is desirable that the masking cation have a full valence shell so that it cannot compete with the metallization cations for chelating sites on the DNA bases [17]. Given these requirements, I have investigated the use of alkali metal cations to passivate $SiO_2$ surfaces, creating both a physical and an electrostatic barrier to the adsorption of transition metal cations used for metallization. Additionally, Group IA cations in aqueous solution are non-reducible and highly soluble,

enabling them to be rinsed off easily once nanowires have been constructed. Due to a structure-breaking effect at the silica-water interface, the affinity of silica surfaces for alkali metal cations follows the sequence: $Cs^+ > K^+ > Na^+ > Li^+$ [18, 19]. Here I demonstrate the effective use of $K^+$ and $Cs^+$ as surface passivation agents against nonspecific metallization in the fabrication of DNA-templated copper and silver nanorods, respectively. Finally, I have used this background reduction approach to demonstrate the feasibility of fabricating silver nanowires from single stranded (ss) DNA template molecules, which have not been reported previously, perhaps due to the only recently overcome difficulty of producing well-elongated ssDNA on surfaces [15]. The importance of this development is that surface ssDNA is available for direct hybridization to complementary probes, unlike dsDNA. Thus, ssDNA should provide an ideal scaffold for the facile positioning of multiple oligonucleotide-coupled nanostructures along surface DNA strands with nanometer-scale precision.

## *2.2. Experimental*

### 2.2.1. Instruments and Materials

All images were obtained using an extended Multimode Nanoscope IIIa atomic force microscope from Digital Instruments (Santa Barbara, CA) and microfabricated, aluminum-coated silicon cantilever-tips from Nanoscience Instruments (Phoenix, AZ). All DNA and nanorod average height measurements were obtained from 100 randomly selected profiles across linear features on each surface. Silicon [100] p-type substrates were obtained from TTI Silicon (Sunnyvale, CA). I acquired 0.1% aqueous poly-L-lysine solution from Ted Pella Inc. (Redding, CA). Double-stranded λ-DNA was obtained from New England Biolabs (Ipswich, MA). Ascorbic acid was purchased from Sigma (St

Louis, MO). Formaldehyde (37% aqueous solution) and $AgNO_3$ were obtained from Fisher (FairLawn, NJ). $Cu(NO_3)_2$ was bought from Mallinckrodt Baker (Paris, KY), $CsNO_3$ was obtained from Johnson Matthey (Ward Hill, MA), and $KNO_3$ was purchased from Columbus Chem (Columbus, WI). I employed an Easypure UV/UF purification system (Barnstead, Dubuque, IA) to provide water for all solutions and rinsings.

### 2.2.2. Silicon Substrate Preparation

Silicon substrates were cleaved into 7 x 7 mm squares, rinsed with acetone and immersed in hot piranha solution (70% $H_2SO_4$, 30% $H_2O_2$) for 20 min. Substrates were then rinsed extensively with water and air dried. Positive charges were generated on the surfaces by adsorption of 40 mL of 1 ppm aqueous poly-L-lysine solution for 10 min, followed by rinsing with ~20 mL of water and air drying.

### 2.2.3. DNA Templates

Single-stranded λ-DNA used in making silver nanorods was created by heat denaturing a dsDNA aliquot at 95 °C for 5 min, followed by immediate placement on ice. Alignment of ssDNA was accomplished as reported previously [15] by translating across a silicon substrate a 1 ng/μL droplet of λ-ssDNA solution in Tris-EDTA (TE) buffer. The moving air–water interface elongated the DNA in the direction of droplet translation. Stretching was performed using a two-axis computer-controlled translation stage. After DNA alignment, substrates were rinsed with water and air dried. Double stranded λ-DNA was deposited similarly on additional silicon substrates for copper nanorod fabrication.

### 2.2.4. Silver Nanorod Fabrication

Substrates with aligned ssDNA were incubated for 30 min with a 10 mM aqueous solution of $CsNO_3$ to allow surface saturation with $Cs^+$. Next, substrates were treated for 30 min with an aqueous solution containing 10% $NH_4OH$, 10 mM $CsNO_3$ and 0.1 mM $AgNO_3$. The silver ions associated electrostatically with the phosphate backbone and coordinated with the nucleotide bases, while the cesium ions minimized $Ag^+$ adsorption on the $SiO_2$ surface. Then, the substrates were rinsed for 5 s with a 10 mM aqueous $CsNO_3$ solution to displace any $Ag^+$ adsorbed to the $SiO_2$. Following this step the silver associated with the DNA was reduced by incubating the substrates for 5 min with a freshly prepared aqueous solution containing 10% $NH_4OH$, 10% formaldehyde and 10 mM $CsNO_3$. Silver nanorods were synthesized by developing the reduced Ag associated with surface DNA using an aqueous solution containing 10% formaldehyde, 0.1 mM $AgNO_3$ and10 mM $CsNO_3$. Finally, developed substrates were rinsed with ~20 mL of water and air dried.

### 2.2.5. Copper Nanorod Fabrication

Double-stranded DNA aligned on silicon substrates was treated with 20 mL of 0.1 M aqueous $KNO_3$ for 25 min, which allowed $K^+$ to associate electrostatically with the $SiO_2$ surface. 20 mL of 1 M $Cu(NO_3)_2$ was then added and incubation proceeded for 4 min more. $Cu^{2+}$ was reduced by adding 20 mL of 0.1 M ascorbic acid solution to the surface and incubating for 2 min. Longer reduction times typically led to greater amounts of nonspecific copper metal deposition. The substrates were then rinsed with ~20 mL of water and air dried. All treatments and rinsings were performed in a $N_2$ atmosphere to reduce DNA cleavage.

## 2.3. *Results and Discussion*

### 2.3.1. Silver Nanorods Templated by ssDNA

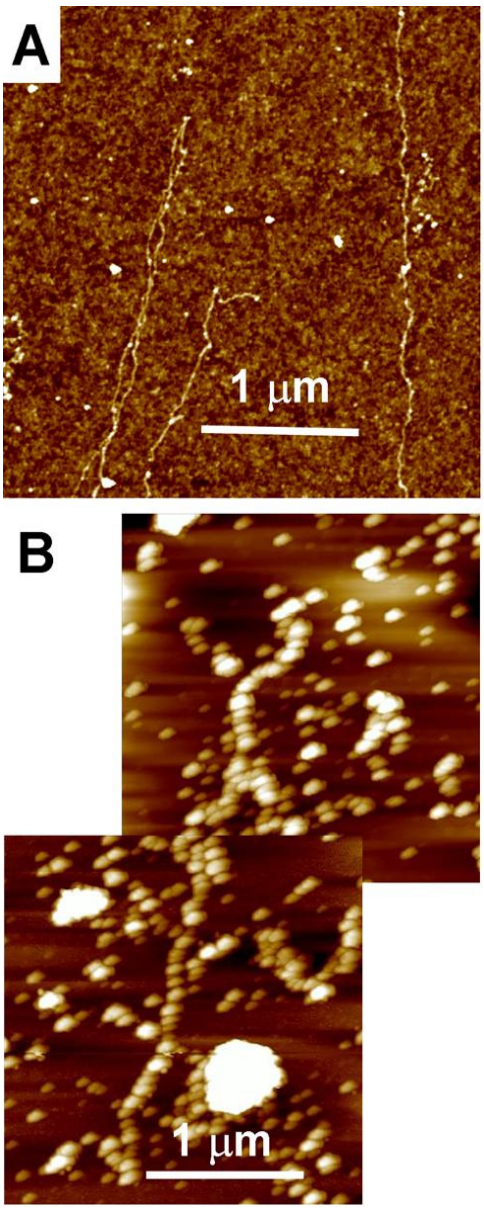


**Figure 2.1.** AFM height images of **(A)** ssDNA aligned on silicon (3 nm height scale) and **(B)** a ssDNA-templated silver nanorod with high background (30 nm height scale) after 20 min of developing time.

**Fig. 2.1A** shows a typical AFM height image of ssDNA aligned on a silicon surface. Measurements on unmodified ssDNA elongated on surfaces like this one yielded an average height of 0.5 nm with a relative standard deviation (RSD) of 27%. **Fig. 2.1B** shows a typical AFM height image of a high-background silver nanorod obtained without employing $Cs^+$ in the fabrication protocol. Measurements across the linear feature yielded an average height of 25 nm with a RSD of 25%. This height RSD is comparable to that of untreated DNA, and the similarity should be ascribed to tip convolution effects. I also note the inconvenience involved in imaging a surface like the one shown in **Fig. 2.1B**; the overall surface roughness, as well as the size and amount of loose particles that tend to stick to the AFM tip cause extensive probe wear and resolution degradation within just a few scans. Control experiments where silver was not added gave no increase of

DNA height nor presented surface debris. Therefore, I conclude that the deposition of silver is responsible for the observed surface features in **Fig. 2.1B**.

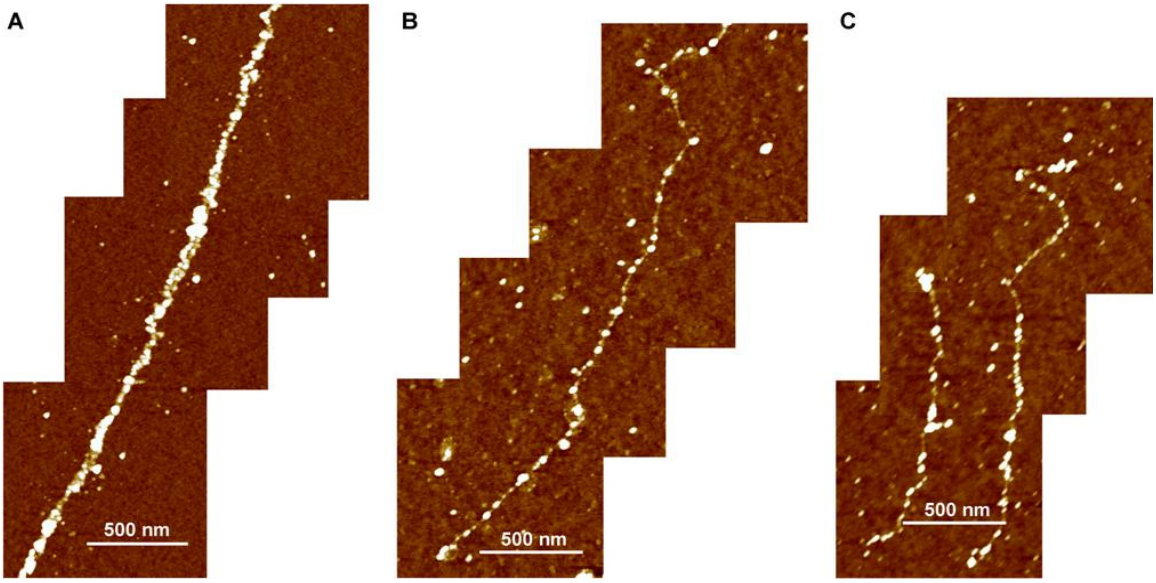


**Figure 2.2.** AFM height images of low background ssDNA-templated silver nanorods. **(A)** 20 min developing time (mean height: 9.3 nm, RSD: 45%,10 nm height scale); **(B)** 5 min developing time (mean height: 3.1 nm, RSD: 60%, 5 nm height scale); and **(C)** 5 min developing time (mean height: 2.9 nm, RSD: 55%, 5 nm height scale). Particle analysis of granular feature dimensions in nanorods in these images yielded the following values. **(A)** Mean particle diameter: 30 nm, RSD: 68%; **(B)** mean particle diameter: 21 nm, RSD: 60%; **(C)** mean particle diameter: 30 nm, RSD: 56%.

**Fig. 2.2** shows AFM height images of silver nanorods grown on three different substrates using my ionic surface masking method. A few nonspecific Ag deposits are still visible, but the contrast with **Fig. 2.1B** is clear. Silver coverage of the DNA is comparable for all strands on the same substrate, and the nanorod height can be controlled by adjusting the developing time. **Fig. 2.3** compares nonspecific silver deposition for unblocked and cesium-masked surfaces. These results indicate that the passivated surfaces have a significantly lower background of nonspecifically deposited surface features. The cesium-treated surfaces yielded a 51% lower particle density, an 86% reduction in average particle height and a 74% reduction in mean particle diameter. On average my ssDNA-templated silver nanorods with a 20 min developing time had

heights on the order of 9 nm, compared to the 0.5 nm height of untreated ssDNA. I expect that this significant difference, corresponding to ~50 atomic layers of silver, may suffice to make these nanorods conductive, but I have not yet tested their electrical behavior. In any case, I am confident that more facile and reliable electrical characterization will be achieved with these better-defined, low-background nanorods.

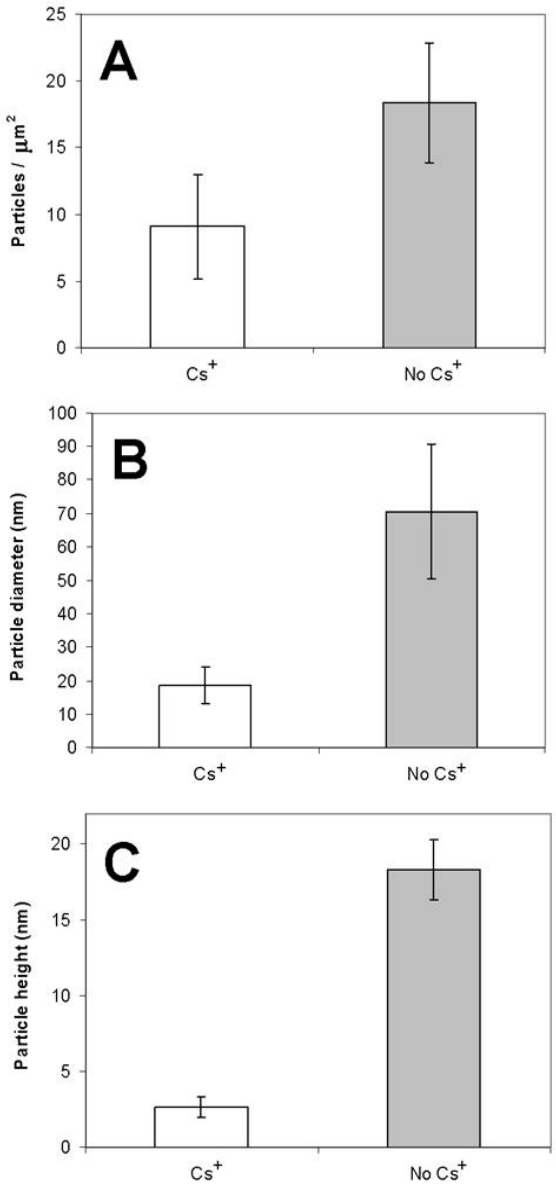


**Figure 2.3.** Comparison of nonspecific deposition in representative images of ssDNA-templated silver nanorod surfaces with (white) and without (grey) cesium treatment. 1000 particles from ten AFM images on five different substrates were analyzed. Error bars represent ±1 standard deviation. **(A)** Mean particle density in particles per $\mu m^2$. **(B)** Mean particle diameter in nm. **(C)** Mean particle height in nm.

The choice of cesium as the masking ion for silver deposition was based on the factors outlined in Section 2.1: $Cs^+$ has a full valence shell, a high affinity for $SiO_2$ surfaces, and the same charge as $Ag^+$. The mechanism of displacement of nonspecifically bound silver ions by cesium ions is complex and probably involves a combination of factors, including ionic size and hydration sphere stability. Affinity for electrostatic DNA binding sites along the phosphate backbone should be governed by steric and diffusion effects with no specificity

for silver or cesium, since both are monovalent. However, competition for the chelating sites on the DNA nucleotide bases does not occur, because the full valence shell of $Cs^+$ prevents its participation in this binding mode. Thus, cesium provides an ideal masking ion since it should bind to the $SiO_2$ surface more strongly than $Ag^+$, without displacing silver ions from the DNA. Silver nanorods fabricated using potassium instead of cesium as the masking ion did not yield a significant reduction in nonspecific deposition, further showing that the high affinity of $Cs^+$ for the $SiO_2$ surface is an essential element for the success of this technique for the blocking of silver ions. Additionally, a comparison of silver deposition in **Fig. 2.1B** and **Fig. 2.2A**, both with a developing time of 20 min, indicates that the presence of cesium ion in the developing solution decreases silver deposition somewhat. This should translate into an increased amount of control over feature size, which may enable the elimination of granular features that are typically seen on silver nanorods grown from DNA templates [8, 12].

### 2.3.2. Copper Nanorods Templated by dsDNA

**Fig. 2.4A** displays a representative AFM height image of a surface with aligned dsDNA. Line profile measurements on this surface yielded an average DNA height of 0.7 nm with a 36% RSD. **Fig. 2.4B** shows typical results of copper deposition without using $K^+$ as a surface masking ion. The average height of the linear nanorod structure was 2.0 nm with a 44% RSD, a significant height increase relative to unmodified dsDNA, which is consistent with earlier work [13]. Control experiments performed by excluding copper or ascorbic acid from the treatment showed negligible DNA-templated or nonspecific deposition. Copper nanorods formed by my methods have smaller heights than silver

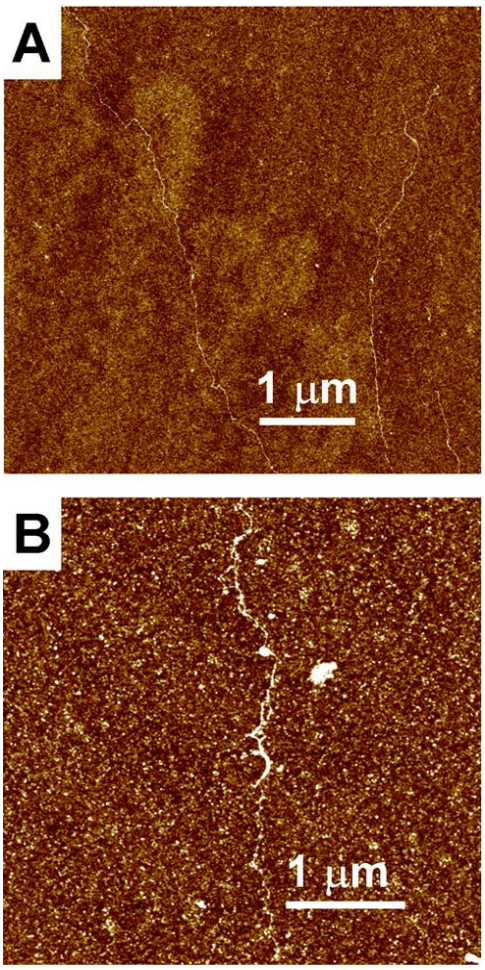


**Figure 2.4.** AFM height images of **(A)** dsDNA aligned on silicon and **(B)** a dsDNA-templated copper nanorod with high nonspecific background. The height scale is 5 nm for both images.

nanorods [13]. I attribute the smaller radial dimensions of the copper nanorods to the different electrochemical and nucleation properties of copper compared to silver.

**Fig. 2.5** shows AFM height images of copper nanorods formed on three different surfaces where elongated dsDNA was treated with $KNO_3$ prior to copper metallization. A clear increase in the height of the filamentous features can be noted relative to **Fig. 2.4A**. Also, the nonspecific copper background on the surface is markedly lower compared to **Fig. 2.4B**. Indeed, nonspecific particle deposition density was reduced by 74%, while nonspecific particle height and diameter remained relatively constant (see **Fig. 2.6**). These data show that $K^+$ effectively reduces the amount of $Cu^{2+}$ that associates with the $SiO_2$ surface before and during the copper reduction stage. Unlike the effect of $Cs^+$ on silver nanorods, the presence of $K^+$ during copper nanorod synthesis reduces only the quantity and not the size of nonspecifically deposited nanoparticles. The smaller dimensions of nonspecific Cu (relative to Ag) deposits on the unmasked surfaces likely account for the minimal size difference between nonspecific copper nanoparticles on unblocked surfaces and those passivated with $K^+$.

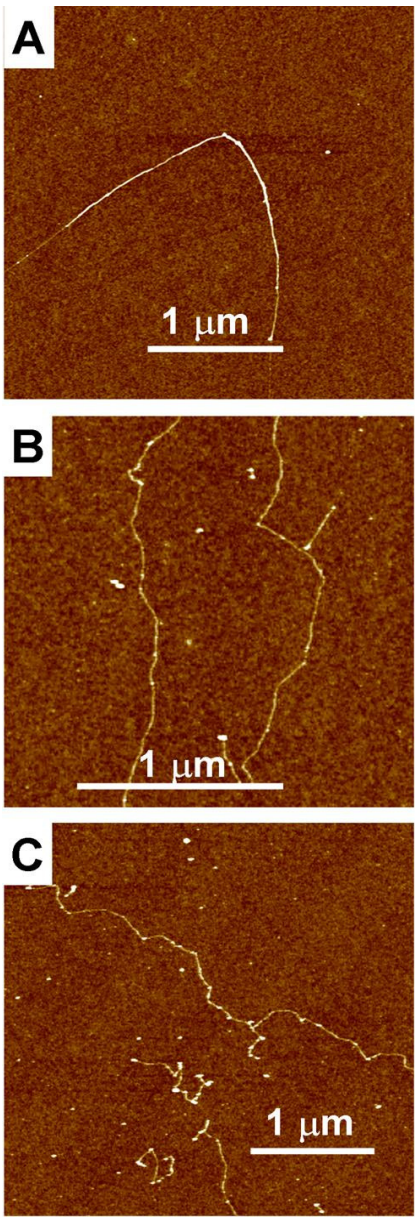


**Figure 2.5** AFM height images of dsDNA-templated copper nanorods fabricated using potassium as a masking ion. Each image was taken from a different substrate. **(A)** Mean height: 3.3 nm, RSD: 54%. **(B)** Mean height: 1.8 nm, RSD: 26%. **(C)** Mean height: 2.2 nm, RSD: 51%. The height scale is 5 nm for all images.

My previous attempts to increase copper nanorod heights through a series of $Cu^{2+}$ and subsequent reduction treatments were unsuccessful, largely because of the high background of nonspecifically deposited copper nanoparticles [13]. These particles provided nucleation sites for further copper deposition in subsequent treatments, causing the nonspecific deposits to obscure the nanorods eventually. However, with this substantial reduction in nonspecific particle density, a limited number of further $Cu^{2+}$ and subsequent reduction treatments should increase nanorod height while limiting interference from nonspecifically deposited copper metal. I anticipate that the ability to make low-background copper nanowires should facilitate studies of their electrical properties and enable their incorporation into nanoscale integrated circuitry.

## *2.4. Conclusions*

I have demonstrated the ability to reduce significantly the nonspecific metallization of silicon substrates used in DNA-templated nanorod fabrication. My approach involves masking silver or copper cation adsorption sites on the $SiO_2$ surface by blocking with alkali metal cations.

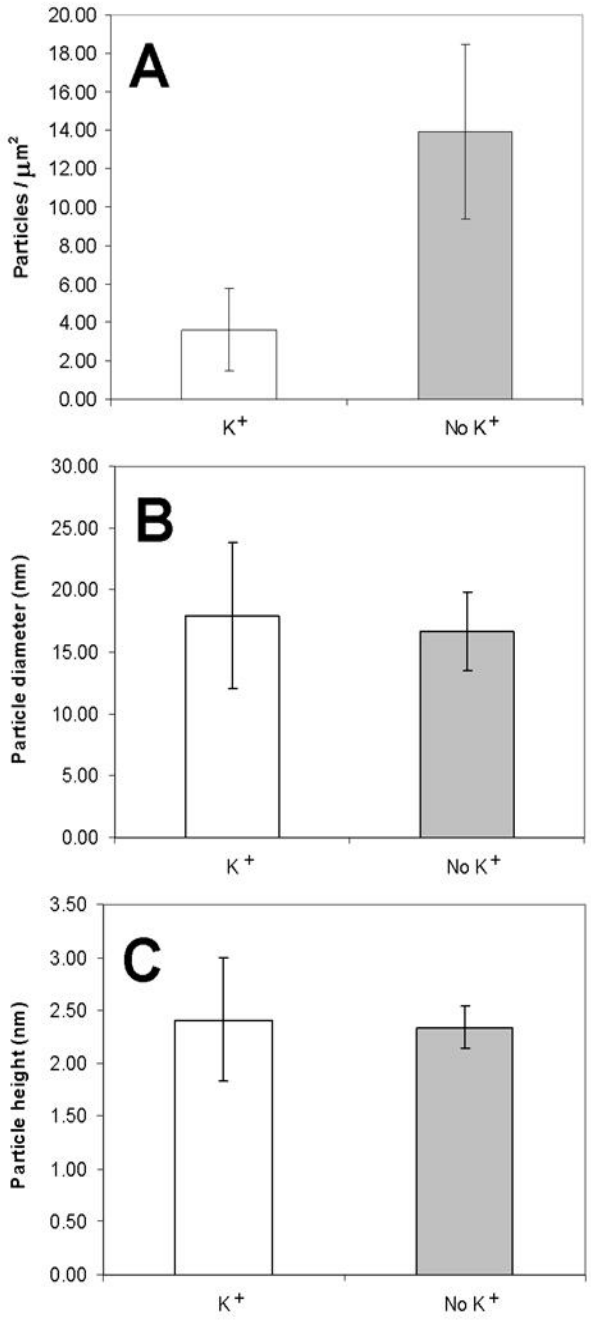


**Figure 2.6.** Nonspecific deposition in representative dsDNA-templated copper nanorods with (white) and without (grey) potassium ion masking. 1200 particles from 14 AFM images on 7 different substrates were analyzed. Error bars represent ±1 standard deviation. **(A)** Mean particle density in particles per $\mu m^2$. **(B)** Mean particle diameter in nm. **(C)** Mean particle height in nm. Height scale is 5 nm for all images.

This increased degree of control over the self-assembly process should allow the bottom-up fabrication of more complex devices with increased yields. I have also reported the first instance of ssDNA serving as a template for the fabrication of silver nanorods. I believe that the ability to manipulate the more biochemically active ssDNA should open a wealth of possibilities for the surface hybridization of different nanostructures that eventually will be interconnected electronically by metallization of the ssDNA template.

## 2.5. References


1. Turton, R. *The Quantum Dot*, Oxford University Press, New York, **1995**, p. 74.
2. The International Technology Roadmap for Semiconductors, **2002** update, http://public.itrs.net. (March, 2007).
3. Choi, J.S.; Sauer, G.; Goring, P.; Nielsch, K.; Wehrspohn, R.B.; Gösele, U. Monodisperse Metal Nanowire Arrays on Si by Integration of Template Synthesis with Silicon Technology, *J. Mater. Chem.* **2003**, *13*, 1100-1103.
4. Zhang, J.; Han, B.; Liu, M.; Liu, D.; Dong, Z.; Liu, J.; Li, D. Ultrasonication-Induced Formation of Silver Nanofibers in Reverse Micelles and Small-Angle X-ray Scattering Studies, *J. Phys. Chem. B* **2003**, *107*, 3679-3683.
5. Fritzsche, W.; Köhler, J.M.; Böhm, K.J.; Unger, E.; Wagner, T.; Kirsch, R.; Mertig, M.; Pompe, W. Wiring of Metallized Microtubules by Electron Beam-Induced Structuring, *Nanotechnology* **1999**, *10*, 331-335.
6. Scheibel, T.; Parthasarathy, R.; Sawicki, G.; Lin, X.M.; Jaegerand, H.; Lindquist, S.L. Conducting Nanowires Built by Controlled Self-assembly of Amyloid Fibers and Selective Metal Deposition, *Proc. Natl. Acad. Sci. USA* **2003**, *100*, 4527-4532.
7. Xin H.; Woolley, A.T. DNA-Templated Nanotube Localization, *J. Am. Chem. Soc.* **2003**, *125*, 8710-8711.
8. Braun, E.; Eichen, Y.; Sivan, U.; Ben-Yoseph, G. DNA-Templated Assembly and Electrode Attachment of a Conducting Silver Wire, *Nature* **1998**, *391*, 775-778.
9. Mertig, M.; Ciacchi, L.C.; Seidel, R.; Pompe, W.; De Vita, A. DNA as a Selective Metallization Template, *Nano Lett.* **2002**, *2*, 841-844.
10. Richter, J.; Mertig, M.; Pompe, W.; Mönch, I.; Schackert, H.K. Construction of Highly Conductive Nanowires on a DNA Template, *Appl. Phys. Lett.* **2000**, *78*, 536-538.
11. Mbindyo, J.K.N.; Reiss, B.D.; Martin, B.R.; Keating, C.D.; Natan, M.J. Mallouk, T.E. DNA-Directed Assembly of Gold Nanowires on Complementary Surfaces, *Adv. Mater.* **2001**, *13*, 249-254.
12. Keren, K.; Krueger, M.; Gilad, R.; Ben-Yoseph, G.; Sivan, U.; Braun, E. Sequence-Specific Molecular Lithography on Single DNA Molecules, *Science* **2002**, *297*, 72-75.
13. Monson, C.F.; Woolley, A.T. DNA-Templated Construction of Copper Nanowires, *Nano Lett.* **2003**, *3*, 359-363.
14. Michalet, X.; Ekong, R.; Fougerousse, F.; Rousseaux, S.; Schurra, C.; Hornigold, N.; Slegtenhorst, M.; Wolfe, J.; Povey, S.; Beckmannand, J.S.; Bensimon, A. Dynamic Molecular Combing: Stretching the Whole Human Genome for High-Resolution Studies, *Science* **1997**, *277*, 1518-1523.
15. Woolley, A.T.; Kelly, R.T. Deposition and Characterization of Extended Single-Stranded DNA Molecules on Surfaces, *Nano Lett.* **2001**, *1*, 345-348.
16. Nakao, H.; Hayashi, H.; Yoshino, T.; Sugiyama, S.; Otobe, K.; Otani, T. Development of Novel Polymer-Coated Substrates for Straightening and Fixing DNA, *Nano Lett.* **2002**, *2*, 475-479.

17. Bloomfield, V.A.; Crothers, D.M.; Tinoco, I. *Physical Chemistry of Nucleic Acids*, Harper & Row: New York, **1974**, p. 421.
18. Anderson M.A.; Rubin, A.J. *Adsorption of Inorganics at Solid-Liquid Interfaces*, Ann Arbor Science: Ann Arbor, Michigan, **1981**, p. 110.
19. Altug, I.; Hair, M.L. Cation Exchange in Porous Glass, *J. Phys. Chem*. **1967**, *71*, 4260-4263.

# CHAPTER 3: DNA-TEMPLATED THREE-BRANCHED NANOSTRUCTURES FOR NANOELECTRONIC DEVICES*

## 3.1. Introduction

DNA-templated nanofabrication is an attractive approach for the self-assembly of nanoelectronics, and a number of advances have been achieved in this field [1, 2]. Double-stranded (ds) DNA has served as template for the deposition of conductive materials, including silver [3], palladium [4], copper [5], and carbon nanotubes [6, 7]. Single-stranded (ss) DNA has also been demonstrated as a template for silver metallization [8]. The electrical conductivity of dsDNA-templated nanowires has been characterized [3, 4]. Sequence-specific metallization of DNA [9, 10] has allowed the construction of a substrate-gated, DNA-templated field-effect transistor [7]. Indeed, the linear nature of DNA makes it well suited for the fabrication of two-terminal nanoelectronic devices; however, greatly increased flexibility in device design could be achieved through nonlinear, branched DNA structures. In this regard, Seeman and co-workers have provided elegant examples of the construction of complex two-dimensional arrays from DNA [2, 11], but isolated branched DNA structures for nanoelectronic devices have not been demonstrated. In this chapter, I report the use of DNA templating for the fabrication of discrete three-branched metal nanostructures as precursors for three-

* This chapter is adapted with permission from *J. Am. Chem. Soc.* **2005**, *127*, 2828-2829. Copyright 2005 American Chemical Society.

terminal nanoelectronic devices. These DNA-templated entities, along with other branched nanostructures [12], should provide a path to the construction and detailed electrical characterization of individually gated nanodevices, which are desirable in achieving electrical signal gain and independent device operation [13].

## *3.2. Experimental*

### 3.2.1. Synthetic Approach

My approach (**Fig. 3.1**) begins with the design of three oligonucleotides (**1**-**3**) that self-assemble into a three-branched motif (complex **A**). The arms of the complex have stable dsDNA portions and sticky-end overhangs to facilitate manipulation and/or extension. The core of the assembly is a ssDNA region designed to facilitate directed hybridization of a biotinylated oligonucleotide (**4**), which can be tagged with streptavidin (**5**) to give complex **B**. Oligonucleotide sequences were selected using in-house-written software that generates a ssDNA sequence and checks it for primer-dimer complexes, minimizing their length and melting temperature.

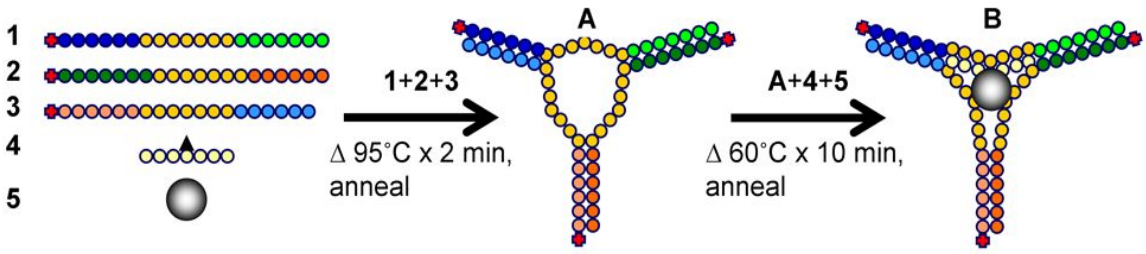


**Figure 3.1.** Assembly and specific labeling of a three-branched DNA complex. **(1-3)** long (~120 base) oligonucleotides with complementary regions represented as tonal variations of the same color (i.e., dark vs. light green). **(4)** Internally biotinylated poly-T sequence, complementary to the dark yellow regions in **(1-3)**. **(5)** Streptavidin. **(A)** Three-branched DNA nanostructure assembly. **(B)** Streptavidin-labeled, three-armed DNA complex.

### 3.2.2. Oligonucleotide Design

Oligonucleotides **1**, **2** and **3** are 125-, 125- and 118-mers, respectively; each has an extended length of ~40 nm and a melting temperature of ~74 °C. Oligonucleotide **4** is a 40-base segment with a melting temperature of ~52 °C and a biotin attached to position 20. Oligonucleotides **1**-**3** were selected and analyzed for primer-dimer complexes using software written in house. They were further analyzed for hairpins using the DNA folding and energy minimization algorithm implemented in RNAstructure [14]. The sequences of the oligonucleotides used in this work are given below. Table 1 summarizes the findings on the maximum lengths and melting temperatures ($T_m$) of the primer-dimer and hairpin complexes for oligonucleotides **1**, **2** and **3**.

**Oligonucleotide 1:**

5'GGGCGGCGACCTGCTCATCAGCTACCGGCTACCATTCGGCGCTAGAAAAAA
AAAAAAAAAAAAAAAAAAAAAAAAAAAAAAAACCGTGTCACAAGGTGC
ATCGTAACCTCACATTGCGGGGGT3'

**Oligonucleotide 2:**

5'GGGCGGCGACCTACCCCCGCAATGTGAGGTTACGATGCACCTTGTGACACG
GAAAAAAAAAAAAAAAAAAAAAAAAAAAAAAAAAAAAAGTACAGACA
ACAGGCACGACGCACTTCTCGGAG3'

**Oligonucleotide 3:**

5'GGGCGGCGACCTCTCCGAGAAGTGCGTCGTGCCTGTTGTCTGTACAAAAAA
AAAAAAAAAAAAAAAAAAAAAAAAAAAAAAAAACTAGCGCCGAATGGTA
GCCGGTAGCTGATGAGC3'

**Oligonucleotide 4:**

5'TTTTTTTTTTTTTTTTTTTT[BioTEG]TTTTTTTTTTTTTTTTTTTT3'

**Table 3.1. Primer-dimer and Hairpin Complexes in Designed Oligonucleotide Sequences.**

| Oligonucleotide | Longest primer-dimer complex (base pairs) | Count | Maximum primer-dimer $T_m$ (°C) | Longest hairpin (base pairs) | Count | Maximum hairpin $T_m$ (°C) |
|---|---|---|---|---|---|---|
| 1 | 4 | 9 | 0.7 | 3 | 6 | -3.3 |
| 2 | 4 | 12 | 0.7 | 4 | 1 | 0.7 |
| 3 | 6 | 1 | 8.7 | 5 | 1 | 4.7 |

### 3.2.3. DNA Complex Assembly

Oligonucleotides (Qiagen, Valencia, CA) were aliquoted in Tris-EDTA (TE) buffer (pH 8.0) to a concentration of 10 nM. Equal volumes of oligonucleotides **1**, **2** and **3** were mixed with ½ volume of 10X annealing buffer (Qiagen) in a microcentrifuge tube, heated to 95 °C for 2 min and allowed to cool to room temperature. A four-fold stoichiometric excess of oligonucleotide **4**, a two-fold stoichiometric excess of streptavidin, and sufficient NaCl to provide a final concentration of 500 mM $Na^+$ were added to the tube. Then, the mixture was heated to 60 °C for 10 min and allowed to cool to room temperature.

### 3.2.4. Settings for Atomic Force Microscopy (AFM)

Data were collected with a Multimode IIIa AFM (Veeco, Sunnyvale, CA) using microfabricated, aluminum-coated silicon cantilever tips (Nanoscience Instruments, Phoenix, AZ). Vibrational noise was reduced with an active isolation system (MOD1-M, Halcyonics, Goettingen, Germany). Representative imaging parameters were: tip resonance frequency, 50-60 kHz; free oscillation amplitude, 0.9-1.1 V; amplitude

setpoint, 0.5-0.8 V; scan rate, 1.0-1.6 Hz. Images were processed offline to remove background curvature.

### 3.2.5. Preparation of Surfaces for Microscopy Analysis

Freshly cleaved mica surfaces were treated with a 1 ppm aqueous solution of poly-L-lysine (Ted Pella, Redding, CA) for 10 min, rinsed with water and air dried. Carbon-coated copper TEM grids were treated with 5 ppm aqueous poly-L-lysine for 10 min, rinsed with water and dried. Complexes **A** and **B** were deposited on both types of surfaces immediately after drying.

### 3.2.6. Metallization of DNA Complexes

Poly-L-lysine treated carbon-coated copper TEM grids were incubated with 5 μL of complex **A** for 3 hr and rinsed. Silver metallization involved treating the grids in the dark for 10 min with an ethanolic solution of $AgNO_3$ (Fisher Scientific, Fair Lawn, NJ) made basic with $NH_3$ (EM Science, Gibbstown, NJ). The grids were rinsed and exposed to a dilute aqueous formaldehyde solution (37%, Fisher) for 3-20 min. The reaction was terminated by extensive rinsing and air drying. Copper metallization required incubating the grids with a 1 M solution of $Cu(NO_3)_2$ (Mallinckrodt Baker, Paris, KY) in dimethyl sulfoxide (EM Science) for 10 min. The grids were rinsed and the DNA-associated copper ions were reduced utilizing a 1 M aqueous solution of ascorbic acid (Sigma, St. Louis, MO) for 4 min. The reaction was terminated by rinsing.

### 3.2.7. Settings for Electron Microscopy

TEM images were obtained using a Tecnai 30 FEI instrument, with 300 kV acceleration potential and 3.8 kV extraction voltage. Scanning transmission electron

microscopy (STEM) images were recorded on a Tecnai 20 Analytical FEI instrument, with 200 kV acceleration potential and 3.4 kV extraction voltage.

## *3.3. Results and Discussion*

### 3.3.1. Assembly of Branched DNA Complexes

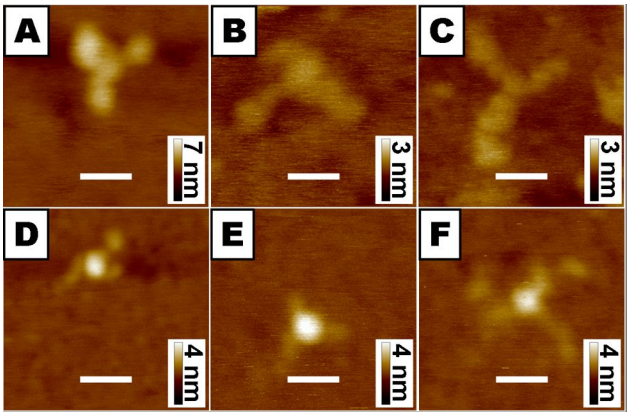


**Figure 3.2.** Tapping mode AFM height images of **(A-C)** structure **A** and **(D-F)** structure **B** on mica surfaces. The presence of a globular raised region at the center of each complex **B** is evident. The white bar represents 25 nm in all images.

Oligonucleotide reaction mixtures were deposited on mica surfaces and imaged by AFM. **Fig. 3.2A-C** shows representative images of discrete and well-defined three-branched DNA structures (**A** in **Fig. 3.1**). Substrates having the streptavidin-tagged three-armed assemblies provided AFM data (**Fig. 3.2D-F**) consistent with complex **B** in **Fig. 3.1**. The expected arm length in structures **A** and **B** was ~21 nm; the mean arm length in 40 complexes was 26 nm with a standard deviation of 5 nm. The slightly greater AFM lengths are likely due to tip convolution. Importantly, the ability to (1) assemble these complexes in solution with potentially high yields (~50%) and (2) specifically localize nanostructures using straightforward biotin streptavidin chemistry should be valuable for the bottom-up self-assembly of materials that could potentially form nanoelectronic devices.

### 3.3.2. Metallization of Branched DNA Templates

Depositing conductive material around nucleic acids is an essential step in the production of DNA-templated nanoelectronic devices. In this work, I demonstrate highly

specific metallization of branched DNA complexes using both silver [3,8] and copper [5,8]. **Fig. 3.3A-D** displays transmission electron microscopy (TEM) images of complex **A** after silver metallization, in comparison to a silver-metallized control substrate that lacked DNA (**Fig. 3.3E**). The seeding and templating effect that the DNA exerts on the deposition of silver is manifested clearly. On the DNA-containing surfaces, the shape of the metallized features resembled DNA complex **A**, whereas control surfaces only showed much larger silver deposits with irregular shapes.

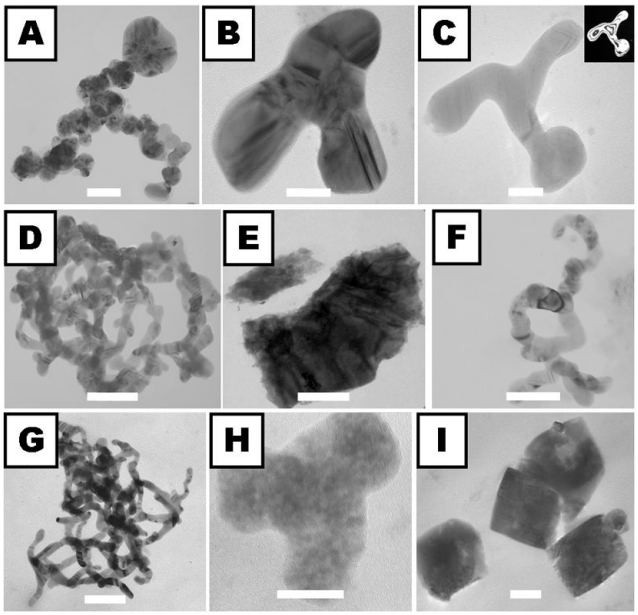


**Figure 3.3.** TEM images of DNA-templated metallization of complex **A** with silver **(A-E)** or copper **(F-I)**, on carbon-coated TEM grids. **(A)** Polycrystalline structure with multiple grains that extend well beyond the DNA template. Scale bar is 50 nm. **(B-C)** Nearly single-crystalline metallized complexes with dimensions closer to those of the DNA template show fewer crystal defects and grain boundaries. Scale bars are 25 nm. **(C)** Inset is a dark-field TEM image. **(D)** Higher-order cluster of DNA-templated silver nanostructures showing multiple filamentous features that branch at regular intervals. The white bar depicts 100 nm. **(E)** Micron-scale silver crystals with irregular features on a control grid containing no DNA. Scale bar is 2 μm. **(F)** Lower- and **(G)** higher-order clusters of crystalline DNA-templated copper metallization products. Scale bars are 50 and 100 nm, respectively. **(H)** More abundant, three-branched polycrystalline copper nanostructures. Scale bar is 25 nm. **(I)** Control experiments on surfaces lacking DNA complexes show large copper crystals. Scale bar is 100 nm.

Furthermore, I found that the pH of the reducing solution influenced the degree of polycrystallinity of the metallized complexes. At higher reducing solution pH (8-12),

primarily polycrystalline silver nanostructures were formed (**Fig. 3.3A**), while at lower reducing solution pH (2-6), DNA-templated silver products were more single crystalline (**Fig. 3.3B,C**). Indeed, dark-field TEM images of complex **A** metallized with reducing solutions at lower pH values indicate the nearly single-crystalline nature of some of the resulting structures (**Fig. 3.3C**, inset). The substrate also influenced the morphology of the DNA templates, which sometimes formed higher-order clusters on hydrophobic TEM grids, compared to primarily isolated three-branched complexes on mica. When these clusters were metallized, they formed seemingly interwoven bundles of DNA-templated silver branching at regular intervals, as shown in **Fig. 3.3D**. Preferential axial extension of branches (e.g., **Fig. 3.3C**) may be due to the deposition kinetics for the different crystalline planes, although further studies will be needed to elaborate the mechanism more fully.

Metallization of three-branched DNA assemblies with copper was also highly specific. Complex **A** was formed and deposited on TEM grids, and then metallized with copper [15]. TEM analysis revealed clear differences between copper-metallized surfaces containing DNA templates (**Fig. 3.3F-H**) and metallized control substrates lacking DNA templates (**Fig. 3.3I**). A few clusters of more highly crystalline, branched copper nanostructures were identifiable (**Fig.3.3F,G**), but more commonly, I observed polycrystalline metallization of individual DNA complexes (**Fig. 3.3H**). Metallization under milder conditions should favor the formation of structures whose features are more single crystalline, as I have observed for silver. I have also characterized metallization products of complex **B**, but the thickness of metal deposition necessary for TEM analysis obscures the low-contrast streptavidin core.

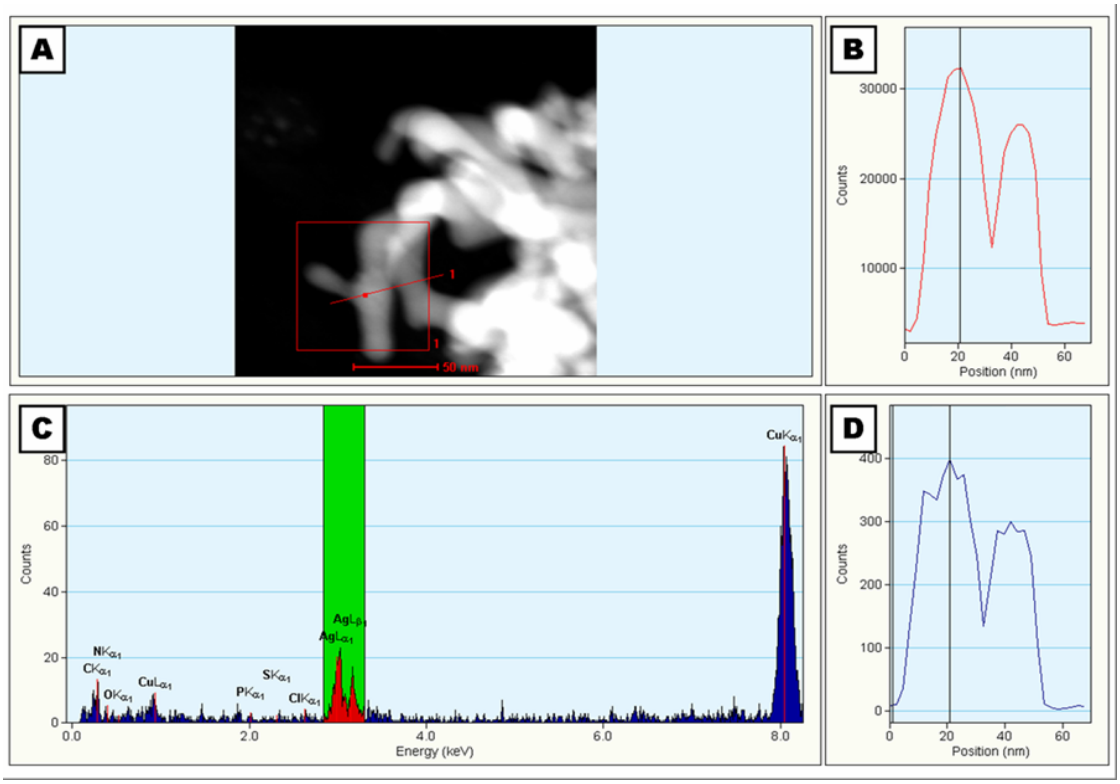


**Figure 3.4.** STEM EDX line profile on a drift-corrected region of a cluster of silver-metallized three-branched DNAs. **(A)** STEM image, showing the analyzed feature, the region used for Fourier transform drift correction (red box) and the path of the line scan (red line). The small dot along the red line represents a spot in the image, which is analyzed in **(B-D)**. **(B)** Raw trace of the high-angle annular dark-field detector along the line scan. The black vertical line indicates the position of the dot in **(A)**. **(C)** X-ray spectrum for the position marked by the dot in **(A)**. Silver, carbon and copper (from the grid) are the main constituents. The green region encompasses the $Ag_L$ X-rays. **(D)** Integration of the green region in **(C)** shows a silver content profile that closely resembles that of the total signal in **(B)** and is in full registry with the image in **(A)**.

Nanometer-resolution energy-dispersive X-ray (EDX) studies on metallized nanostructures were carried out with a STEM. On silver-metallized DNA templates, $Ag_L$ X-rays were the most intense of the bands not arising from the grid, revealing that the studied clusters were mainly composed of silver (**Fig. 3.4**). Moreover, EDX analysis of copper-metallized complex **A** showed a $Cu_L$ peak signal strongly correlated with the morphology of the structure, indicative of DNA-templated three-branched copper deposits.

## 3.4. Conclusion

I have demonstrated the design, self-assembly, and specific metallization of a three-branched DNA motif that can be specifically labeled at the center using biotin-streptavidin coupling. The formation of complexes, both with and without conjugated streptavidin, has been established by AFM. Moreover, silver and copper metallization of these complexes with high specificity for the DNA template has been achieved. Electron microscopy analysis of these DNA-templated nanostructures has revealed their morphology, and high-spatial-resolution EDX of the metallized products has confirmed their composition. Rationally designed three-armed DNA complexes could potentially serve as positioning and connecting tools for streptavidin-tagged semiconductor nanocrystals or other electronically active nanomaterials, thus providing a novel means for the construction of multiple, independently operable three-terminal nanoelectronic devices. These results indicate promising potential for the use of three-branched DNA complexes in the bottom-up self-assembly of nanoelectronics.

## 3.5. References


1. Niemeyer, C.M. Progress in "Engineering Up" Nanotechnology Devices Utilizing DNA as a Construction Material, *Appl. Phys. A* **1999**, *68*, 119-124.
2. Seeman, N.C. At the Crossroads of Chemistry, Biology, and Materials Structural DNA Nanotechnology, *Chem. Biol*. **2003**, *10*, 1151-1159.
3. Braun, E.; Eichen, Y.; Sivan, U.; Ben-Yoseph, G. DNA-Templated Assembly and Electrode Attachment of a Conducting Silver Wire, *Nature* **1998**, *391*, 775-778.
4. Richter, J.; Mertig, M.; Pompe, W.; Mönch, I.; Schackert, H. K. Construction of Highly Conductive Nanowires on a DNA Template, *Appl.Phys. Lett*. **2001**, *78*, 536-538.
5. Monson, C.F.; Woolley, A.T. DNA-Templated Construction of Copper Nanowires, *Nano Lett*. **2003**, *3*, 359-363.
6. Xin, H.; Woolley, A.T. DNA-Templated Nanotube Localization, *J. Am. Chem. Soc.* **2003**, *125*, 8710-8711.
7. Keren, K.; Berman, R.S.; Buchstab, E.; Sivan, U.; Braun, E. DNA-Templated Carbon Nanotube Field-Effect Transistor, *Science* **2003**, *302*, 1380-1382.
8. Becerril, H.A.; Stoltenberg, R.M.; Monson, C.F.; Woolley, A.T. Ionic surface Masking for Low Background in Single- and Double-Stranded DNA-Templated Silver and Copper Nanorods, *J. Mater. Chem*. **2004**, *14*, 611-616.
9. Keren, K.; Krueger, M.; Gilad, R.; Ben-Yoseph, G.; Sivan, U.; Braun, E. Sequence-Specific Molecular Lithography on Single DNA Molecules. *Science* **2002**, *297*, 72-75.
10. Keren, K.; Berman, R.S.; Braun, E. Patterned DNA Metallization by Sequence-Specific Localization of a Reducing Agent, *Nano Lett*. **2004**, *4*, 323-326.
11. Seeman, N.C. DNA in a Material World, *Nature* **2003**, *421*, 427-431.
12. Mokari, T.; Rothenberg, E.; Popov, I.; Costi, R.; Banin, U. Selective Growth of Metal Tips onto Semiconductor Quantum Rods and Tetrapods, *Science* **2004**, *304*, 1787-1790.
13. Abusch-Madger, D.; Bao, Z.; Erbe, A.; Meng, H.; Zhitenev, N. In *Molecular Nanoelectronics*, 1st ed.; Reed, M. A., Lee, T., Eds.; American Scientific Publishers: Stevenson Ranch, CA, **2003**; pp 137-151.
14. Mathews, D. H.; Zucker, M.; Turner, D.H. *RNAstructure, ver. 3.7*, University of Rochester, New York, **2002**.
15. Stoltenberg, R.M.; Woolley, A.T. DNA-Templated Nanowire Fabrication, *Biomed. Microdevices* **2004**, *6*, 105-111.

# CHAPTER 4: DNA-TEMPLATED NICKEL NANOSTRUCTURES AND PROTEIN ASSEMBLIES*

## 4.1. Introduction

DNA-templated nanofabrication is a powerful approach for producing nanostructures of various materials. DNA is a robust biopolymer that can withstand a range of pH, temperature, and solvation conditions. Chelating nitrogenated bases in the DNA molecule, as well as a polyanionic phosphate backbone, provide chemical handles [1] that make possible the fabrication of DNA-templated nanomaterials. Typically, sodium or other ions associated with nucleic acids are exchanged for higher-charge density transition metal cations that can be reduced or further reacted to form DNA-templated solids. To date, this approach has been applied to make DNA-templated materials including metals such as silver [2-4], platinum [5], palladium [6], gold [7, 8], cobalt [9], and copper [10-12]; and semiconductors such as cadmium sulfide [13,14] and iron oxide [15].

DNA templating that does not rely on cation exchange is also possible. For instance, DNA has been used as a scaffold for the localization of bifunctional molecules that serve as linkers between DNA and other nanostructures [16]. Examples of this strategy include the use of polycyclic aromatic amines [17] or long-chain positively

* This chapter is adapted with permission from *Langmuir*, **2006**, *22*, 10140-10144. Copyright 2006 American Chemical Society.

charged surfactants [18] to direct the assembly of DNA and carbon nanotubes. Another approach [19] utilizes functionalized DNA oligonucleotides to assemble metal [20], streptavidin [12, 21], or streptavidin-coupled nanostructures [22]. Finally, DNA molecules can be modified covalently to direct the assembly of specific cations [23] or organic molecules [24].

Nickel nanostructures are of considerable interest because the electrical, magnetic, and catalytic properties of macroscale nickel-containing materials might also be valuable at the nanometer scale. In addition, nickel can serve as an intermediary in the assembly of histidine (His)-modified moieties. The His tag, a hexamer of the naturally occurring amino acid histidine, is utilized routinely in biochemical protocols as a molecular handle that mediates the reversible binding of labeled proteins to purification columns that contain nickel ions. Thus, it may be feasible for His-tagged proteins, as well as other His-labeled nanostructures, to be localized selectively and reversibly on nanoscale DNA-templated nickel.

Heterotrimeric GTP-binding proteins (G-proteins) are signal transducers that couple transmembrane receptors to their intracellular effectors. G-proteins are composed of $G_\alpha$, $G_\beta$, and $G_\gamma$ subunits. Upon ligand-induced conformational changes in the receptor, bound GDP is exchanged for GTP on $G_\alpha$, resulting in dissociation of GTP-bound $G_\alpha$ from the $G_{\beta\gamma}$ complex. Phosducin-like protein (PhLP) is a widely expressed binding partner of G-protein βγ subunit complexes and the cytosolic chaperonin containing TCP-1 (CCT). Recent findings show that PhLP is involved in the assembly of $G_{\beta\gamma}$ dimer subunits and may act in concert with CCT in the $G_{\beta\gamma}$ assembly process [25].

Here I describe the surface fabrication of DNA-templated nickel nanostructures, which have not been reported previously. I also show the association of His-tagged PhLP (His-PhLP) with $Ni^{2+}$-treated surface DNA and DNA-templated nickel metal. I observe that His-PhLP binds selectively and reversibly to DNA-templated nickel constructs to produce nanoscale linear protein assemblies. While other DNA-templated protein arrangements have been reported previously [21, 22, 26], these approaches utilized biotinylated DNA sequences to direct the binding of streptavidin to periodically occurring, but discrete, locations on the DNA. My methodology for nanofabricating DNA-templated protein assemblies is more general in the scope of proteins that can be deposited, requires no specially synthesized DNA, and yields high coverage of the DNA template with protein.

## *4.2. Experimental Section*

### 4.2.1. Preparation of cDNA Constructs for PhLP and His-PhLP

Wild-type human PhLP with 3'c-myc and $His_6$ epitope tags was constructed in the bacterial expression vector pET15b (Novagen, San Diego, CA) as described by Lukov et al [25]. The wild-type human PhLP-TAP fusion construct was prepared by PCR amplification of human PhLP and the C-TAP tag from pZome-1-C vector (Cellzome, Cambridge, UK) followed by ligation and insertion into bacterial expression vector pETDUET-1 (Novagen). The integrity of both constructs was confirmed by sequence analysis.

### 4.2.2. Protein Expression and Purification

Wild-type human PhLP-myc-His in the pET15b vector was transformed in *Escherichia coli* DE3 cells by heat shock and was purified using nondenaturing $Ni^{2+}$

chelate affinity chromatography [27]. Wild-type human PhLP-TAP in the pETDUET-1 vector was transformed in *E. coli* DE3 cells by heat shock and was extracted using BPER reagent (Pierce Biotechnology, Rockford, IL) followed by TAP tag purification as described by Rigaut et al [28]. The purified proteins were concentrated and exchanged into 20 mM HEPES (pH 7.2), 150 mM NaCl, 50% glycerol buffer.The concentration and purity of the proteins were determined as described by Lukov et al [25], with each protein exceeding 90% purity.

### 4.2.3. Substrate Preparation for Atomic Force Microscopy (AFM)

I used both hydrophobic and hydrophilic silicon surfaces to align DNA and generate my nanomaterials. To prepare these substrates, I cleaned 1 $cm^2$ pieces of p-type [100] silicon wafers (TTI Silicon, Sunnyvale, CA) using piranha solution, rinsed them with purified water from an Easypure UV/UF system (Barnstead, Dubuque, IA), and dried the surfaces under a stream of nitrogen. Cleaned silicon squares were used directly as hydrophilic substrates. To produce hydrophobic surfaces, I dried the cleaned silicon pieces at 130 °C for 1 h and then exposed them to chlorodimethyloctadecylsilane (Aldrich, St. Louis, MO) vapor for 5 min. I removed the wafers from the oven and soaked them in acetone for 30 min followed by rinses with acetone, 2-propanol, and purified water. In preparation for DNA alignment, I treated hydrophilic silicon squares with a 1 ppm aqueous solution of poly-L-lysine (Ted Pella, Redding, CA) for 1 min followed by a purified water rinse; hydrophobic squares were used as prepared. I aligned λ DNA (New England Biolabs, Ipswich, MA) on both types of silicon substrates by translation [29] or wicking of a 1-4 μL droplet of a 1-5 ng/μL λ DNA solution in 10 mM Tris-HCl, 1 mM EDTA (both from Life Technologies, Grand Island, NY), pH 8.0 (TE buffer). Finally, I

rinsed the aligned DNA substrates with purified water and dried them under a stream of nitrogen. Both types of surfaces allowed the fabrication of nanostructures, but the hydrophilic silicon substrates were more susceptible to nonspecific deposition of His-PhLP when rinsing was not optimal. I attribute this behavior to electrostatic interactions between the positively charged His tag and the negatively charged silicon dioxide surface.

### 4.2.4. Preparation for Scanning Transmission Electron Microscopy (STEM)

I took copper grids coated with an unsupported carbon film (Ted Pella) and treated them with a 4 μL droplet of a 5 ng/μL λ DNA solution in TE buffer for 5 min or until evaporation was complete. I then rinsed the substrates with purified water. This procedure deposited the DNA strands on the carbon surface without subjecting it to large mechanical forces that could fracture the carbon film. I found that translation of the solution to align DNA fragments on the carbon surface was unsuccessful because of the fragile nature of the unsupported carbon membranes.

### 4.2.5. Preparation of DNA-$Ni^{2+}$ Complexes and DNA-templated $Ni^0$

I prepared saturated ethanolic solutions of $NiCl_2$ (Acros Organics, Geel, Belgium) or $Ni(NO_3)_2$ (Baker & Adamson, Easton, PA) by dissolving 50 mg of either salt in 500 μL of ethanol, vigorously stirring for 10 min, and centrifuging at 14 000 rpm for 5 min. I observed no effects of the nickel salt anions on the nanostructures I fabricated. To produce $Ni^{2+}$-treated DNA, I exposed surface-aligned DNA substrates to the ethanolic nickel ion solution for 5 min in an environment saturated with ethanol vapor, after which

I rinsed abundantly with ethanol and dried the substrate under a stream of nitrogen. To make DNA-templated nickel metal, I prepared a reducing solution, dissolving 4 mg of $NaBH_4$ (EMD, Gibbstown, NJ) in a mixture of 100 μL of concentrated $NH_4OH$ and 900 μL of purified water, stirring for 5 min, and allowing the solution to sit overnight before use. I treated aligned DNA substrates with 15 μL of the saturated ethanolic nickel solution for 5 min in an enclosed chamber, added 200 μL of the reducing solution, and allowed the reaction to proceed for 5 min. Finally, the substrates were rinsed with purified water and dried under a stream of nitrogen.

### 4.2.6. Preparation of DNA–Nickel–Protein Nanocomposites

I prepared a protein dilution buffer, containing 20 mM HEPES, (Mallinckrodt Baker, Phillipsburg, NJ) pH 7.2 and 150 mM NaCl (Columbus Chemical Industries, Columbus, WI). I also prepared a nickel binding equilibration buffer, containing 20 mM Tris, pH 8.0, 500 mM NaCl, and 50 mM imidazole (Acros Organics). I prepared a solution containing 70 ng/μL His-PhLP in a 1:1 mixture of the dilution and equilibration buffers and used it within 1 h. I incubated substrates, having either $Ni^{2+}$-treated DNA or DNA-templated nickel metal, with 10 μL of the His-PhLP solution for 1 min, rinsed abundantly with purified water and dried under a gentle nitrogen stream. For control experiments, a 70 ng/μL solution of PhLP lacking the His-tag was used to treat the same type of substrates in a similar way.

### 4.2.7. Settings for AFM

I collected tapping mode height images with a Multimode IIIa AFM (Veeco, Sunnyvale, CA) using microfabricated, aluminum-coated silicon cantilever tips

(Nanoscience Instruments, Phoenix, AZ). I used an active isolation system (MOD1-M, Halcyonics, Gőttingen, Germany) to reduce vibrational noise. My imaging parameters were tip resonance frequency, 50-70 kHz; free oscillation amplitude, 0.9-1.1 V; amplitude setpoint, 0.5-0.8 V; and scan rate, 0.4-1.4 Hz. I processed my images offline to remove background curvature.

### 4.2.8. Settings for STEM

I recorded STEM images on a Tecnai 20 FEI instrument, with a 200 kV acceleration potential and a 3.4 kV extraction voltage. I used the cross-correlation method of the Tecnai software to correct for sample drift during nanometer-resolved energy-dispersive X-ray (EDX) analysis.

## *4.3. Results and Discussion*

### 4.3.1. Nickel Metallization

**Fig. 4.1** displays tapping mode AFM height data of unmodified surface-aligned λ DNA, immobilized DNA that has been ion exchanged with $Ni^{2+}$, and DNA-templated nickel metal. The height of DNA increases by almost a factor of 2 after incubation with a saturated ethanolic solution of $Ni^{2+}$ followed by ethanol rinsing (**Fig. 4.1B**). This increase in DNA height persists until the substrate is rinsed with an aqueous solution, which returns the DNA height to its unmodified value. **Fig. 4.1C** shows a linear DNA-templated nickel metal nanostructure on a silicon surface, fabricated as outlined in Section 4.2.5. The morphology of these metal nanostructures, as revealed by AFM, is that of a chain of closely spaced nickel nanoparticles, with ~12 nm cross-sectional dimensions. **Fig. 4.1D** shows a completely extended λ DNA molecule that is covered continuously with such nickel nanoparticles. This image demonstrates that my method for fabrication of nickel

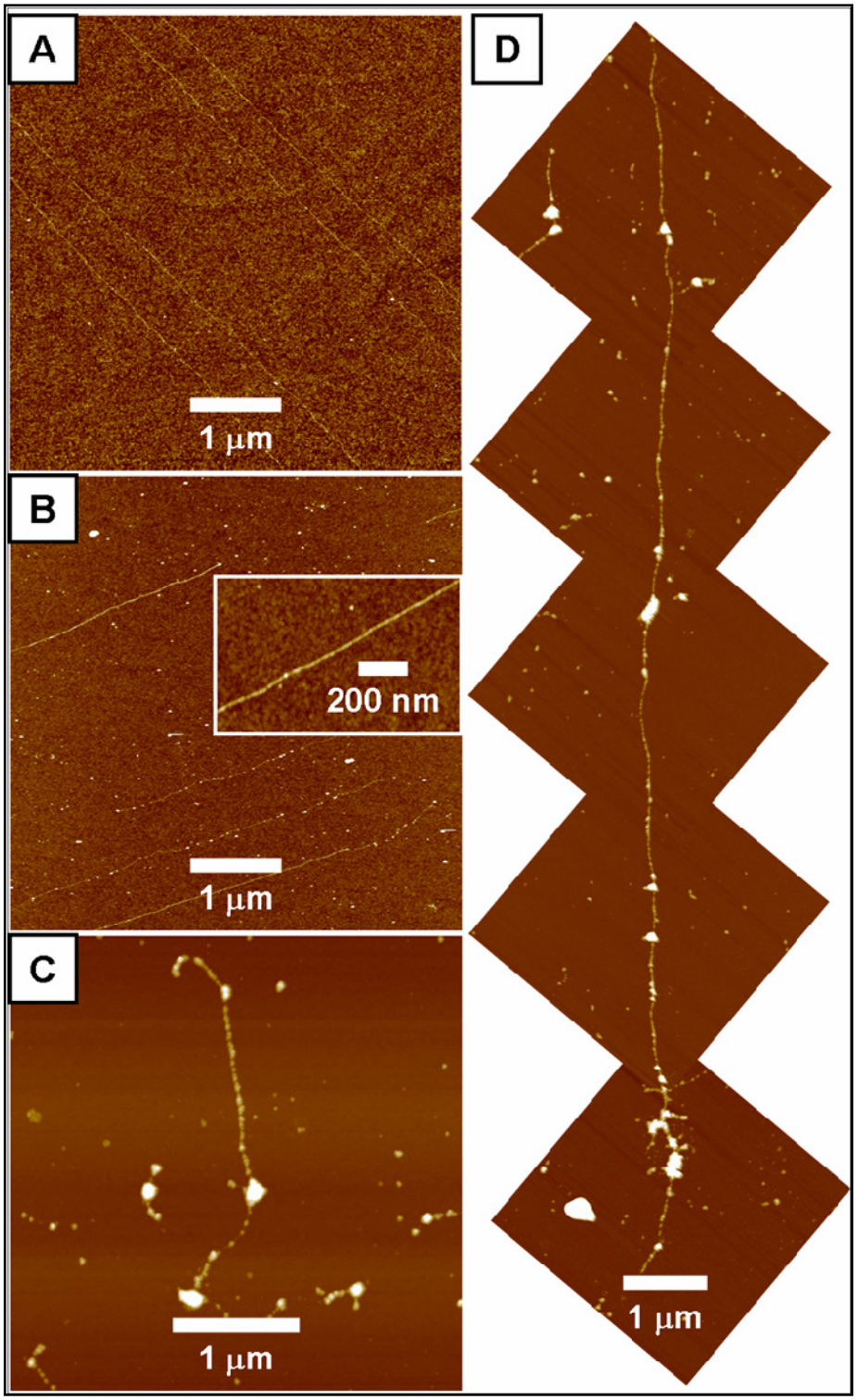


**Figure. 4.1.** Tapping mode AFM height images of the synthesis of DNA-templated nickel. **(A)** Surface-aligned λ DNA molecules; Z scale is 3 nm. **(B)** DNA treated with $Ni^{2+}$ and rinsed with ethanol; Z scale is 10 nm. **(C-D)** Linear nickel metal nanostructures made from surface DNA; Z scale is 50 nm in **(C)** and 100 nm in **(D)**.

nanostructures does not cleave or otherwise damage the DNA template, allowing long DNA molecules to be plated with nickel, without loss of their structural integrity.

Importantly, linear or two-dimensional assemblies of DNA-templated nickel nanoparticles could form ordered nanoscale magnetic storage units [9] or serve as catalytic seeds for the nanoscale patterned growth of materials such as carbon nanotubes [30, 31].

### 4.3.2. Compositional X-ray Analysis

I used analytical electron microscopy to further characterize these DNA-templated nickel structures. **Fig. 4.2A-B** shows STEM images of two separate DNA-templated nickel nanostructures grown on carbon-coated copper grids. Due to the hydrophobic nature of these surfaces, the DNA strands tend to bundle or entangle when deposited on such substrates, producing nonlinear nickel nanostructures. I found a granular but quasicontinuous assembly of nickel nanoparticles along the DNA template. The average width of the observed features in the thinner, unbundled regions is ~17 nm, which agrees well with the measured AFM height of ~12 nm. Due to the finely focused electron beam in STEM, it is possible to selectively probe well-defined, nanometer-sized regions in the sample under study.

**Fig. 4.2C** shows an EDX spectrum obtained from a region in the nickel nanostructure in **Fig. 4.2B**. The spectrum shows prominent nickel $L_\alpha$ and $K_\alpha$ peaks at 0.851 and 7.477 keV, respectively. Less intense carbon, oxygen, and silicon peaks from surface adsorption are observed, as well as copper and cobalt peaks from the supporting grid and the pole piece of the electromagnetic objective lens, respectively. I profiled the composition of the nanostructure in **Fig. 4.2B** by taking a series of EDX spectra at 5 nm

intervals along the red line. I integrated the signal from the nickel $K_\alpha$ peak in each spectrum to obtain a cross section (**Fig. 4.2D**) and compared this profile with that generated from the signal collected at the high-angle annular dark-field detector (**Fig. 4.2E**). The two plots have nearly identical shapes, indicating that the analyzed nanostructure is mainly composed of nickel.

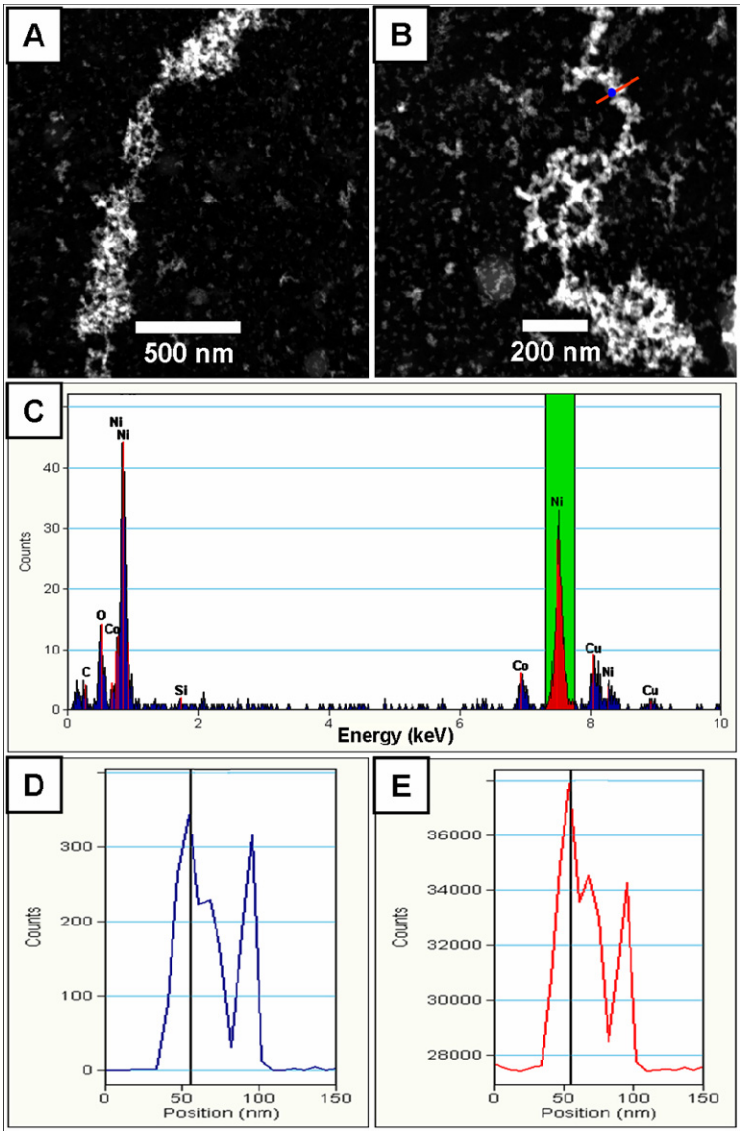


**Figure. 4.2.** STEM images and nanometer-resolved composition analysis of DNA-templated nickel metal nanostructures. **(A-B)** STEM images of DNA-templated nickel nanostructures. **(C)** EDX spectrum obtained from the location indicated by the blue dot in **(B)**. **(D)** Integration of characteristic nickel X-ray peaks (green region in **C**) from EDX spectra collected at 5 nm intervals along the red line in **(B)**. **(E)** Total signal profile at the high-angle annular dark-field detector along the same red line.

### 4.3.3. Nickel–Protein Nanocomposites

I also studied the interaction of PhLP and His-PhLP with my DNA-templated nickel assemblies. **Fig. 4.3A** shows an AFM height image of individual PhLP molecules on a surface; their average height is 4.2 nm with a standard deviation of 1.1 nm. The PhLP dimensions agree remarkably well with the 4.8 nm average diameter determined from the crystallographic structure of the closely related protein, Phosducin (PDB 2TRC) [32]. Further, I observed no difference in the AFM heights of PhLP and His-PhLP. **Fig. 4.3B** depicts a control substrate showing that unmodified DNA does not interact with PhLP under the conditions utilized in my experiments. In another control, unmodified surface DNA and His-PhLP display little specific interaction after incubation and rinsing treatments (**Fig. 4.3C**).

**Fig. 4.3D** depicts the effect of incubation of PhLP with $Ni^{2+}$-treated surface DNA; not only do the DNA and the protein remain separated but also the DNA height reverts to that of untreated DNA, an indication that the imidazole buffer may deplete exposed $Ni^{2+}$ cations from the DNA. In contrast, when I incubated $Ni^{2+}$-treated surface DNA with His-PhLP, a dramatic ~10 nm height increase was observed on all DNA features (**Fig. 4.3E-F**). The selectivity of the His-PhLP for the DNA template was high, as surrounding regions were free from nonspecific protein deposition. I found that some His-PhLP deposited in the vicinity of the surface DNA, resulting in broadened AFM features relative to the original DNA. The less-than-sharp edges on these protein lines are probably due to the diffusion of $Ni^{2+}$ from the DNA to nearby surface regions during incubation with protein; His-PhLP molecules also bind in these diffused $Ni^{2+}$ regions.

**Fig. 4.3G** shows several DNA-templated nickel metal lines that have been incubated with PhLP. Some free protein molecules are present on the surface, but the

height and overall appearance of the nickel metal nanostructures are unchanged (see **Fig. 4.1C-D**).

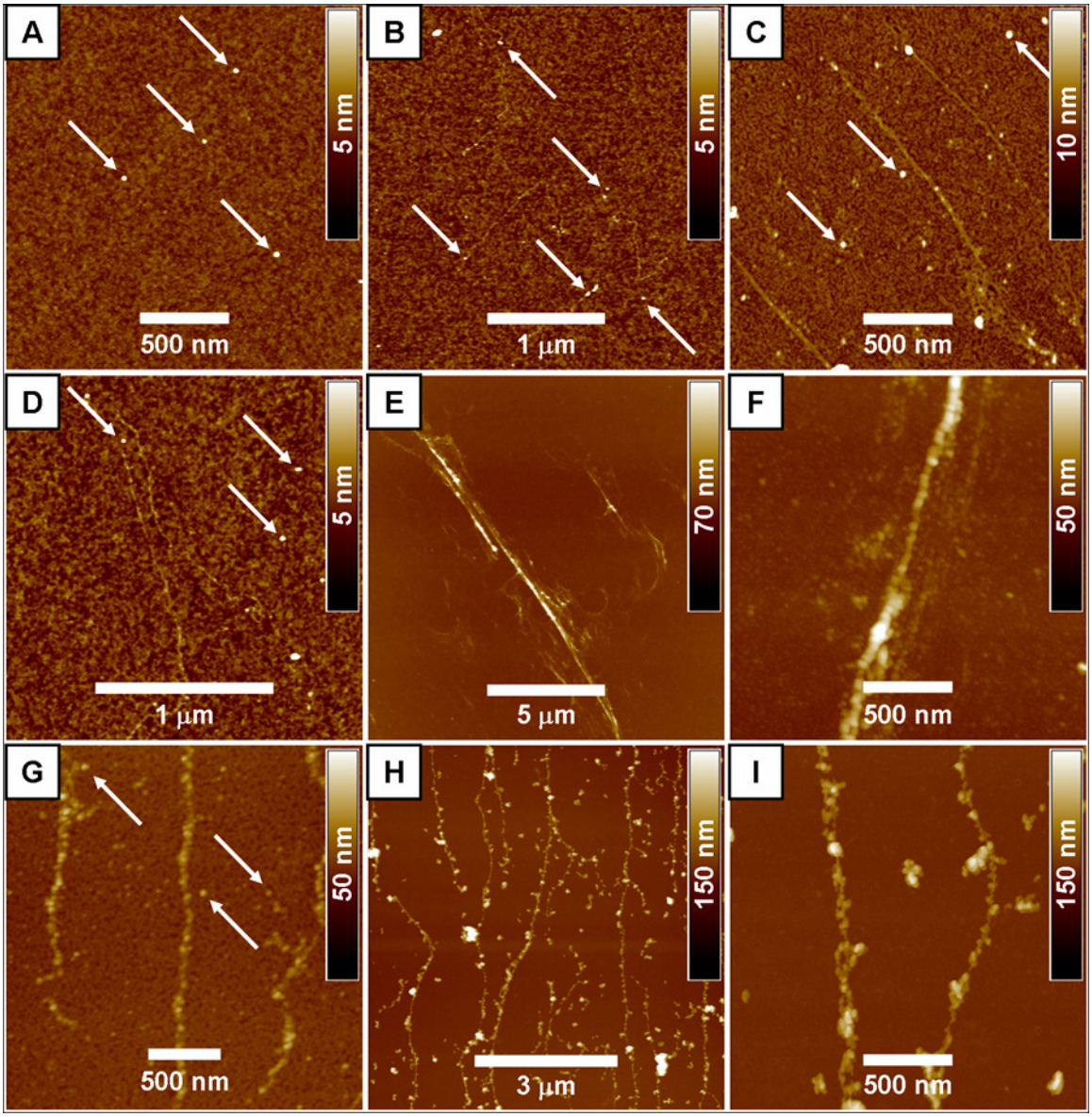


**Figure. 4.3.** AFM height images of DNA-templated nickel-protein nanocomposites. **(A)** PhLP on silicon dioxide. **(B)** DNA incubated with PhLP. **(C)** DNA incubated with His-PhLP. **(D)** DNA treated with $Ni^{2+}$, rinsed with ethanol, and exposed to PhLP. **(E-F)** DNA treated with $Ni^{2+}$, rinsed with ethanol, and exposed to His-PhLP. **(G)** DNA-templated nickel metal nanostructures exposed to PhLP. **(H-I)** DNA-templated nickel metal nanostructures exposed to His-PhLP. All substrates were rinsed with purified water after protein treatment. Individual protein molecules are indicated with white arrows in **(A-D, G)**.

On the other hand, when DNA-templated nickel metal is incubated with His-PhLP, I observe a significant, >20 nm height increase for the surface lines, as well as a

change in morphology (**Fig. 4.3H-I**). In addition, the background substrate is essentially free of nonspecific deposition of His-PhLP, and the edges of the DNA-templated nickel-His-PhLP composites are sharper than those in **Fig. 4.3E-F**. These observations can be explained by a protein localization process in which the His-PhLP selectively attacks high-energy sites along the DNA-templated nickel metal, where nickel atoms are more available for reaction. This selective attack and chelation process does not, during the short duration of the treatment, generate an excess of nickel cations that diffuse from the DNA-templated metal to neighboring areas. Thus, protein deposition along the metal nanostructure is not totally uniform, and a protein-free background is obtained.

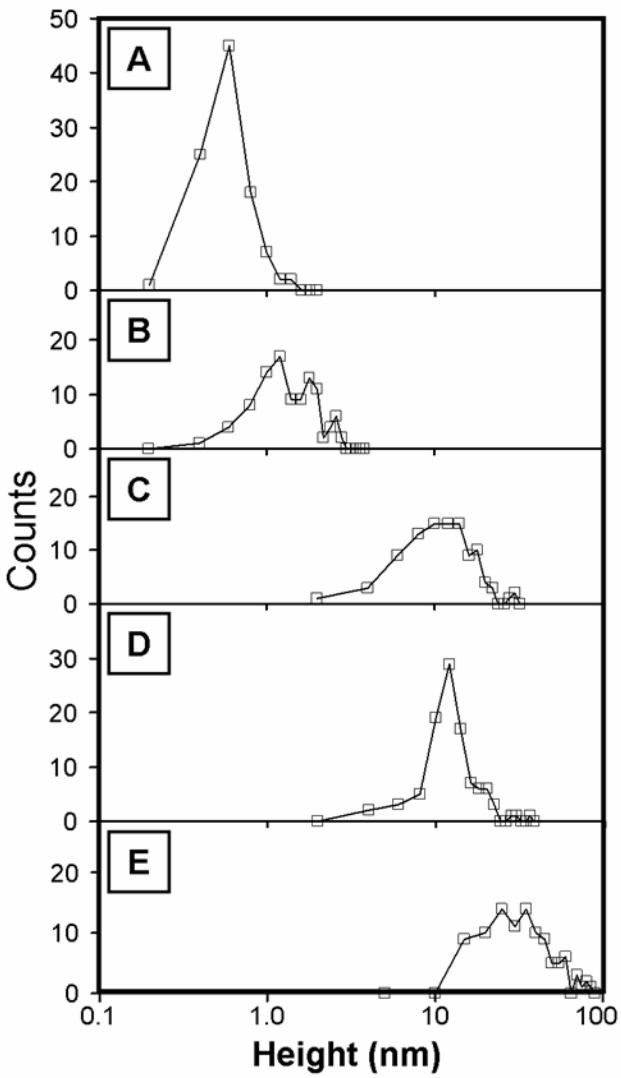


**Figure. 4.4.** Evolution of the AFM height distribution of DNA-templated materials. **(A)** Surface-aligned λ DNA. **(B)** DNA complexed with $Ni^{2+}$. **(C)** DNA complexed with $Ni^{2+}$ and treated with His-PhLP. **(D)** DNA-templated nickel metal. **(E)** DNA-templated nickel metal treated with His-PhLP. Mean heights are 0.5, 1.4, 12, 12, and 35 nm in **(A-E)**, respectively, and RSDs range from 40-47%.

**Fig. 4.4** summarizes the distributions of AFM heights for the DNA-templated nickel and protein features I made. The effects of supplying surface DNA with $Ni^{2+}$,

reducing to nickel metal, and adding His-PhLP are evident. Interestingly, I observe that $Ni^{2+}$-treated surface DNA exposed to His-PhLP undergoes a height increase that corresponds to ~2 layers of protein, while DNA-templated nickel metal appears to accommodate up to ~5 layers of His-PhLP. I believe that because the His-PhLP binding sites on the $Ni^{2+}$-treated surface DNA are abundant, closely spaced, mobile, and generally accessible, a smoothing effect is exerted that prevents locally high concentrations of His-PhLP. In contrast, for DNA-templated nickel metal, the number, accessibility, and mobility of the His-PhLP binding sites are controlled by crystallographic factors; thus, favorable facets on nickel nanoparticles may react more abundantly with His-PhLP and increase local coverage.

### 4.3.4. Reversible Nature of the Nickel–His–PhLP Interaction

Finally, I have investigated conditions that allow the straightforward removal of His-PhLP from DNA-templated nickel metal. I took DNA-templated nickel metal-His-PhLP composites, incubated them with different $Ni^{2+}$ solutions, and rinsed with purified water for 3 min. The results are summarized in **Table 4.1**; two controls (the unmodified DNA-templated nickel metal and the nickel metal-His-PhLP composite) are included for comparison.

**Table 4.1. Height of DNA-templated Nickel–His–PhLP Nanostructures upon Incubation with Different Solutions.**

| Treatment Conditions | Mean AFM Height (nm) | % RSD |
|---|---|---|
| Control 1. DNA-templated nickel metal | 12 | 40 |
| Control 2. DNA-nickel-protein nanocomposite | 35 | 47 |
| Ethanolic $Ni^{2+}$ (saturated, ~0.4 M), 15 min | 32 | 61 |
| Aqueous $Ni^{2+}$ (0.6 M), 15 min | 19 | 58 |
| Ethanolic $Ni^{2+}$ (saturated, ~0.4 M), 60 min | 18 | 31 |
| Aqueous $Ni^{2+}$ (0.6 M), 60 min | 12 | 38 |

I observe that His-PhLP largely remains localized on the DNA-templated nickel metal after a 15 min treatment with ethanolic $Ni^{2+}$ and is not removed completely even after a 1 h exposure to this solution. Interestingly, this result suggests that surfaces with multiple types of proteins might be obtained through a multistep procedure wherein new DNA is aligned on a substrate and treated with ethanolic $Ni^{2+}$ after the formation of other DNA-templated nickel metal-His-protein composites. In contrast, I determined that treatment with aqueous $Ni^{2+}$ completely removes the His-PhLP from the DNA-templated nickel, possibly by offering more abundant and favorable chelating sites for the His tag in an environment that can solvate the protein. Importantly, aqueous $Ni^{2+}$ solutions for His-tagged protein removal can dislodge the protein without damaging the underlying nickel nanostructures. On the other hand, when I utilized 0.5 M imidazole buffer, rapid removal of the His-PhLP was observed in conjunction with etching of the nickel metal, which would limit the reusability of the DNA-templated nanostructures.

## *4.4. Conclusion*

I have reported the fabrication of DNA-templated nickel metal nanostructures that could find application as patterned lines of catalytic, magnetic, or protein domains. I have also demonstrated that both surface DNA treated with $Ni^{2+}$ and DNA-templated nickel metal reversibly bind His-PhLP. On the basis of my results from the His-PhLP model system, I expect other His-tagged proteins and nanostructures to be localizable on DNA-templated nickel. This development is an important addition to the existing repertoire of DNA-templated interactions and enables the DNA-directed self-assembly of His-tagged materials. From a biochemical vantage point, my findings could be useful in the fabrication of very high-density protein assemblies that could enhance the study of

protein-protein and protein-substrate interactions. For instance, it should be feasible to use AFM to probe whether G-protein βγ subunits bind to my Ni-His-PhLP composites, which would confirm the potential for evaluating protein-protein interactions in this system. Importantly, my methodology does not require access to cleanroom equipment or to other lithographic techniques to achieve fine patterning, although my procedures are compatible with standard microfabrication methods. Indeed, the combination of my approach with top-down microscale patterning could prove advantageous in the development of applications for DNA-templated nickel and protein nanomaterials.

## 4.5. References


1. Gu, Q.; Cheng, C.; Gonela, R.; Suryanarayanan, S.; Anabathula, S.; Dai, K.; Haynie, D.T. DNA Nanowire Fabrication, *Nanotechnology* **2006**, *17*, R14-R25.
2. Braun, E.; Eichen, Y.; Sivan, U.; Ben-Yoseph, G. DNA-Templated Assembly and Electrode Attachment of a Conducting Silver Wire, *Nature* **1998**, *391*, 775-778.
3. Keren, K.; Berman, R.S.; Braun, E. Patterned DNA Metallization by Sequence-Specific Localization of a Reducing Agent, *Nano Lett*. **2004**, *4*, 323-326.
4. Becerril, H.A.; Stoltenberg, R.M.; Monson, C.F.; Woolley, A.T. Ionic Surface Masking for Low Background in Single- and Double-stranded DNA-Templated Silver and Copper Nanorods, *J. Mater. Chem.* **2004**, *14*, 611-616.
5. Ford, W.E.; Harnack, O.; Yasuda, A.; Wessels, J.M. Platinated DNA as Precursors to Templated Chains of Metal Nanoparticles, *Adv. Mater*. **2001**, *13*, 1793-1797.
6. Richter, J.; Mertig, M.; Pompe, W.; Mönch, I.; Schackert, H.K. Construction of highly conductive nanowires on a DNA template, *Appl. Phys. Lett*. **2001**, *78*, 536-538.
7. Harnack, O.; Ford, W.E.; Yasuda, A.; Wessels, J.M. Tris(hydroxymethyl)phosphine-Capped Gold Particles Templated by DNA as Nanowire Precursors, *Nano Lett*. **2002**, *2*, 919-923.
8. Keren, K.; Kreuger, M.; Gilad, R.; Ben-Yoseph, G.; Sivan, U.; Braun, E. Sequence-Specific Molecular Lithography on Single DNA Molecules, *Science* **2002**, *297*, 72-75.
9. Gu, Q.; Cheng, C.; Haynie, D.T. Cobalt Metallization of DNA: Toward Magnetic Nanowires, *Nanotechnology* **2005**, *16*, 1358-1363.
10. Monson, C.F.; Woolley, A.T. DNA-Templated Construction of Copper Nanowires, *Nano Lett*. **2003**, *3*, 359-363.
11. Stoltenberg, R.M.; Woolley, A.T. DNA-Templated Nanowire Fabrication, *Biomed. Microdevices* **2004**, *6*, 105-111.
12. Becerril, H.A.; Stoltenberg, R.M.; Wheeler, D.R.; Davis, R.C.; Harb, J.N.; Woolley, A.T. DNA-Templated Three-Branched Nanostructures for Nanoelectronic Devices, *J. Am. Chem. Soc*. **2005**, *127*, 2828-2829.
13. Coffer, J.L.; Bigham, S.R.; Li, X.; Pinizzotto, R.F.; Rho, Y.G.; Pirtle, R.M.; Pirtle, I.L. Dictation of the Shape of Mesoscale Semiconductor Nanoparticle Assemblies by Plasmid DNA, *Appl. Phys. Lett*. **1996**, *69*, 3851-3853.
14. Liang, H.; Angelini, T.E.; Braun, P.V.; Wong, G.C.L. Roles of Anionic and Cationic Template Components in Biomineralization of CdS Nanorods using Self-Assembled DNA-Membrane Complexes, *J. Am. Chem. Soc*. **2004**, *126*, 14157-14165.
15. Nyamjav, D.; Ivanisevic, A. Templates for DNA-Templated $Fe_3O_4$ Nanoparticles, *Biomaterials* **2005**, *26*, 2749-2757.
16. Ijiro, K.; Matsuo, Y.; Hashimoto, Y. DNA-Based Silver Nanowires Fabricated by Electroless Plating, *Mol. Cryst. Liq. Cryst*. **2006**, *445*, 207-211.
17. Xin, H.; Woolley, A.T. DNA-Templated Nanotube Localization, *J. Am. Chem. Soc*. **2003**, *125*, 8710-8711.

18. Xin, H.; Woolley, A.T. High-Yield DNA-Templated Assembly of Surfactant-Wrapped Carbon Nanotubes, *Nanotechnology* **2005**, *16*, 2238-2241.
19. Gothelf, K.V.; LaBean, T.H. DNA-Programmed Assembly of Nanostructures, *Org. Biomol. Chem*. **2005**, *3*, 4023-4037.
20. Csáki, A.; Maubach, G.; Born, D.; Reichert, J.; Fritzsche, W. DNA-Based Molecular Nanotechnology, *Single Mol*. **2002**, *3*, 275-280.
21. Niemeyer, C.M. The Developments of Semisynthetic DNA-Protein Conjugates, *Trends Biotechnol*. **2002**, *20*, 395-401.
22. Li, H.; Park, S.H.; Reif, J.H.; LaBean, T.H.; Yan, H. DNA-templated Self-Assembly of Protein and Nanoparticle Linear Arrays, *J. Am. Chem. Soc*. **2004**, *126*, 418-419.
23. Czlapinski, J.L.; Sheppard, T.L. Template-Directed Assembly and Characterization of Metallosalen-DNA Conjugates, *Bioconjugate Chem*. **2005**, *16*, 169-177.
24. Gothelf, K.V.; Brown, R.S. A Modular Approach to DNA-Programmed Self-Assembly of Macromolecular Nanostructures, *Chem.-Eur. J*. **2005**, *11*, 1062-1069.
25. Lukov, G.L.; Hu, T.; McLaughlin, J.N.; Hamm, H.E.; Willardson, B.M. Phosducin-Like Protein Acts as a Molecular Chaperone for G protein Beta Gamma Dimer Assembly, *EMBO J*. **2005**, *24*, 1965-1975.
26. Yan, H.; Park, S.H.; Finkelstein, G.; Reif, J.H.; LaBean, T.H. DNA-Templated Self-Assembly of Protein Arrays and Highly Conductive Nanowires, *Science* **2003**, *301*, 1882-1884.
27. Savage, J.R.; McLaughlin, J.N.; Skiba, N.P.; Hamm, H.E.; Willardson, B.M. Functional Roles of the Two Domains of Phosducin and Phosducin-Like Protein, *J. Biol. Chem.* **2000**, *275*, 30399-30407.
28. Rigaut, G.; Shevchenko, A.; Rutz, B.; Wilm, M.; Mann, M.; Séraphin, B. A. Generic Protein Purification Method for Protein Complex Characterization and Proteome Exploration, *Nat. Biotechnol*. **1999**, *17*, 1030-1032.
29. Woolley, A.T.; Kelly, R.T. Deposition and Characterization of Extended Single-Stranded DNA Molecules on Surfaces, *Nano Lett*. **2001**, *1*, 345-348.
30. Geng, J.; Li, H.; Golovko, V.B.; Shephard, D.S.; Jefferson, D.A.; Johnson, B.F. G.; Hofmann, S.; Kleinsorge, B.; Robertson, J.; Ducati, C. Nickel Formate Route to the Growth of Carbon Nanotubes, *J. Phys. Chem. B*. **2004**, *108*, 18446-18450.
31. Shi, J.; Lu, Y.F.; Tan, K.F.; Wang, X.W. Catalytical Growth of Carbon Nanotubes/Fibers From Nanocatalyst Prepared by Laser Pulverization of Nickel Sulfate, *J. Appl. Phys.* **2006**, *99*, 024312.
32. Gaudet, R.; Bohm, A.; Sigler, P.B. Crystal Structure at 2.4 Å Resolution of the Complex of Transducin βγ and Its Regulator, Phosducin, *Cell* **1996**, *87*, 577-588.

# CHAPTER 5: DNA SHADOW NANOLITHOGRAPHY

## *5.1. Introduction*

DNA is used extensively in bottom-up nanofabrication to produce discrete [1-4] or periodic nanostructures [5-8] with controlled morphology. Such nanoscale DNA patterns have been utilized as templates for the deposition of nanoparticles [7, 9-12], metals [13-19], semiconductors [20, 21], carbon nanotubes [22-24], proteins [25-28], etc. Importantly, the properties of DNA-templated constructs are directly and sometimes adversely influenced by the nucleic acid within the assembly. For example, electroless deposition of metal on DNA typically yields granular, polycrystalline nanowires [14, 29-32] because the mesoscale uniformity of the DNA molecule promotes simultaneous, multiplexed nucleation. Thus, the development of a nanofabrication methodology that can utilize nucleic acid's patterning abilities, without requiring the presence of DNA during subsequent fabrication steps, would be highly desirable. One such patterning approach was reported by Deng and Mao [33], who deposited thick metal films over DNA nanostructures on mica to create imprinted metal replicas of the DNA features with nanometer resolution. This report showed the versatility of the DNA molecule for patterning at the nanoscale.

Shadow or angled deposition is a well-known microfabrication technique used to produce features smaller than those directly achievable by optical lithography [34, 35].

Typically, a material is either deposited through a shadow mask or onto a textured surface, which serves as its own shadow mask for certain deposition directions. Common textured surfaces used for shadow deposition include self-organized crystalline facets of NaCl [36, 37], sapphire [38], semiconductors [39, 40] and substrates with microfabricated features [41]. Recently, nanoparticles [42-44], nanowires [45, 46] and carbon nanotubes [47] have also been utilized in shadow deposition to enhance nanofabrication resolution, and patterns with 50 nm dimensions or smaller can be made by shadow deposition techniques.

Here, I explore the use of aligned DNA molecular bundles to add "texture" to flat silicon <100> substrates. Because these DNA features are very thin (~2-6 nm) and structurally compact, they provide an effective nanoscale barrier to deposition. Thus, when thin metal films are vapor deposited at an appropriate angle on these DNA-bearing substrates, the DNA serves as a "nanostencil" that patterns the films. Such shadow patterns can then be transferred into the underlying substrate as trenches using mainstream microfabrication techniques such as reactive ion etching. Furthermore, I show that my DNA shadow nanolithography (DSN) process can generate straight or curved linear trenches with linewidths as narrow as 7 nm. These trenches can then template the electroless deposition of metal nanowires, or they can be closed off at the top to form nanopores.

## *5.2. Experimental Details*

### 5.2.1. DNA Alignment

I used hydrophobic silicon surfaces to favor the formation of DNA bundles. I cleaned 1 $cm^2$ pieces of p-type silicon <100> wafers (TTI Silicon, Sunnyvale, CA) using

piranha solution, rinsed them with purified water from an Easypure UV/UF system (Barnstead, Dubuque, IA) and dried them under a stream of nitrogen. I baked the substrates at 130 °C for 1 hr, and then exposed them to chlorodimethyloctadecylsilane (Aldrich, St Louis, MO) vapor for 30 min in an oven at 90 °C. I removed the wafers from the oven and soaked them in acetone for 30 min, followed by rinses with acetone, isopropanol and purified water.

I aligned λ DNA (New England Biolabs, Ipswich, MA) on the hydrophobic silicon substrates by translation [48] or wicking of a 1-4 μL droplet of a λ DNA solution in 10 mM Tris, 1 mM EDTA (both from Life Technologies, Grand Island, NY), pH 8.0. DNA concentrations of 1-5 ng/μL produced aligned individual DNA molecules, whereas DNA bundles were favored by concentrations in the 25-50 ng/μL range. Finally, I rinsed the aligned DNA substrates with purified water and dried them under a stream of nitrogen.

### 5.2.2. Atomic Force Microscopy (AFM)

I collected tapping mode height images with a Multimode IIIa AFM (Veeco, Sunnyvale, CA) using microfabricated, aluminum-coated silicon cantilever tips (Nanoscience Instruments, Phoenix, AZ). I used an active isolation system (MOD1-M, Halcyonics, Goettingen, Germany) to dampen out vibrational noise. Imaging parameters were: tip resonance frequency, 50-70 kHz; free oscillation amplitude, 0.9-1.1 V; amplitude setpoint, 0.5-0.8 V; and scan rate, 0.4-1.4 Hz. I processed my images offline to remove background curvature.

### 5.2.3. Scanning Electron Microscopy (SEM)

I recorded secondary electron SEM images using a Phillips XL30 Environmental SEM with a field emission gun. Substrates were imaged in high vacuum mode without any conductive coating.

### 5.2.4. Thermal Evaporation of Metal Films

I used a CHA-600 triple-source thermal evaporator (CHA Industries, Fremont, CA) fitted with a stationary, planar holder, which was leveled carefully. I oriented the DNA-bearing silicon squares by placing them on polymer supports cut to the appropriate angle, and placed them directly above the metal source at a ~40 cm distance. When the pressure was $<2 \times 10^{-6}$ torr, I deposited ~4 nm of either Al or Cr on the substrates at 0.5 Å/s.

### 5.2.5. Reactive Ion Etching

I used an inductively coupled plasma reactive ion etching (ICP-RIE) tool from Surface Technology Systems (Newport, UK) for transferring DNA shadows onto substrates. I etched the metal-masked silicon samples with $C_4F_8$ and $SF_6$. Typical experimental conditions are given below.

The $C_4F_8$ gas flow rate was 30-130 sccm (cubic centimeters per minute at standard temperature and pressure); the flow rate for $SF_6$ was 50 sccm. Coil power was 800 W, platen power was 200 W, and the platen was cooled to 10 °C with flowing helium. The base pressure was $\sim 2 \times 10^{-7}$ torr, and the etching pressure was ~10 mtorr. The etch time was 1-4 min.

I cleaned all my etched samples for 30 s in a 200 W, 10 sccm $O_2$ plasma (PE-II, Technics, Danville, CA) to remove any surface contamination. I verified by X-ray

photoelectron spectroscopy, AFM and SEM that this cleaning did not damage the metal films.

### 5.2.6. Oxidation of Silicon Substrates

Silicon substrates with DSN-patterned nanotrenches were oxidized inside a Lindberg/Blue M tube furnace (Asheville, NC) at 800-1100 °C for 10-120 min with $O_2$ flow of 700 sccm.

## *5.3. Results and Discussion*

**Fig. 5.1** gives an overview of the DSN process. DNA molecular objects (molecules, bundles, self-assembled networks, etc.) are aligned on a surface (see Section 5.2.1 for details), and their orientation is characterized by AFM. Then, a metal film with good substrate adhesion and small grain size (e.g., Al or Cr for Si) is vapor deposited at a shallow angle relative to the surface. The resulting film has nanometer-sized gaps corresponding to molecular shadows, and anisotropic etching transfers this pattern into the substrate in the form of trenches. Other variants of DSN could achieve pattern transfer by using the metal film as a protective layer during chemical functionalization of the exposed substrate lines, followed by suitable removal of the metal film. **Fig. 5.2** shows AFM and SEM images of DNA-bearing silicon substrates before and after DSN, using plasma etching to transfer the DNA pattern into the surface. My experiments with branching DNA bundles (**Fig. 5.2D, F**) indicate that two-dimensional patterns can be generated if the features are less than ~45° from parallel to the direction of the metal deposition.

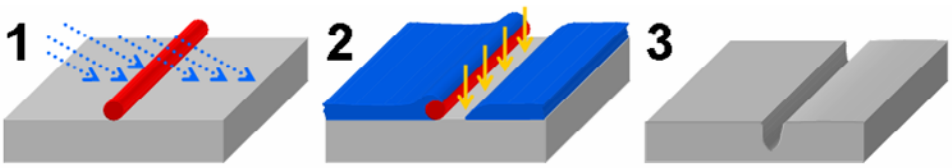


**Figure 5.1.** Overview of DNA shadow nanolithography. (**A**) Surface-aligned DNA (red) is shadowed by metal vapor (blue arrows). (**B**) A thin metal film (blue) with nanometer-scale shadow gaps is formed; then, an etching agent (gold arrows) attacks the exposed substrate. (**C**) Lift off of the metal film leaves a patterned substrate.

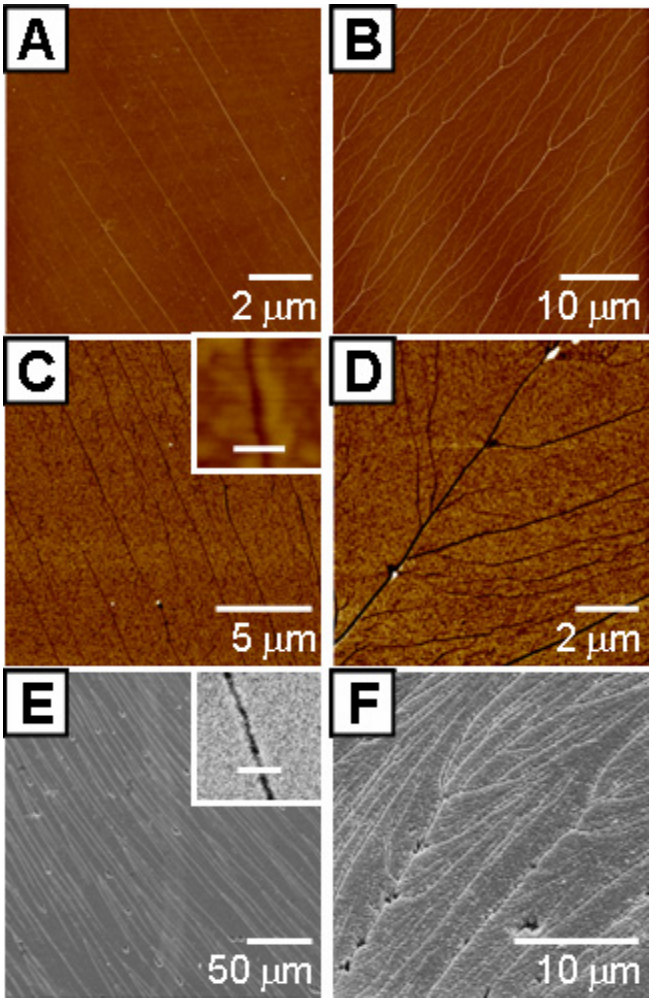


**Figure 5.2.** Transfer of linear and branched DNA patterns to silicon surfaces by DSN. AFM of surface-aligned **(A)** linear and **(B)** branched DNA bundles. AFM of a 4 nm thick **(C)** Al or **(D)** Cr film on silicon showing DNA shadows; Z scale is 10 nm for all AFM images. **(C-inset)** Close-up zoom of a trench; scale bar is 50 nm. SEM micrographs of **(E)** linear and **(F)** branched nanometer-scale trenches etched into silicon. Scale bar on the inset is 50 nm, and the trenches are ~8 nm wide.

Spatial resolution in DSN is determined by a combination of factors, including the height of the DNA template, the quality of the metal film and the nature of the pattern transfer step. To a first approximation, the width of the DNA shadow ($w$) on the metal film depends on the evaporation angle ($\theta$) as $w = h/\cos(\theta)$, where $h$ is the height of the DNA object. However, I found experimentally that the geometric model underestimates $w$ by a factor of up to 2.5 for calculated $w \leq 4$ nm. The spatial resolution limit of DSN is in part imposed by the grain size of the metal deposited, and in part by

broadening during pattern transfer to the substrate. Using Al or Cr films, I routinely observed continuous, well-defined, 7-20 nm wide molecular shadows for $\theta$ = 15-30° and $h$ = 2-4 nm. Values of $\theta$ < 15° gave wider shadows (≥ 30 nm) even for single, unbundled DNA molecules, while experiments with $\theta$ as large as 60° gave measurable, <7 nm wide shadows on occasion. Using even higher values of $\theta$ resulted in either discontinuous rows of pits 2-3 nm wide or in no discernable pattern transfer.

For successful pattern transfer by plasma etching, I found that the thickness of the metal film must be ≤ 2$h$. Thicker films perform better as etch masks and allow the creation of higher aspect ratio structures, but risk covering up finer DNA features when DNA objects of different heights are present on the surface. Trenches with aspect ratios of up to ~15 were made readily using 3 nm thick Al etch masks. Importantly, the spatial resolution and achievable depth of the etched features depend strongly on the quality of the metal etch mask. My metal films were deposited by thermal evaporation from a line source at 0.5 Å/s and base pressures <2 x $10^{-6}$ torr. Higher base pressures rendered films with numerous pinholes that resulted in poor etch masks.

Etching of DSN-patterned silicon substrates was performed in an ICP-RIE using a mixture of $C_4F_8$ and $SF_6$ as etching agents. For the same coil power and etching time (typically 3 min), higher $C_4F_8$ content gave shallower trenches with more vertical sidewalls. The sidewall profile was even more strongly influenced by $w$, the trench width at the surface (see **Table 5.1**). For $w$ < 10 nm, trenches were shallow and had rounded sidewalls (**Fig. 5.3A**), which made the bottom of the trench significantly wider than $w$. For $w$ = 10-20 nm, this rounding and broadening effect was lessened, and trench depth increased substantially (**Fig. 5.3B**).

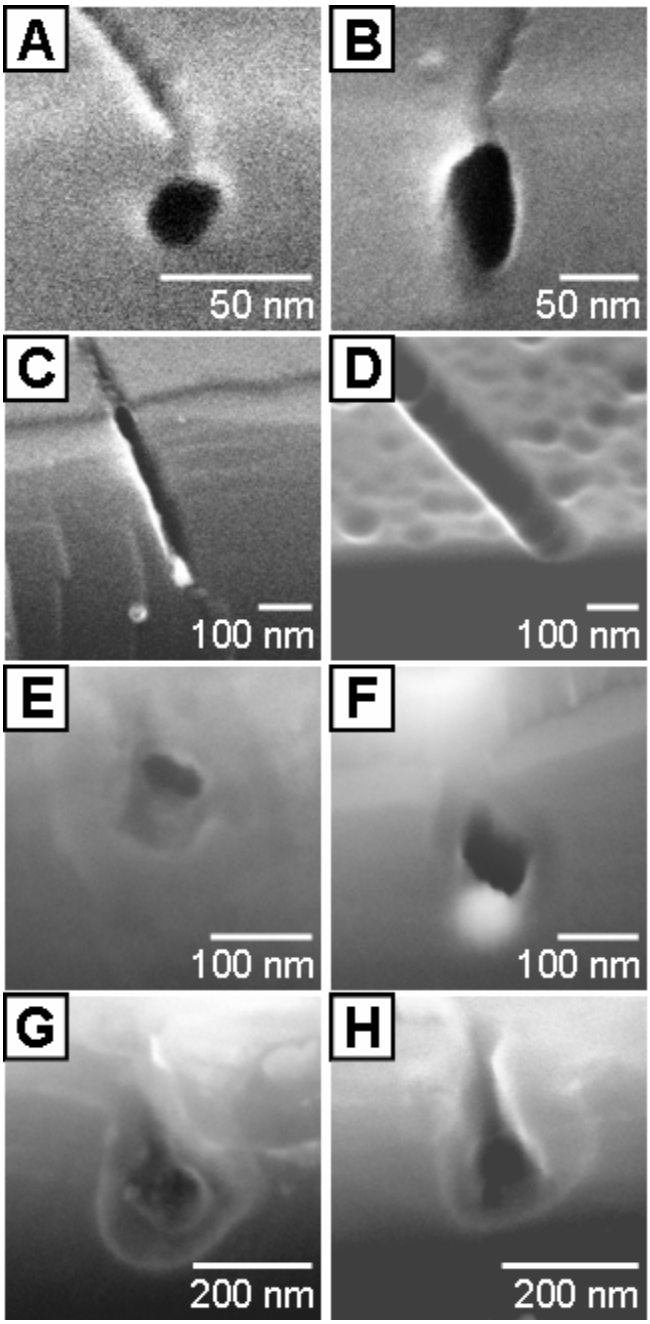


**Figure 5.3.** SEM cross-sectional profiles of etched trenches and nanopores. (**A**-**C**) Typical variation of trench depth and profile with trench width at the surface; trench dimensions are given in **Table 5.1**. (**D**) Hemispherical DNA-templated trench transferred into silica using wet etching. (**E**-**F**) Ends of nanopores formed by closing narrow-neck trenches with thermally grown silicon dioxide. (**G**) Cross-section of a nanopore showing a silica film closing the narrow top of the trench. (**H**) Cross-section of a wider, oxidized trench that failed to close into a nanopore.

For $w$ > 20 nm, sidewalls were typically straight (**Fig. 5.3C**), and trench depth approached 70% of the value obtained in control experiments with micron-scale linewidths. The observed dependence of the etch rate and the sidewall profile on trench width, as well as the constriction observed at the top of the trenches in **Fig. 5.3A-B**, is due to a reduction in the flux of ions and etching species into the trench with decreasing trench width (RIE lag) [49, 50].

I also investigated DSN on thermally oxidized silicon, using buffered oxide etchant for isotropic pattern transfer. Undercutting resulted in wider, hemicylindrical features (**Fig. 5.3D**), but these results demonstrate that DSN can be

generalized to pattern other substrates for which suitable etching is devised.

Features created by DSN can be tailored to specific applications using standard microfabrication tools. For instance, **Fig. 5.3E-F** displays end-on images of nanopores, formed through the closing of the narrow neck portion of small, rounded sidewall trenches by growth of a thin layer of dry thermal oxide. **Fig. 5.3G** shows a cleaved nanopore, with the silica layer having contrast somewhat different from the non-oxidized silicon. **Fig. 5.3H** shows a cut of a wider trench that failed to close completely due to insufficient oxide growth. Further investigation of the continuity of these DNA-templated nanopores is still required to evaluate their potential for chemical sensing [51, 52] or nanofluidics applications [53, 54].

**Table 5.1. Dimensions of DSN-fabricated Trenches Presented in Fig. 5.3A-C.**

| Panel | Top width (nm) | Maximum width (nm) | Depth (nm) |
|---|---|---|---|
| A | 7 | 22 | 40 |
| B | 15 | 43 | 110 |
| C | 27 | 43 | 385 |

In another variant of DSN, a substrate after the stage shown in **Fig. 5.1B** can be utilized to template the deposition of metal nanowires. I studied filling trenches by electroless deposition of nickel, copper or silver. Electroless silver showed the most promising results of the three metals, due to its relatively small grain size under my plating conditions. I functionalized the walls of DSN-patterned trenches in silicon with aminosilanes to activate the trenches for metal deposition, while the top of the silicon substrate was still protected by the metal etch mask. Very slow electroless deposition (typically 16 hrs) was then performed, followed by liftoff of excess plated metal through dissolution of the underlying etch mask. **Fig. 5.4A** shows a large-area SEM image of chains of 50-100 nm diameter silver nanoparticles growing out from trenches. KOH

etching of the silicon to near the level of the bottom of the trenches showed that continuous, nanocrystalline silver lines had formed (**Fig 5.4B**). However, this etching weakened the adhesion of the silver nanowires to the silicon substrate, such that many were lifted off during rinsing. In some cases, the surface of the etched substrate showed evidence of removed nanowires (**Fig. 5.4C**). Control experiments on non-templated substrates demonstrated that my electroless silver plating bath produced significantly larger deposits with different morphology from my DSN-fabricated silver lines (**Fig. 5.4D**). I expect that optimized electroless plating methods, implemented on insulating substrates, should enable the fabrication of arrays of metal nanowires through DSN.

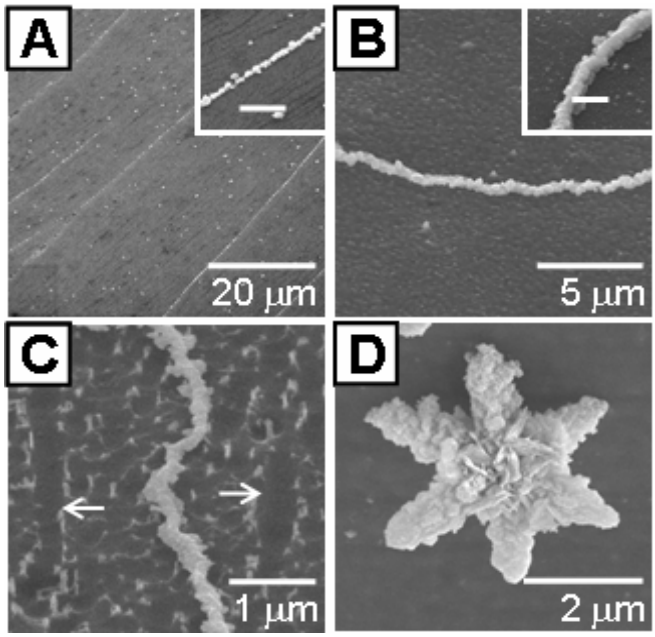


**Figure 5.4.** SEM images of electroless deposition of silver in silicon nanotrenches. (**A**) Wider trenches nucleate the growth of chains of silver nanoparticles. Narrower trenches appear as silver-free, dark lines. The white bar in the inset is 2 μm. (**B**-**C**) Etching of the top silicon layer reveals continuous silver nanowires formed inside trenches; many of these nanowires lifted off during etching and rinsing. White arrows in (**C**) point to bottom surfaces of trenches near the nanowire. Scale bar in (**B**) inset is 500 nm. (**D**) Morphology of silver deposits not templated by trenches.

## 5.4. Conclusion

I have shown the utilization of surface-aligned DNA molecules as shadow mask templates in a new nanolithography approach with spatial resolution in the sub-10-nm range. Using DSN, DNA patterns of varied complexity can be transferred to a substrate with high fidelity, and post-processed in parallel by standard chemical or microfabrication methods to add functionality to the nanofabricated structures. I have shown the formation of high-aspect-ratio trenches, enclosed nanopores and continuous metal lines on silicon by DSN. These nanostructures could find use in applications such nanofluidic channels or chemical sensors.

## 5.5. References


1. Li, X.; Yang, X.; Qi, J.; Seeman, N.C. Antiparallel DNA Double Crossover Molecules as Components for Nanoconstruction, *J. Am. Chem. Soc.* **1996**, *118*, 6131-6140.
2. LaBean, T.H.; Yan, H.; Kopatsch, J.; Liu, F.; Winfree, E.; Reif, J.H.; Seeman, N.C. Construction, Analysis, Ligation, and Self-Assembly of DNA Triple Crossover Complexes, *J. Am. Chem. Soc.* **2000**, *122*, 1848-1860.
3. Goodman, R.P.; Schaap, I.A.T.; Tardin, C.F.; Erben, C.M.; Berry, R.M.; Schmidt, C.F.; Turberfield, A.J. Rapid Chiral Assembly of Rigid DNA Building Blocks for Molecular Nanofabrication, *Science* **2005**, *310*, 1661-1665.
4. Becerril, H.A.; Stoltenberg, R.M.; Wheeler, D.R.; Davis, R.C.; Harb, J.N.; Woolley, A.T. DNA-Templated Three-Branched Nanostructures for Nanoelectronic Devices, *J. Am. Chem. Soc.* **2005**, *127*, 2828-2829.
5. Winfree, E.; Liu, F.; Wenzler, L.A.; Seeman, N.C. Design and Self-Assembly of Two-Dimensional DNA Crystals, *Nature* **1998**, *394*, 539-544.
6. Park, S.H.; Yin, P.; Liu, Y.; Reif, J.H.; LaBean, T.H.; Yan, H. Programmable DNA Self-Assemblies for Nanoscale Organization of Ligands and Proteins, *Nano Lett.* **2005**, *5*, 729-733.
7. Zhang, J.; Liu, Y.; Ke, Y.; Yan, H. Periodic Square-Like Gold Nanoparticle Arrays Templated by Self-Assembled 2D DNA Nanogrids on a Surface, *Nano Lett.* **2006**, *6*, 248-251.
8. Zheng, J.; Constantinou, P.E.; Micheel, C.; Alivisatos, A.P.; Kiehl, R.A.; Seeman, N.C. Two-Dimensional Nanoparticle Arrays Show the Organizational Power of Robust DNA Motifs, *Nano Lett.* **2006**, *6*, 1502-1504.
9. Harnack, O.; Ford, W.E.; Yasuda, A.; Wessels, J.M. Tris(Hydroxymethyl)Phosphine-Capped Gold Particles Templated by DNA as Nanowire Precursors, *Nano Lett.* **2002**, *2*, 919-923.
10. Nyamjav, D.; Ivanisevic, A. Templates for DNA-Templated $Fe_3O_4$ Nanoparticles, *Biomaterials* **2005**, *26*, 2749-2757.
11. Tanaka, S.; Fritzsche, W.; Sako, Y.; Yanagida, T. Synthesis of Long-Template DNA Using Enzymatic Reaction for Regular Alignment of Au-Nanoparticles, *Chem. Lett.* **2006**, *35*, 1290-1291.
12. Csaki, A.; Garwe, F.; Steinbrueck, A.; Maubach, G.; Festag, G.; Weise, A.; Riemann, I.; Koenig, K.; Fritzsche, W. A Parallel Approach for Subwavelength Molecular Surgery Using Gene-Specific Positioned Metal Nanoparticles as Laser Light Antennas, *Nano Lett.* **2007**, *7*, 247-253.
13. Keren, K.; Krueger, M.; Gilad, R.; Ben-Yoseph, G.; Sivan, U.; Braun, E. Sequence-Specific Molecular Lithography on Single DNA Molecules, *Science* **2002**, *297*, 72-75.
14. Braun, E.; Eichen, Y.; Sivan, U.; Ben-Yoseph, G. DNA-Templated Assembly and Electrode Attachment of a Conducting Silver Wire, *Nature* **1998**, *391*, 775-778.
15. Richter, J.; Mertig, M.; Pompe, W.; Mönch, I.; Schackert, H.K. Construction of Highly Conductive Nanowires on a DNA Template, *Appl. Phys. Lett.* **2001**, *78*, 536-538.

16. Monson, C.F.; Woolley, A.T. DNA-Templated Construction of Copper Nanowires, *Nano Lett.* **2003**, *3*, 359-363.
17. Becerril, H.A.; Stoltenberg, R.M.; Monson, C.F.; Woolley, A.T. Ionic Surface Masking for Low Background in Single- and Double-Stranded DNA-Templated Silver and Copper Nanorods, *J. Mater. Chem.* **2004**, *14*, 611-616.
18. Park, S.H.; Barish, R.; Li, H.; Reif, J.H.; Finkelstein, G.; Yan, H.; LaBean, T.H. Three-Helix Bundle DNA Tiles Self-Assemble into 2D Lattice or 1D Templates for Silver Nanowires, *Nano Lett.* **2005**, *5*, 693-696.
19. Gu, Q.; Cheng, C.; Haynie, D.T. Cobalt Metallization of DNA: Toward Magnetic Nanowires, *Nanotechnology* **2005**, *16*, 1358-1363.
20. Coffer, J.L.; Bigham, S.R.; Li, X.; Pinizzotto, R.F.; Rho, Y.G.; Pirtle, R.M.; Pirtle, I.L. Dictation of the Shape of Mesoscale Semiconductor Nanoparticle Assemblies by Plasmid DNA, *Appl. Phys. Lett.* **1996**, *69*, 3851-3853.
21. Dittmer, W.U.; Simmel, F.C. Chains of Semiconductor Nanoparticles Templated on DNA, *Appl. Phys. Lett.* **2004**, *85*, 633-635.
22. Xin, H.; Woolley, A.T. DNA-Templated Nanotube Localization, *J. Am. Chem. Soc.* **2003**, *125*, 8710-8711.
23. Keren, K.; Berman, R.S.; Buchstab, E.; Sivan, U.; Braun, E. DNA-Templated Carbon Nanotube Field-Effect Transistor, *Science* **2003**, *302*, 1380-1382.
24. Xin, H.; Woolley, A.T. High-Yield DNA-Templated Assembly of Surfactant-Wrapped Carbon Nanotubes, *Nanotechnology* **2005**, *16*, 2238-2241.
25. Niemeyer, C.M.; Adler, M.; Pignataro, B.; Lenhert, S.; Gao, S.; Chi, L.; Fuchs, H.; Blohm, D. Self-Assembly of DNA-Streptavidin Nanostructures and Their Use as Reagents in Immuno-PCR, *Nucleic Acids Res.* **1999**, *27*, 4553-4561.
26. Yan, H.; Park, S.H.; Finkelstein, G.; Reif, J.H.; LaBean, T.H. DNA-Templated Self-Assembly of Protein Arrays and Highly Conductive Nanowires, *Science* **2003**, *301*, 1882-1884.
27. Becerril, H.A.; Ludtke, P.; Willardson, B.M.; Woolley, A.T. DNA-Templated Nickel Nanostructures and Protein Assemblies, *Langmuir* **2006**, *22*, 10140-10144.
28. He, Y.; Tian, Y.; Ribbe, A.E.; Mao, C. Antibody Nanoarrays with a Pitch of ~20 Nanometers, *J. Am. Chem. Soc.* **2006**, *128*, 12664-12665.
29. Richter, J. Metallization of DNA, *Physica E* **2003**, *16*, 157-173.
30. Seidel, R.; Ciacchi, L.C.; Weigel, M.; Pompe, W.; Mertig, M. Synthesis of Platinum Cluster Chains on DNA Templates: Conditions for a Template-Controlled Cluster Growth, *J. Phys. Chem. B* **2004**, *108*, 10801-10811.
31. Ongaro, A.; Griffin, F.; Beecher, P.; Nagle, L.; Iacopino, D.; Quinn, A.; Redmond, G.; Fitzmaurice, D. DNA-Templated Assembly of Conducting Gold Nanowires between Gold Electrodes on a Silicon Oxide Substrate, *Chem. Mater.* **2005**, *17*, 1959-1964.
32. Lund, J.; Dong, J.; Deng, Z.; Mao, C.; Parviz, B.A. Electrical Conduction in 7 nm Wires Constructed on λ-DNA, *Nanotechnology* **2006**, *17*, 2752-2757.
33. Deng, Z.; Mao, C. Metallic Nanostructures: Molecular Lithography with DNA Nanostructures, *Angew. Chem. Int. Ed. Engl.* **2004**, *43*, 4068-4070.
34. Jelks, E.C.; Kerber, G.L.; Wilcox, H.A. A Simple Method for Fabricating Lines of 0.15-μm Width Using Optical Lithography, *Appl. Phys. Lett.* **1979**, *34*, 28-30.

35. Johnson, L.F.; Ingersoll, K.A.; Kammlott, G.W. An Oblique Shadow Deposition Technique for Altering the Profile of Grating Relief Patterns on Surfaces, *Appl. Phys. Lett.* **1979**, *34*, 578-580.
36. Sugawara, A.; Coyle, T.; Hembree, G.G.; Scheinfein, M.R. Self-Organized Fe Nanowire Arrays Prepared by Shadow Deposition on NaCl (110) Templates, *Appl. Phys. Lett.* **1997**, *70*, 1043-1045.
37. Kitahara, T.; Sugawara, A.; Sano, H.; Mizutani, G. Anisotropic Optical Second-Harmonic Generation from the Au Nanowire Array on the NaCl (110) Template, *Appl. Surf. Sci.* **2003**, *219*, 271-275.
38. Westphalen, A.; Zabel, H.; Theis-Bröhl, K. Magnetic Nanowires on Faceted Sapphire Surfaces, *Thin Solid Films* **2004**, *449*, 207-214.
39. Teichert, C.; Barthel, J.; Oepen, H.P.; Kirschner, J. Fabrication of Nanomagnet Arrays by Shadow Deposition on Self-Organized Semiconductor Substrates, *Appl. Phys. Lett.* **1999**, *74*, 588-590.
40. Teichert, C. Self-Organized Semiconductor Surfaces as Templates for Nanostructured Magnetic Thin Films, *Appl. Phys. A* **2003**, *76*, 653-664.
41. Jones, E.T.T.; Chyan, O.M.; Wrighton, M.S. Preparation and Characterization of Molecule-Based Transistors with a 50-Nanometer Source-Drain Separation with Use of Shadow Deposition Techniques. Toward Faster, More Sensitive Molecule-Based Devices, *J. Am. Chem. Soc.* **1987**, *109*, 5526-5528.
42. Jiang, P.; McFarland, M.J. Wafer-Scale Periodic Nanohole Arrays Templated from Two-Dimensional Nonclose-Packed Colloidal Crystals, *J. Am. Chem. Soc.* **2005**, *127*, 3710-3711.
43. Shumaker-Parry, J.S.; Rochholz, H.; Kreiter, M. Fabrication of Crescent-Shaped Optical Antennas, *Adv. Mater.* **2005**, *17*, 2131-2134.
44. Lu, Y.; Liu, G.L.; Kim, J.; Mejia, Y.X.; Lee, L.P. Nanophotonic Crescent Moon Structures with Sharp Edge for Ultrasensitive Biomolecular Detection by Local Electromagnetic Field Enhancement Effect, *Nano Lett.* **2005**, *5*, 119-124.
45. Ancona, M.G.; Kooi, S.E.; Kruppa, W.; Snow, A.W.; Foos, E.E.; Whitman, L.J.; Park, D.; Shirey, L. Patterning of Narrow Au Nanocluster Lines Using $V_2O_5$ Nanowire Masks and Ion-Beam Milling, *Nano Lett.* **2003**, *3*, 135-138.
46. Yan, X.-M.; Kwon, S.; Contreras, A.M.; Bokor, J.; Somorjai, G.A. Fabrication of Large Number Density Platinum Nanowire Arrays by Size Reduction Lithography and Nanoimprint Lithography, *Nano Lett.* **2005**, *5*, 745-748.
47. De Poortere, E.P.; Stormer, H.L.; Huang, L.M.; Wind, S.J.; O'Brien, S.; Huang, M.; Hone, J. Single-Walled Carbon Nanotubes as Shadow Masks for Nanogap Fabrication, *Appl. Phys. Lett.* **2006**, *88*, 143124.
48. Woolley, A.T.; Kelly, R.T. Deposition and Characterization of Extended Single-Stranded DNA Molecules on Surfaces, *Nano Lett.* **2001**, *1*, 345-348.
49. Lee, Y.H.; Zhou, Z.H. Feature-Size Dependence of Etch Rate in Reactive Ion Etching, *J. Electrochem. Soc.* **1991**, *138*, 2439-2445.
50. Panda, S.; Ranade, R.; Mathad, G.S. Etching High Aspect Ratio Silicon Trenches, *J. Electrochem. Soc.* **2003**, *150*, G612-G616.
51. Howorka, S.; Cheley, S.; Bayley, H. Sequence-Specific Detection of Individual DNA Strands Using Engineered Nanopores, *Nat. Biotechnol.* **2001**, *19*, 636-639.

52. Zhang, B.; Zhang, Y.; White, H.S. Steady-State Voltammetric Response of the Nanopore Electrode, *Anal. Chem.* **2006**, *78*, 477-483.
53. Pu, Q.; Yun, J.; Temkin, H.; Liu, S. Ion-Enrichment and Ion-Depletion Effect of Nanochannel Structures, *Nano Lett.* **2004**, *4*, 1099-1103.
54. Karnik, R.; Castelino, K.; Fan, R.; Yang, P.; Majumdar, A. Effects of Biological Reactions and Modifications on Conductance of Nanofluidic Channels, *Nano Lett.* **2005**, *5*, 1638-1642.

# CHAPTER 6: CONCLUSIONS AND FUTURE WORK

## *6.1. Conclusions*

### 6.1.1. Metallization of Single-stranded DNA Aligned on Surfaces and Ionic Surface Masking

Manipulation of ssDNA is challenging due to the reduced mechanical and structural stability of the molecule with respect to dsDNA. Importantly, I showed in Chapter 2 that selective deposition of silver on ssDNA templates is possible in spite of the reduced charge density of ssDNA. Indeed, metallization of ssDNA on surfaces required the use of a lower dielectric constant, ethanol-based plating bath to enhance electrostatic interactions between silver cations and the negatively charged phosphate backbone of the ssDNA. As a side effect, electrostatic interactions between the negatively charged silica surface and the silver cations were also enhanced, leading to a significant increase in non-DNA-templated metal deposits. I solved this problem by pretreating substrates with an aqueous solution of cesium cations, which have high affinity for siliceous surfaces. Cesium ions saturated surface adsorption sites, and were not displaced during the ethanolic silver treatment and reduction. This ionic-masking strategy led to ~70% reductions in the surface density and size of non-specific silver deposits, while ssDNA-templates still plated.

I further evaluated the effectiveness of ionic surface masking in the fabrication of dsDNA-templated copper nanorods on silica surfaces using non-aqueous, low-dielectric

constant plating solutions. Pretreatment of the substrates with potassium cations from aqueous solutions proved effective in blocking access to the surface and significantly reduced the density (~50% of the unmasked value) of non-specific copper deposits, without affecting DNA-templated copper deposition.

The simplicity and effectiveness of the ionic masking technique in reducing non-specific deposition without significantly affecting DNA-templated plating are remarkable, as is the fact that the ionic mask does not deteriorate the surface or complicate AFM characterization. In fact, ionic masks can be removed easily by rinsing with purified water. Importantly, non-specific deposition during DNA plating has been observed by many groups, and ionic masking could be used to alleviate this problem. Indeed, ionic masking could potentially be utilized to reduce non-templated deposition during fabrication of a wide range of DNA-templated nanomaterials on charged surfaces.

### 6.1.2. Assembly, Protein Labeling and Metallization of Branched DNA Templates

In Chapter 3 I designed a self-assembling DNA junction with three arms. The junction was constructed from three ~120-base-long synthetic DNA oligonucleotides and was assembled in solution using a slow annealing step. Each arm comprised a 40-base-pair dsDNA segment that ended in a 12-base, 5' sticky-end overhang designed to enable ligation to λ-DNA for construct elongation. The arms of the self-assembled construct were joined by a flexible central region composed of three poly-A chains. This ssDNA core region was designed to allow hybridization of a complementary poly-T sequence bearing a biotin moiety. Hybridization of these biotinylated oligonucleotides to the branched construct followed by exposure to streptavidin molecules should result in specific labeling of the DNA nanostructure with a single streptavidin. In Chapter 3 I also

showed TEM and EDX studies of the plating of branched DNA templates with silver and copper. Metallization was selective to the DNA construct and showed good coverage of both the dsDNA and ssDNA portions. The crystallinity of these deposits was influenced by the aggressiveness of the plating solution, with milder baths producing material that approached a single-crystal structure.

This work demonstrates the potential of DNA self-assembly to template the fabrication of composite nanostructures that could form scaffolds for three-terminal transistors incorporating streptavidin-coupled semiconductor nanocrystals at the center of the DNA junction. Such constructs could then be plated selectively to produce independently gateable nanoelectronic devices.

### 6.1.3. Synthesis of DNA-templated Nickel Nanorods and Coupling of Histidine-tagged Proteins to DNA-templated Nickel Materials

In Chapter 4, I developed a facile procedure for the growth of chains of nickel nanoparticles on surface-aligned DNA molecules. The procedure begins with incubation of the surface DNA with a saturated ethanolic solution of nickel cations, followed by reduction with base-stabilized sodium borohydride. I used AFM, STEM and EDX to characterize the synthesized nanomaterials. Such nickel nanostructures may find application as nanopatterned catalysts or magnets.

During the synthesis of DNA-templated nickel nanomaterials I noted that surface DNA incubated with $Ni^{2+}$ was able to retain these ions after repeated ethanolic rinses. I tested the effectiveness of DNA-templated nickel nanoparticles and $Ni^{2+}$-treated DNA as templates for the selective binding of His-PhLP. I found that both DNA-nickel materials were able to retain His-PhLP, creating DNA–metal–protein composites. These

assemblies showed good stability toward rinsing with ethanol, water, and saturated ethanolic solutions of $Ni^{2+}$. However, proteins desorbed quickly from DNA-templated nickel materials when rinsed with concentrated (~0.6 M) aqueous solutions of $Ni^{2+}$. In control experiments, I found that the histidine tag is required for selective protein adsorption onto the nickel nanomaterials.

These experiments demonstrated an interesting application to nanofabrication of the well-known purification procedure for histidine-tagged proteins using nickel-containing chromatography columns. The localization of histidine-tagged proteins on DNA-templated nickel materials was reversible at the nanoscale, using buffers and conditions similar to those for macroscale chromatographic purification. My procedure should offer a general tool to provide patterning of histidine-tagged proteins or nanostructures using DNA-templated nanofabrication.

### 6.1.4. DNA Shadow Nanolithography

Sacrificial nanofabrication templates provide a rapid, high-resolution and parallel way of patterning nanostructures. Such templates are often crystalline solids or mesoporous materials. In Chapter 5, I demonstrated the use of single DNA molecules as sacrificial nanofabrication templates. Aligned DNA molecules on silicon surfaces have a ~3 nm thick metal film deposited at a grazing angle. The surface DNA molecules serve as a shadow mask that patterns the metal film with <10 nm linewidths. These DNA shadow lines offer access to the underlying material for chemical modification or etching. Indeed, DNA shadow patterns can be post-processed using mainstream microfabrication techniques to etch the nucleic acid shadows into the substrate, deposit metals in the etched trenches, or grow silicon dioxide layers on the DSN-fabricated substrates.

DNA shadow nanolithography is a new concept that combines bottom-up and top-down fabrication to achieve nanometer-resolution patterning. This development could extend DNA-templated nanofabrication to a variety of materials that do not have affinity for DNA or that are deposited under conditions that would destroy DNA templates (e.g., chemical vapor deposition). Such DNA shadow fabricated nanomaterials could offer improved mechanical, optical or electrical properties compared with structures formed directly on DNA templates.

## *6.2. Future Directions for DNA-templated Nanofabrication*

### 6.2.1. Synthetic Refinements for Improved Material Performance

Future DNA-templated nanomaterials would benefit from synthetic refinements that expand the range of substances that can be assembled on the nucleic acid and improve the performance of the templated constructs. Possible synthetic goals include: (1) controlling the crystallinity of the DNA-templated deposits; (2) reducing defect density; (3) avoiding coprecipitates; and (4) creating well-defined interfaces through surface capping. For example, performing DNA-templated synthesis in the presence of coordinating ligands could produce highly crystalline deposits [1, 2] (**Fig. 6.1A**), and the defect density of these materials could be reduced by lattice reformation through repeated solid-phase cation exchange [3, 4] (**Fig. 6.1B**). Additionally, coordinating ligands could passivate the surfaces of the final assemblies to produce nanostructures with high charge carrier mobilities that could find application in electronics and chemical sensing [5, 6]. Thus, the incorporation of synthetic strategies from inorganic and colloidal chemistry in the preparation of DNA-templated nanomaterials could help alleviate some of the limitations of often-used electroless plating techniques and may provide a way to produce

nanostructures with tunable properties through longitudinal or transverse modulation of the composition of synthesized DNA-templated nanomaterials [7, 8] (**Fig. 6.1C-D**).

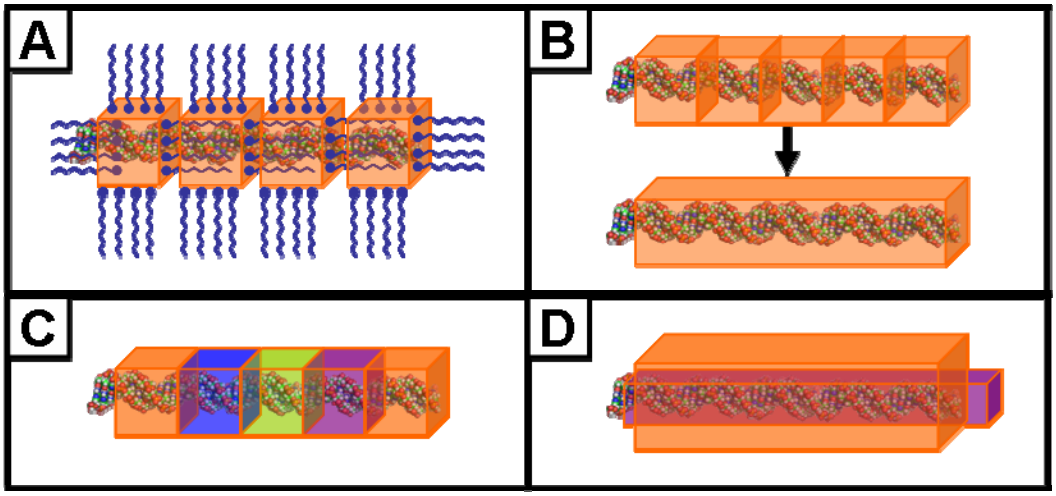


**Figure 6.1**. Highly crystalline DNA-templated nanomaterials. **(A)** Use of coordinating ligands (blue) may favor crystalline growth on DNA templates. **(B)** Solid-solid transformations through cation exchange may reduce the number of grain boudaries and other defects in DNA-templated nanomaterials. **(C)** Longitudinal and **(D)** tranverse modulation of composition in DNA-templated nanostructures (ligands are not shown for clarity in **B-D**).

### 6.2.2. Templates with Increased Complexity

DNA-templated nanofabrication gains attractiveness as the spatial intricacy of the assemblies increases, because complex templates can define hierarchical relationships between distinct nanofabricated elements. Specifically, self-assembled DNA lattices [9, 10], including those containing metal and semiconductor nanoparticles [11, 12], offer intriguing possibilities as DNA templates for the deposition of specific nanomaterials that may impart useful properties to the final construct. For example, DNA-functionalized semiconductor nanoparticles [13, 14] could be used to decorate DNA lattices, and the DNA in these nanostructured composites could then be coated with noble metals to form electrically conductive paths between the semiconductor crystals, forming DNA-templated photodetectors (**Fig. 6.2**).

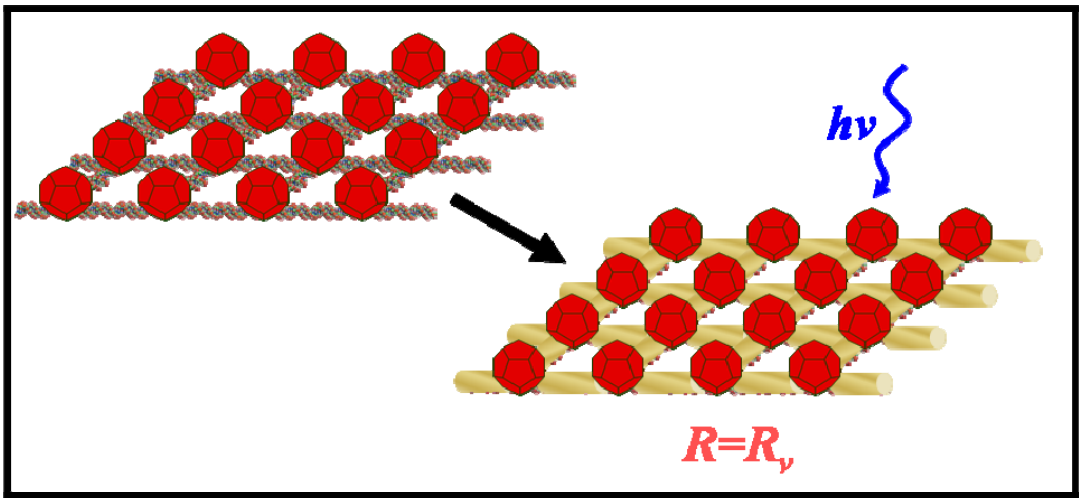


**Figure 6.2.** Metallization of a DNA lattice decorated with semiconductor nanocrystals. DNA-templated metal nanowires form electrically conductive paths that connect all the nanocrystals in the lattice. The final construct could be applied as a nanostructured photosensor.

In another potential application scenario, DNA and nanoparticles of distinct natures (metallic, semiconductive and insulating) could be combined in solution [15-17] to assemble precursors to simple nanoelectronic devices (**Fig 6.3A**). Each type of construct would have unique triplex-forming, sticky-ends for hybridizing the nanostructure in a particular orientation at complementary locations on a rigid DNA lattice, thus achieving self-assembly of multicomponent DNA-templated scaffolds for electronic circuits (**Fig 6.3B-C**) which could be made functional by metallization of the DNA.

Additionally, self-assembled DNA patterns in DNA shadow nanolithography could be useful for the formation and transfer of arbitrary shapes into surfaces with nanometer resolution over several length scales. This would be applicable for patterning silicon or other materials with networks of nanofluidic channels for chemical analysis or carrying out fundamental studies of analyte transport in nanoscale-diameter conduits.

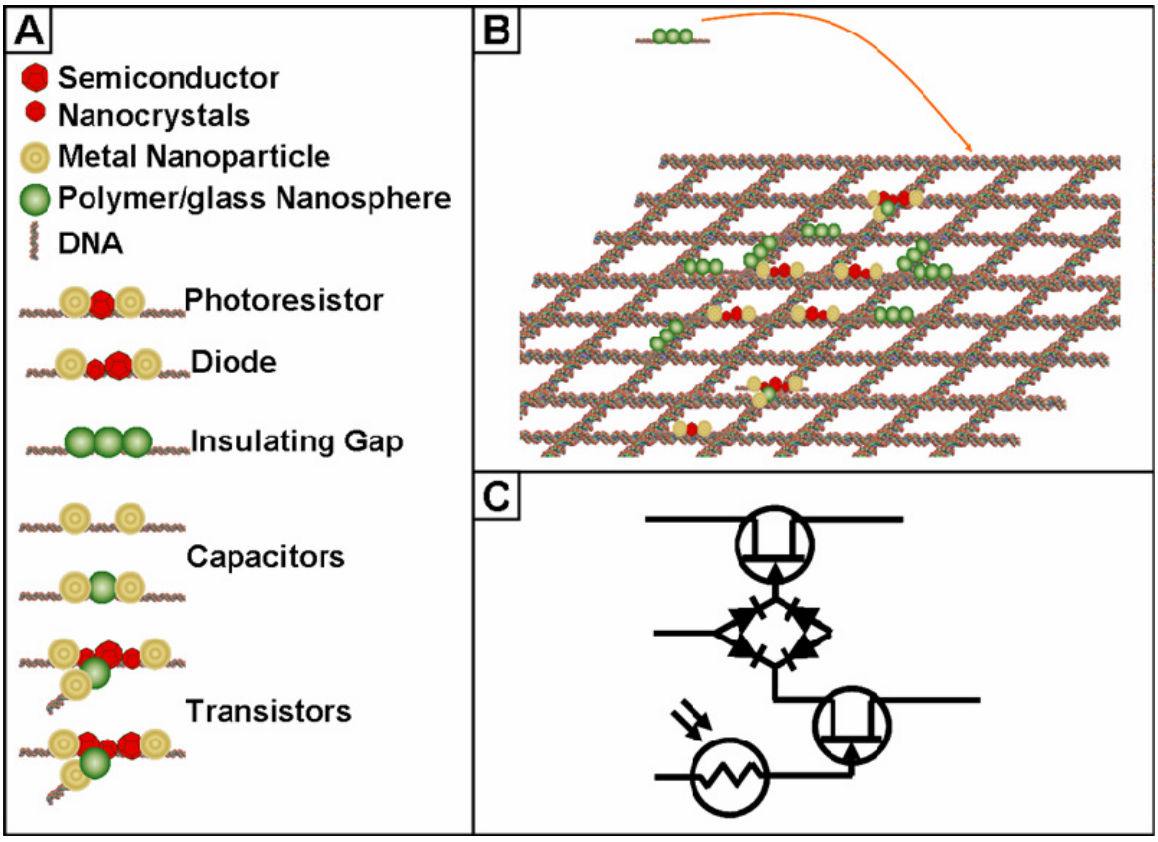


**Figure 6.3.** DNA-templated electronic circuits. **(A)** DNA-assembled, nanoparticle-based electronic components. **(B)** Partial assembly of an electronic circuit on a DNA scaffold. **(C)** Equivalent circuit after complete assembly and DNA metallization.

Template complexity could also be enhanced by the introduction of chemical handles on DNA for the synthesis of improved materials, the use of synthetic DNA with modified nucleotides, or the derivatization of nucleotides in natural DNA molecules. Examples of functionality that could be introduced in this way to dsDNA include: (1) enhanced chelating agents for metal precursors; (2) reducing agents; (3) non-plating regions; (4) specific surface anchor sites; (5) branching points; (6) coupling agents for proteins, nanoparticles, carbon nanotubes, etc.; (7) polymer initiators; (8) groups that promote controlled DNA bundling; and (9) regions with modified stiffness. Imparting these functionalities to DNA molecules would advance the field of DNA-templated nanomaterials and expand the types of functional nanodevices that can be fabricated. For

example, Braun's group demonstrated a working field-effect transistor [18] through the sequence-specific functionalization [19, 20] of DNA using items 2, 3 and 6 from the list above. An intriguing possibility for the introduction of other listed functionalities is the sequence-specific localization of property-enhancing agents on a DNA molecule through triplex forming oligonucleotides (TFOs) [21, 22]. For instance, strong chelators such as EDTA could be linked covalently to a TFO to provide enhanced metal retention (item 1); a lipid-functionalized TFO could define non-plating regions (item 3) and carbon nanotubes end-functionalized with TFO's could hybridize with a DNA scaffold at places where mechanical stability is required (item 9).

### 6.2.3. Controlled Placement of DNA Templates

Another issue that requires attention in DNA-templated nanofabrication is the controlled localization and orientation of multiple DNA templates on surfaces. Reproducible positioning of DNA molecules and patterns over large surface areas would enable the construction of rationally designed devices and systems. Controlled localization of multiple DNA nanostructures on substrates could be achieved in two ways: (1) by self-organization of DNA nanostructures on chemical alignment marks previously patterned on surfaces; or (2) by transferring self-assembled DNA constructs to a pristine surface using a topographically patterned molecular stamp.

Molecular stamping using PDMS has been utilized to pattern DNA and proteins in multilayer, three-dimensional constructs [23]. Although application of the technique is straightforward, the generation of the master stamp is complex and may require lithography methods that limit the patterning resolution to ~1 μm. DNA shadow nanolithography could be utilized to pattern PDMS and other stamping materials with

nanometer-scale resolution. Such stamps could then be utilized to transfer DNA-binding molecules (e.g., poly-L-lysine, amine-terminated dendrimers, etc.) to substrates. These deposited features could guide the placement of DNA with high spatial resolution on specific locations on a substrate.

### 6.2.4. Multilevel DNA-templated Nanofabrication

A new level of nanofabrication and synthetic complexity could be reached by devising schemes for selective protection and deprotection of DNA-templated nanomaterials deposited on a substrate; for example, either activating or deactivating them for further plating. For instance, neutral proteins localized on DNA have been shown to prevent plating [20]. Thus, metallic nanostructures could be coated with masking proteins through thiol (Au, Ag, or Pd) or histidine (Ni or Cu) linkages. Additionally, DNA-templated metallic nanostructures could be passivated against plating by capping them with metal chelating molecules bearing long aliphatic chains to block cation adsorption and electroless deposition. This advance would enable repeated cycles of controlled deposition of new DNA templates and synthesis of nanomaterials, to assemble integrated systems of DNA-templated nanostructures formed from multiple materials.

## *6.3. Final Remarks*

As I have discussed in the present work, the field of DNA-templated nanomaterials is an exciting and multidisciplinary research area that has great technological potential. Although this scientific field is still in its early stages, several proof of concept experiments have demonstrated DNA's ability to pattern surfaces with nanometer resolution using nanostructures made from a variety of inorganic and biological

materials. This dissertation presents methods for the self-assembly of DNA-templated nanomaterials, including chemicals that have natural affinity for DNA such as metal cations, and also entities that by themselves cannot interact with DNA molecules, but that can associate with intermediary substances deposited on DNA, such as His-tagged PhLP on DNA-templated nickel. Furthermore, I have shown how DNA shadows can be used to pattern substrates using top-down microfabrication techniques. I have also described promising future directions for the field, which if realized would allow the use of DNA-templated nanomaterials in a variety of chemical and electronic devices. Due to the self-assembling properties of DNA-templated nanomaterials and their controllable shape, dimension and composition, I expect that in the future these nanostructures will become developed enough to allow the fabrication of multicomponent systems containing optical and chemical sensors, fluidic analyzers and self-assembled electronic processors.

## 6.4. References


1. Liang, H.; Angelini, T.E.; Braun, P.V.; Wong, G.C.L. Roles of Anionic and Cationic Template Components in Biomineralization of CdS Nanorods Using Self-Assembled DNA-Membrane Complexes, *J. Am. Chem. Soc.* **2004**, *126*, 14157-14165.
2. Yin, Y.; Alivisatos, A.P. Colloidal Nanocrystal Synthesis and the Organic-Inorganic Interface, *Nature* **2005**, *437*, 664-670.
3. Zaziski, D.; Prilliman, S.G.; Scher, E.C.; Casula, M.; Wickham, J.; Clark, S.M.; Alivisatos, A.P. Critical Size for Fracture During Solid-Solid Phase Transformations, *Nano Lett.* **2004**, *4*, 943-946.
4. Son, D.H.; Hughes, S.M.; Yin, Y.; Alivisatos, A.P. Cation Exchange Reactions in Ionic Nanocrystals, *Science* **2004**, *306*, 1009-1012.
5. Cui, Y.; Zhong, Z.H.; Wang, D.L.; Wang, W.U.; Lieber, C.M. High Performance Silicon Nanowire Field Effect Transistors, *Nano Lett.* **2003**, *3*, 149-152.
6. Haick, H.; Hurley, P.T.; Hochbaum, A.I.; Yang, P.; Lewis, N.S. Electrical Characteristics and Chemical Stability of Non-Oxidized, Methyl-Terminated Silicon Nanowires, *J. Am. Chem. Soc.* **2006**, *128*, 8990-8991.
7. Lauhon, L.J.; Gudiksen, M.S.; Wang, C.L.; Lieber, C.M. Epitaxial Core-Shell and Core-Multishell Nanowire Heterostructures, *Nature* **2002**, *420*, 57-61.
8. Yang, C.; Zhong, Z.; Lieber, C.M. Encoding Electronic Properties by Synthesis of Axial Modulation-Doped Silicon Nanowires, *Science* **2005**, *310*, 1304-1307.
9. Ding, B.; Sha, R.; Seeman, N.C. Pseudohexagonal 2D DNA Crystals from Double Crossover Cohesion, *J. Am. Chem. Soc.* **2004**, *126*, 10230-10231.
10. Park, S.H.; Pistol, C.; Ahn, S.J.; Reif, J.H.; Lebeck, A.R.; Dwyer, C.; LaBean, T.H. Finite-Size, Fully Addressable DNA Tile Lattices Formed by Hierarchical Assembly Procedures, *Angew. Chem. Int. Ed. Engl.* **2006**, *45*, 735-739.
11. Le, J.D.; Pinto, Y.; Seeman, N.C.; Musier-Forsyth, K.; Taton, T.A.; Kiehl, R.A. DNA-Templated Self-Assembly of Metallic Nanocomponent Arrays on a Surface, *Nano Lett.* **2004**, *4*, 2343-2347.
12. Zheng, J.; Constantinou, P.E.; Micheel, C.; Alivisatos, A.P.; Kiehl, R.A.; Seeman, N.C. Two-Dimensional Nanoparticle Arrays Show the Organizational Power of Robust DNA Motifs, *Nano Lett.* **2006**, *6*, 1502-1504.
13. Parak, W.J.; Gerion, D.; Zanchet, D.; Woerz, A.S.; Pellegrino, T.; Micheel, C.; Williams, S.C.; Seitz, M.; Bruehl, R.E.; Bryant, Z.; Bustamante, C.; Bertozzi, C.R.; Alivisatos, A.P. Conjugation of DNA to Silanized Colloidal Semiconductor Nanocrystalline Quantum Dots, *Chem. Mater.* **2002**, *14*, 2113-2119.
14. Zanchet, D.; Micheel, C.M.; Parak, W.J.; Gerion, D.; Alivisatos, A.P. Electrophoretic Isolation of Discrete Au Nanocrystal/DNA Conjugates, *Nano Lett.* **2001**, *1*, 32-35.
15. Fu, A.; Micheel, C.M.; Cha, J.; Chang, H.; Yang, H.; Alivisatos, A.P. Discrete Nanostructures of Quantum Dots/Au with DNA, *J. Am. Chem. Soc.* **2004**, *126*, 10832-10833.
16. Alivisatos, A.P.; Johnsson, K.P.; Peng, X.; Wilson, T.E.; Loweth, C.J.; Bruchez, M.P., Jr.; Schultz, P.G. Organization of 'Nanocrystal Molecules' Using DNA, *Nature* **1996**, *382*, 609-611.

17. Claridge, S.A.; Goh, S.L.; Frechet, J.M.J.; Williams, S.C.; Micheel, C.M.; Alivisatos, A.P. Directed Assembly of Discrete Gold Nanoparticle Groupings Using Branched DNA Scaffolds, *Chem. Mater.* **2005**, *17*, 1628-1635.
18. Keren, K.; Berman, R.S.; Buchstab, E.; Sivan, U.; Braun, E. DNA-Templated Carbon Nanotube Field-Effect Transistor, *Science* **2003**, *302*, 1380-1382.
19. Keren, K.; Berman, R.S.; Braun, E. Patterned DNA Metallization by Sequence-Specific Localization of a Reducing Agent, *Nano Lett.* **2004**, *4*, 323-326.
20. Keren, K.; Krueger, M.; Gilad, R.; Ben-Yoseph, G.; Sivan, U.; Braun, E. Sequence-Specific Molecular Lithography on Single DNA Molecules, *Science* **2002**, *297*, 72-75.
21. Puri, N.; Majumdar, A.; Cuenoud, B.; Natt, F.; Martin, P.; Boyd, A.; Milleri, P.S.; Seidman, M.M. Targeted Gene Knockout by 2'-O-Aminoethyl Modified Triplex Forming Oligonucleotides, *J. Biol. Chem.* **2001**, *276*, 28991-28998.
22. Knauert, M.P.; Glazer, P.M. Triplex Forming Oligonucleotides: Sequence-Specific Tools for Gene Targeting, *Hum. Mol. Genet.* **2001**, *10*, 2243-2251.
23. Zhou, D.; Bruckbauer, A.; Ying, L.; Abell, C.; Klenerman, D. Building Three-Dimensional Surface Biological Assemblies on the Nanometer Scale, *Nano Lett.* **2003**, *3*, 1517-1520.